

COSMOLOGICAL SIMULATIONS OF GALACTIC DISC ASSEMBLY

Elisa House

A THESIS SUBMITTED IN PARTIAL FULFILMENT
OF THE REQUIREMENTS FOR THE DEGREE OF
DOCTOR OF PHILOSOPHY

Jeremiah Horrocks Institute for Astrophysics and Supercomputing
University of Central Lancashire

October 2011

Declaration

The work presented in this thesis was carried out in the Jeremiah Horrocks Institute for Astrophysics and Supercomputing, University of Central Lancashire. Unless otherwise stated it is the original work of the author.

While registered for the degree of Doctor of Philosophy, the author has not been a registered candidate for another award of the University. This thesis has not been submitted in whole, or in part, for any other degree.

Chapters 2, 3, and 4 were previously published in E. L. House, C. B. Brook, B. K. Gibson, et al., 2011, “Disc Heating: Comparing the Milky Way with Cosmological Simulations”.

*“Already living her life away from him,
a life he knew very little about,
living with people he had never met
and walking streets he didn’t know,
looking at the far reaches of the sky
and explaining the Universe to someone
whose world finished where hers began.”*

Paul House

I would like to dedicate this thesis to my dear parents. I could not have done it without their unconditional love and endless support.

Abstract

In this thesis, we use cosmological galaxy simulations to model the formation and evolution of disc dominated galaxies, including detailed implementation of chemistry, in order to better understand how disc galaxies can form hierarchically.

We address the issue of kinematic heating in disc galaxies by analysing a suite of cosmological Milky Way-type disc simulations run with different particle-and grid-based hydrodynamical codes and different resolution, and compare them with observations of the Milky Way. By studying the kinematics of disc stars in these simulations, we seek to determine whether or not the existence of a fragile thin disc is possible within a cosmological framework, where multiple mergers and interactions are the essence of galaxy formation.

We study the velocity dispersion-age relation for disc stars at $z = 0$ and find that four of the simulations are more consistent with observations by Holmberg et al. (2008) in which the stellar disc appears to undergo continual/secular heating. Two other simulations are in better agreement with the Quillen & Garnett (2001) observations that suggest a “saturation” in the heating profile for young stars in the disc. None of the simulations have thin discs as old as that of the Milky Way.

We also analyse the kinematics of disc stars at the time of their birth, and find that in some simulations old stars are born cold within the disc and are subsequently heated, while other simulations possess old stellar populations which are born relatively hot. The models which are in better agreement with observations

of the Milky Way’s stellar disc undergo significantly lower minor-merger/assembly activity after the last major merger.

We show that numerical issues are not dominating our results. By running a set of isolated Milky Way-type simulations with different resolution and different density thresholds for star formation we conclude that, on top of the effects of mergers, there exists a “floor” in the dispersion that is related to the underlying treatment of the heating and cooling of the interstellar medium, and the low density threshold which such codes use for star formation.

A persistent issue in simulations of disc galaxies is the formation of large spheroidal components, and disc galaxies with larger bulge to disc ratios than is observed. This problem is alleviated by supernova feedback. We found that by increasing the feedback in the simulations, we decrease the amount of stars that are accreted onto the main galaxy. The star formation is quenched more efficiently in low mass satellites when stronger feedback is implemented as well as in the main halo. These effects result in a disc galaxy which has formed less stars overall, but more importantly, contains less *accreted* stars. As the strong stellar feedback quenches the star formation in the small building blocks, the metallicity of the *accreted* stars is lower than in the case where less feedback was used.

In the context of hierarchical formation, mass assembly is expected to be scale free. Yet the properties of galaxies depend strongly on their mass. We examine how baryonic physics has different effects at different mass scales by analysing three cosmological simulations using the same initial conditions that are scaled to three different masses. Despite their identical dark matter merger history, we show that the simulated galaxies have significantly different stellar accretion histories. As we go down in mass, the lowest mass progenitors are unable to form stars, resulting in a low mass galaxy with less *accreted* stars. The overall chemical properties are also distinct at the different mass scales, as one

might expect from the mass-metallicity relation of observed galaxies. We examine gradients of chemical abundances with radius and with height above the disc, and look for properties that are retained at different mass scales and properties which change, often dramatically.

We analyse the kinematic and chemical properties of their *accreted* and *in-situ* populations. Again, trends can be found that persist at all mass scales, providing signatures of hierarchical structure formation. We find that *accreted* populations in the high mass simulation did not resemble any of the populations in the lower mass galaxies, showing that the chemical properties of proto-galaxies, which merge at high redshift to form massive galaxies, differ from the properties of low mass galaxies that survive at $z=0$.

We probe further the signatures of hierarchical structure formation at smaller scales, in dwarf galaxies. We analysed the morphologies, kinematics and chemical properties of two simulated dwarf galaxies with different merger histories. We again analyse the *accreted* and *in-situ* populations. Observations of dwarf galaxies have found that they are comprised of multiple components. Our simulated dwarfs indicate that such populations may indeed be a manifestation of the hierarchical formation process in action in these lower mass galaxies.

In one simulated dwarf, the *in-situ* stellar component forms a thin disc and a thick disc. We show that the thick disc in this simulation forms from *in-situ* stars that are born kinematically hot in the disc from early gas-rich mergers. The thin disc is formed quiescently from the later infall of gas. The *accreted* stars in the simulation were found to form an extended stellar halo. Chemical signatures of the three populations are also explored.

The second dwarf we analysed has different galactic components, a result found to be due to the different merger history of this galaxy. The last major merger in this simulation occurs early on in the formation process between two

proto-galaxies of similar mass. The result is a dwarf galaxy comprised of a disc formed of *in-situ* stars and a flattened rotating stellar halo formed of *accreted* stars. The angular momentum of the *accreted* and old *in-situ* stars is obtained from the last major merger. We discuss the resemblance of this flattened rotating stellar halo to fast rotating flattened elliptical galaxies, and propose that such structures may explain some of the observed extra-galactic thick discs.

These studies show that galactic properties emerge through the complex inter-play between hierarchical structure formation, star formation, and feedback from supernovae. Different modelling of these processes will alter the simulated galaxy's properties, and detailed comparisons with observations can then be made to determine the dominant processes responsible for different galactic properties. We remain optimistic that further improvement in modelling will allow deeper insights into the processes of galaxy formation and evolution.

Contents

Declaration	2
Abstract	4
Acknowledgements	16
1 Introduction	18
1.1 Galaxies	20
1.2 The Standard Model of Structure Formation and Evolution	21
1.3 Our Milky Way	24
1.3.1 The Thin Disc	25
1.3.2 The Thick Disc	27
1.3.3 The Bulge	31
1.3.4 The Stellar Halo	32
1.3.5 The Dark Matter Halo	33
1.4 Chemical Evolution	34
1.5 Our studies	35
1.5.1 Disc Heating	35
1.5.2 Resolution and Star Formation	35
1.5.3 Feedback Effects	36
1.5.4 Mass-Morphology Relation	36

1.5.5	Hierarchical Formation in Dwarf Galaxies	37
2	Numerical Method	38
2.1	Introduction	38
2.2	Numerical Method	39
2.2.1	SPH	40
2.2.2	AMR	40
2.2.3	Star Formation	41
2.2.4	Feedback	42
2.2.5	Renormalisation Technique	45
2.2.6	Producing Mock Images	47
3	Disc Heating	49
3.1	Introduction	49
3.2	Simulations	51
3.2.1	S09_YCosm_AMR_RAMSES	53
3.2.2	G07_YCosm_SPH_GASOLINE	54
3.2.3	B09_YCosm_SPH_GASOLINE	54
3.2.4	B05_NCosm_SPH_GCD+	55
3.2.5	A03_YCosm_SPH_GRAPESPH	56
3.2.6	H09_YCosm_AMR_RAMSES	56
3.2.7	R08_NCosm_SPH_GASOLINE	56
3.3	Disc Heating	57
3.3.1	Age-Velocity Dispersion Relation	58
3.3.2	Stars Born in the Disc	60
3.3.3	Disc Heating	65
3.3.4	The Effects of Mergers	71
3.3.5	The Central Concentration of the Satellites	74

3.4	Conclusions	76
4	The Effects of Resolution and Star Formation Recipes	79
4.1	Introduction	79
4.2	Isolated Milky Way Models	81
4.3	The Effects of Resolution and Density Threshold	85
4.4	Conclusions	89
5	The Effects of Feedback	91
5.1	Introduction	91
5.2	Simulations	92
5.3	The Effects of Feedback	94
5.4	The Effects of Feedback in <i>Accreted</i> and <i>In-situ</i> Populations . . .	103
5.5	Conclusions	105
6	The Effects of Mass	107
6.1	Introduction	107
6.2	Simulations	108
6.3	The Effects of Mass	112
6.4	The <i>Accreted</i> and <i>In-situ</i> Populations	122
6.4.1	Chemical Gradients	126
6.5	Conclusions	133
7	Hierarchical Formation in Dwarf Galaxies	136
7.1	Introduction	136
7.2	Dwarf Galaxy Simulations	141
7.3	The <i>Accreted</i> and <i>In-situ</i> Populations	143
7.3.1	Morphology and Profiles	143
7.3.2	Kinematics	155

7.3.3	Chemistry	161
7.4	Conclusions	175
8	Conclusions	177

List of Tables

3.1	Properties of the Simulations	52
3.2	Structural Parameters of the Simulations	57
4.1	Primary Galaxy Model Parameters	81
4.2	Properties of the Isolated Simulations	85
5.1	Mass of <i>Accreted</i> and <i>In-situ</i> Populations	104
6.1	Mass of <i>Accreted</i> and <i>In-situ</i> Populations	122
7.1	Profile Fit Results	150

List of Figures

1.1	Hubble Sequence	22
1.2	Milky Way Metallicity Distribution Function	26
2.1	The Schmidt-Kennicutt Law	43
2.2	Renormalisation Technique	46
2.3	Mock Images	48
3.1	Age-Velocity Dispersion of Suite of Simulations	61
3.2	Age-Velocity Dispersion of <i>In-situ</i> stars	63
3.3	Velocity Dispersion at Birthtime	67
3.4	Evolution of Velocity Dispersion	70
3.5	Rotation Curves of Satellites	76
4.1	Isolated Simulations	84
4.2	Velocity Dispersion vs Time of Isolated Simulations	86
4.3	Star Formation Histories	87
5.1	Stellar Merger Histories with Age	95
5.2	Stellar Merger History	96
5.3	Stellar Merger Histories with Fe/H	98
5.4	Fe/H Distribution	99
5.5	Stellar Merger Histories with O/Fe	100
5.6	O/Fe Distribution	101

5.7	<i>Accreted</i> and <i>In-situ</i> Populations	103
5.8	Fe/H Distribution for Populations	105
6.1	Colour Magnitude Diagram	109
6.2	Star Formation Rate	111
6.3	Stellar Merger History	113
6.4	Stellar Merger Histories with Age	114
6.5	Stellar Merger Histories with Fe/H	116
6.6	Fe/H Distribution	117
6.7	Stellar Merger Histories with O/Fe	119
6.8	O/Fe Distribution	120
6.9	Velocity Distribution	123
6.10	Toomre Diagrams	124
6.11	Fe/H Distribution of Populations	127
6.12	Fe/H vs Height of Populations	128
6.13	Fe/H vs Radius of Populations	129
6.14	O/Fe Distribution of Populations	130
6.15	O/Fe vs Height of Populations	132
6.16	O/Fe vs Radius of Populations	133
7.1	Alpha Ratios	137
7.2	Alpha Ratios LMC	139
7.3	Rotation Curve	141
7.4	Stellar Merger Histories	142
7.5	Stellar Merger Histories of <i>Accreted</i> vs <i>In-situ</i>	144
7.6	SBmaps edge-on Dwarf Galaxies	145
7.7	SBmaps face-on Dwarf Galaxies	146
7.8	Dwarf Brightness Profiles	147
7.9	Dwarf Brightness Profiles	148

7.10 Axial Ratios	151
7.11 Rotational Velocity Distribution	155
7.12 Average Rotational Velocity vs Height	156
7.13 Average Rotational Velocity vs Radius	157
7.14 Stellar Merger DG1	158
7.15 DG1 Heating	160
7.16 Fe/H Distribution	162
7.17 Fe/H vs z and R	163
7.18 Stellar Merger Histories with Fe/H	166
7.19 Age-Metallicity Relation	167
7.20 Stellar Merger Histories with O/Fe	169
7.21 O/Fe versus Age	170
7.22 O/Fe vs z and R	171
7.23 O/Fe versus Fe/H	173

Acknowledgements

Since my arrival at the Jeremiah Horrocks Institute (UCLan) in 2007, Brad Gibson has patiently built a strong and exciting extragalactic group, which has resulted in cutting edge and competitive research in the field of galaxy formation. The faith he shows in his students and postdocs is empowering and his enthusiasm for our work is a great stimulus to all. It has been a privilege to be a part of this project and I thank Brad for giving me this opportunity that has enriched my life to such a great extent.

I also owe a great debt to my other supervisors, Chris Brook and Patricia Sánchez-Blázquez. Their knowledge, encouragement and constant support has proved invaluable. Chris Brook's dedication has been inestimable in helping me attain my PhD. He is inspiring, motivating and most of all a patient and knowledgeable mentor. It has been a pleasure to work with such great scientists.

I am extremely grateful to my examiners, Stewart Eyres and Sean Ryan, for accepting to read through this work, which I hope has not been too onerous a task.

I thank the Science and Technology Facilities Council (STFC) for their financial assistance in the form of a PhD grant and additional grants, without which I would never have been able to carry out my studies. I sincerely hope that other students will have the privilege of benefiting from this support in the future.

I would like to thank all those who have made it possible for me to submit

this thesis. Many people have been helpful in providing suggestions and comments on the work presented in this thesis, including Daisuke Kawata, Stephanie Courty, Rok Roškar, Fabio Governato, Greg Stinson, Sarah Buehler, Gareth Few, Francesco Calura, all my co-authors on the paper and the anonymous referees.

I thank everyone at the Jeremiah Horrocks Institute for their friendship, which I am sure will endure, especially my dear flat mate Markus Hartmann whose friendship has got me through the many personal challenges I have faced. He has been my family in Preston.

I would like to offer special thanks to all my loving family, my grandparents Bobby, Mavis and Polly, and my Aunt Lesley. My sister Clea has always been an inspiration and an example to me, and her partner Arturo has always shown great interest in my work. Finally, I thank my parents, Paul and Susan, for their love, encouragement and support.

Chapter 1

Introduction

How galaxies form is an important and interesting topic for astronomers to study, both because the properties of galaxies can provide important insights into cosmological theories, as well as being a fascinating topic in their own right: we do, after-all, live in the disc of a fairly standard large spiral galaxy. There exists a largely accepted theory of galaxy formation, in which structure formation is driven by cold dark matter (CDM) and builds up hierarchically, with small galaxies merging to form progressively larger galaxies. This theory attempts to accommodate galaxy formation within the accepted cold dark matter cosmological paradigm.

However, several problems exist when trying to explain the observed properties of galaxies within this overall cosmological framework. It is hard, for example, to accommodate this scenario, where violent mergers and interactions are a frequent occurrence, with what appear to be fairly fragile, thin galactic discs, which are common in late-type spiral galaxies such as our own Galaxy. The kinematics of galactic populations thus provide constraints on galaxy formation theories.

Further clues to galaxy formation can be gained by examining the evolution of chemical elements in stellar populations, which can provide valuable information regarding the conditions which exist at the time of their birth.

One of the major outstanding “grand challenges” facing astrophysics for the coming decade is the unravelling of the underlying physics governing the formation and evolution of disc galaxies such as our own Milky Way. The vast majority of galaxies in our Universe have disc morphologies (Allen et al., 2006; Cameron et al., 2009). These disc galaxies have long been decomposed into two components, the disc for which they are named which follows an exponential light profile, and a central light concentration, the bulge. However, we have increasingly become aware that disc galaxies are rather more complex systems, made up of multiple components. Apart from the disc and the bulge, all such galaxies which have been looked at deeply enough have found to have a thick disc in addition to their thin disc (Dalcanton & Bernstein, 2002; Yoachim & Dalcanton, 2002) as well as extended stellar halos, for example in MW, M31 (Chapman et al., 2006; Kalirai et al., 2006), LMC (Minniti et al., 2003), and M33 (Mould & Kristian, 1986).

High Performance Computing (HPC) simulations of gravitational N -body and hydrodynamical physics have become a primary tool with which to model galaxy formation in a cosmological context (e.g. Katz et al. 1992; Summers et al. 1993; Navarro & White 1994; Steinmetz & Mueller 1994; Sommer-Larsen et al. 2003; Abadi et al. 2003a; Robertson et al. 2004; Bailin et al. 2005; Okamoto et al. 2005; Governato et al. 2007; Gibson et al. 2009; Sánchez-Blázquez et al. 2009; Agertz et al. 2010). These simulations model the formation and evolution of disc galaxies within a Universe dominated by Cold Dark Matter (CDM) and a cosmological constant (Λ).

In this thesis we make use of these cosmological galaxy simulations to gain insights into the origin of different galactic components. Detailed comparison between observed galaxies and their components will be made throughout. We will in particular focus on the role of hierarchical structure formation in forming

the different components.

1.1 Galaxies

Galaxies in the Universe are well defined astronomical objects that are dynamically bound and contain from a million stars to 10^{12} stars. They are diverse objects spanning a wide range of masses, sizes and morphologies (see Figure 1.1). Despite this they obey certain scaling relations, which makes them intriguing, exciting, and crucial to study, in the sense that, examining their formation and evolution at different epochs sheds light into the structure and formation of the Universe.

One of the most noticeable and obvious properties of galaxies is their morphology. They can be classified into two main groups, ellipticals, which are supported by the random motions of their stars, i.e. by velocity dispersion, and spirals that are rotationally supported and are dominated by a disc component. The earliest classification systems was made by Edwin Hubble in 1927 where he ordered galaxies according to their morphology, from early-type ellipticals that are pure ellipsoids, to late-type spirals that are pure discs (Cameron et al., 2009; Cheng et al., 2011). Figure 1.1 shows images of galaxies showing the Hubble sequence. However, not all galaxies observed in the Universe fall on the Hubble sequence. Dwarf galaxies, the faintest galaxies in the sky, do not fall on the sequence and they can be subdivided into two groups. There are dwarf galaxies with ongoing star formation and where most of their baryonic component is gas. These are called dwarf irregulars (dIrr). Dwarf galaxies that have no gas or young stars are referred to as dwarf spheroidals (dSph). In addition to dwarf galaxies, there are also a group of bright galaxies that are neither spirals nor ellipticals and we often classify these as peculiar or irregular galaxies.

We can directly relate the Hubble sequence to the formation history of galaxies. For example, it is believed that ellipticals and spirals have different formation pathways and therefore lie separately on the sequence. The sequence also contains important information on galaxy evolution. Figure 1.1 shows the Hubble sequence at two different epochs of formation, now and 6 billion years ago. These two times show very different sequences where the number of peculiar galaxies increases as you go back in time. This provides important information regarding the evolutionary path of galaxies. How galaxies have evolved through these phases, and whether this is related to the hierarchical structure formation inherent in cold dark matter cosmologies, is a very active area of scientific research.

1.2 The Standard Model of Structure Formation and Evolution

Today, the favoured model for the formation and evolution of structure in the Universe is the current concordance cosmological model (White & Rees 1978; Blumenthal et al. 1984; Spergel et al. 2003), in which the energy budget is dominated by a term which causes the Universe to accelerate its expansion, the cosmological constant Λ , and the mass budget is dominated by a component which is non-relativistic (cold) and interacts with the baryonic matter via gravity alone (dark matter). The concept of dark matter goes back to the 1930s when Fritz Zwicky was studying galaxy clusters, and found that about 10 times more mass was needed than was observed to keep the galaxies gravitationally bound within the clusters. During the 1970s observers started to measure the rotation curves of external galaxies (Rubin & Ford, 1970) and found remarkably that they remained constant with radius, evidence once again of a significant component in galaxies that remains invisible to the eye, i.e undetectable electromagnetically.

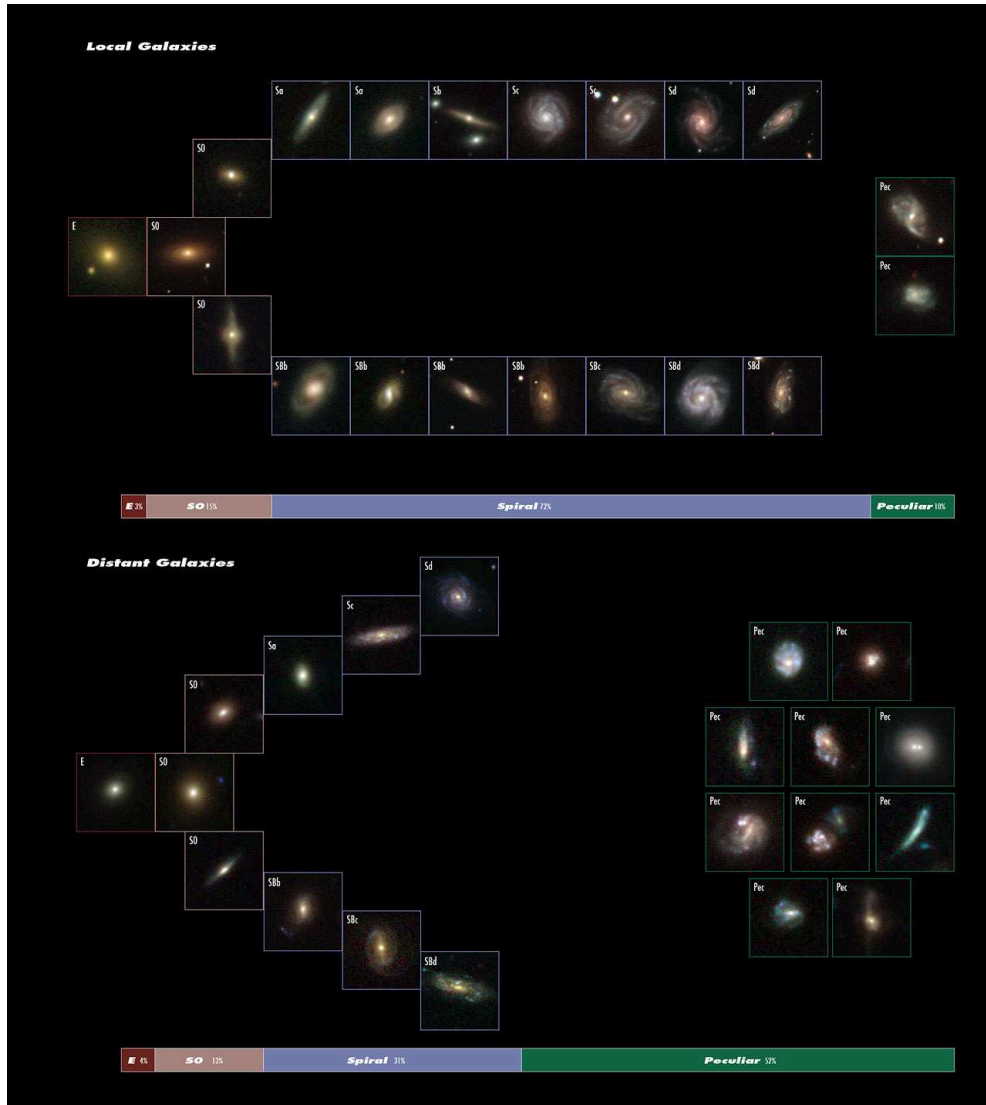


Figure 1.1: This image created with data from NASA/ESA Hubble Space Telescope and Sloan Digital Sky Survey shows the Hubble Sequence at two different epochs, today (top panel) and 6 billion years ago (bottom panel). The two images are very different from one another, which offers clues to their evolution. The top image represents the local Universe with most of the galaxies being late-type spirals. The bottom image shows the distant Universe, where there is a much larger fraction of peculiar galaxies than today. This could be a manifestation of hierarchical formation in which peculiar galaxies are the basic building blocks. Credit: NASA, ESA, Sloan Digital Sky Survey (SDSS), R. Delgado-Serrano and F. Hammer (Observatoire de Paris).

At the same time that dark matter was being discovered, the cosmological model was born as a result of the so-called Big Bang theory. Around 1929 Edwin Hubble discovered that the galaxies were receding from one another, which meant that the space between galaxies was expanding. If this were true then if you go back in time instead of forward, it is evident that the galaxies would get closer and closer together until they reached an incredible dense and hot state resulting in a catastrophic event, The Big Bang, approximately 13.7 Gyr ago. The Big Bang was later proven by the detection of the cosmic microwave background (CMB) radiation (Penzias et al., 1969), lingering from the explosion.

Accurate measurements of the temperature fluctuations of the CMB by The Wilkinson Microwave Anisotropy Probe (WMAP) (Spergel et al. 2003) satellite has helped build the concordance cosmological model. It consists of a flat Universe with total energy density close to the critical density, $\Omega = \rho/\rho_c = 1$. Approximately 1/3 of the density is matter, $\Omega_M = 0.29 \pm 0.07$, with dark matter dominating, $\Omega_{DM} = 0.243 \pm 0.06$ and only 5% is baryonic matter, $\Omega_B = 0.047 \pm 0.006$ (Spergel et al. 2003). The rest of the density is attributed to the vacuum energy, $\Omega_\Lambda = 0.73 \pm 0.04$, often referred to as dark energy and is responsible for the expansion of the Universe. The expansion rate of the Universe, known as the Hubble constant H_0 , has a value of $H_0 = 72 \text{ km/s/Mpc}$.

The Λ CDM model provides a framework for the formation and evolution of structure within the Universe, such as galaxies, galaxy clusters and filaments. The Universe initially was an extremely hot, dense homogenous plasma of elementary particles. After $\approx 10^{-30}$ sec since The Big Bang the Universe started expanding very rapidly and exponentially, a period known as inflation. During this inflation period initial quantum fluctuations were converted into macroscopic cosmological perturbations seeding the primordial density or temperature perturbations in the CMB, which in turn became the seeds for the collapse of matter into over

dense regions and eventually the formation of structure. The amplitude of the density perturbations increases with decreasing scale. This means that small-scale perturbations collapse first and then merge to form larger structures in a hierarchical or “bottom-up” fashion.

In classic theory of the formation of disc galaxies, tidal torques from surrounding large scale structures provides angular momentum for gas, which cools into a central galaxy, retaining its angular momentum to form a disc (Fall & Efstathiou, 1980). As will be discussed later in the thesis, there are outstanding issues with this theory particularly when placed within the context of the hierarchical structure formation that is implicit in cold dark matter cosmologies. We will attempt to gain insights into how disc galaxies can form within the current cosmological paradigm.

1.3 Our Milky Way

Our home galaxy, the Milky Way, is a typical large spiral galaxy, classified as an SBc (see Figure 1.1) as it contains a central bar. The Milky Way is the only galaxy for which very detailed abundances and kinematical data are available to us. This makes the Milky Way a unique testbed for models of galaxy formation.

It has been well established for some time now that the Milky Way has several distinct structural components, which are also thought to have formed at different times in the Galaxy’s evolution as they are dynamically and chemically distinct (see Figure 1.2 that shows the metallicity distribution function of the different Galactic components). It has a central bulge, an extended flattened disc, an extended spherical stellar halo, and all are encompassed by a large non-baryonic component, the dark matter halo. The Sun lies 8 kpc from the centre (Eisenhauer et al., 2003) close to the mid-plane embedded in the stellar disc, which is the most prominent feature of the Milky Way and extends out to at least 15 kpc in radius.

The disc is further separated into a thin disc, which contains most of the total disc stars, and all the massive young stars, and a thick disc, which contains old stars and extends further than the thin disc above the plane, hence the name.

1.3.1 The Thin Disc

The thin disc contains 90% of the total baryonic component of the Milky Way, with a mass of $\sim 5 \times 10^{10} M_{\odot}$ (Mo et al., 2010). Its scaleheight, defined as the distance one must move in the direction perpendicular to the plane to see the density fall by a factor e , is between ~ 200 to 400 pc (Jurić et al. 2008; Carollo et al. 2010). The thin disc is approximated by an exponential density profile with a scalelength of ~ 3.8 kpc (Bensby et al., 2011). As mentioned above, thin disc stars are mostly young massive stars with an average age of ~ 6 Gyr, with the oldest stars having ages up to ~ 10 Gyr (Edvardsson et al., 1993), although determining the ages of stars has proven to be observationally very challenging. Thin disc stars are metal rich with a metallicity distribution function (MDF) spanning a range of $-1 \leq [\text{Fe}/\text{H}] \leq 0.4$ dex, and peaking at around solar metallicity (Nordström et al. 2004; Ivezić et al. 2008; Lee et al. 2011). The stars in the thin disc orbit the Galactic centre at $\sim 200 \text{ km s}^{-1}$ and they follow nearly circular orbits. All of the dust in the Galaxy lies in the plane of the thin disc and it also contains about $5 \times 10^9 M_{\odot}$ of cold gas (Mo et al., 2010), moving on circular orbits close to the mid-plane of the disc. The majority, 80% of this gas is neutral (Mo et al., 2010), i.e. atomic hydrogen HI, which is observed in 21cm radio line emission. The rest of the cold gas, 20% (Mo et al., 2010), is in the form of molecular gas and is best observed in millimetre-wave line emission from carbon monoxide (CO). It is more centrally concentrated than the atomic gas, mostly found as a ring at 4.5 kpc from the centre of the Galaxy (Mo et al., 2010). The molecular gas is found in molecular clouds with masses around 10^5 - $10^7 M_{\odot}$ and

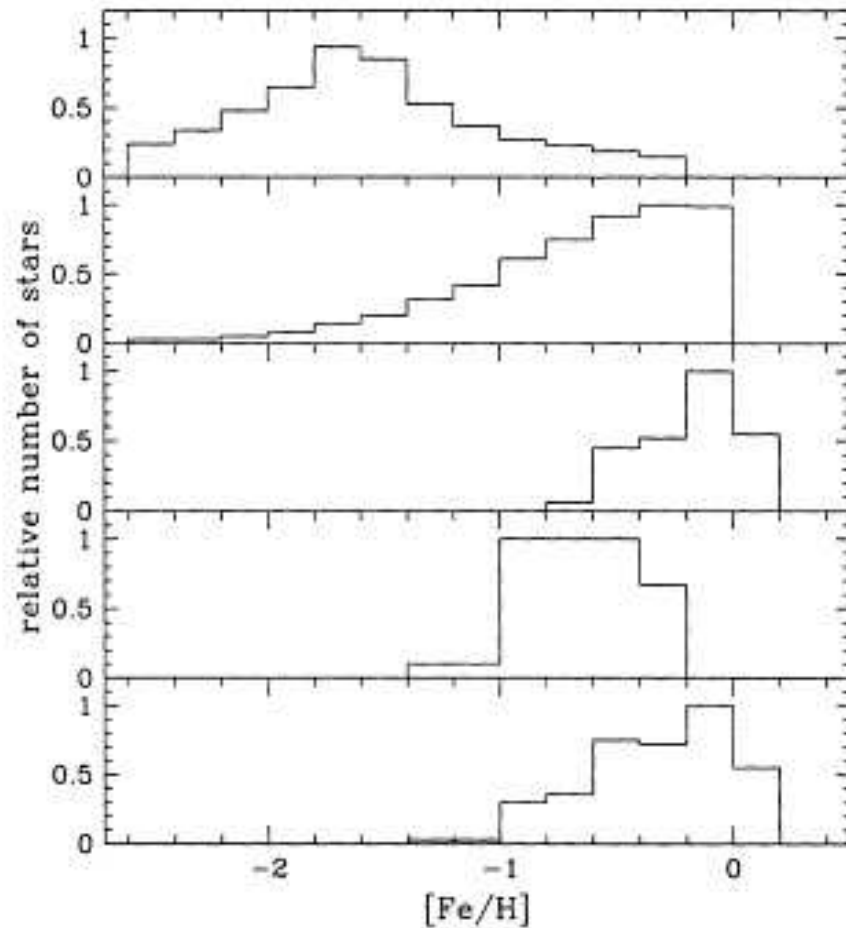


Figure 1.2: This figure was taken from Wyse (1999), and shows the metallicity distribution function (MDF) of the different components of the Milky Way, normalised to unity. From top to bottom; the Solar neighbourhood halo (Carney et al., 1994); the outer Galactic bulge (Ibata & Gilmore, 1995), truncated at solar metallicity due to calibration limitations; the volume complete local thin disc F/G stars (from the Gliese catalogue); the volume complete local thick disc stars; and the “solar cylinder”, i.e. F/G stars integrated vertically from the disc plane to infinity.

with high densities of around $100 \text{ atoms cm}^{-3}$. Star formation occurs in these molecular clouds. Therefore, most of the star formation in the Galaxy occurs in the disc due to the gas embedded in it as well as its spiral structure, which triggers star formation.

1.3.2 The Thick Disc

Thick discs were first discovered as faint features described as envelopes surrounding external S0 galaxies (Burstein (1979); Tsikoudi (1979)). The existence of a second thicker disc component in the Milky Way was discovered later by Gilmore & Reid (1983) and this along with subsequent studies of the ages, abundances, and kinematics showed that the thin and thick disc are indeed distinct components and that the thick disc presented a unique episode in the Galaxy's formation (e.g Reid & Majewski 1993; Nissen 1995; Chiba & Beers 2000; Bensby et al. 2007), where a thin disc whose stars have formed continuously over $\sim 9 \text{ Gyr}$, is superimposed on an old thick disc. The thick disc has also been shown to be a common component in most, and possibly all, observed spiral galaxies (Yoachim & Dalcanton 2008), at least in the sense that the light distributions are better fit by two functions rather than one. Recent observations carried out measuring the stellar population of the Milky Way's thick disc give scaleheights that range between $500 - 1100 \text{ pc}$ (Jurić et al. 2008; Carollo et al. 2010) and a scalelength very similar to the thin disc, though recent studies suggest that it is smaller than the thin disc, with a scalelength of $\sim 2 \text{ kpc}$ (Bensby et al., 2011). The rotational lag of the thick disc of the Milky Way ranges from 20 kms^{-1} (Chiba & Beers 2000) to 50 kms^{-1} (Soubiran et al. 2008). It is also kinematically hotter, with a velocity dispersion perpendicular to the plane, i.e. σ_w , measured to be $46 \pm 3 \text{ kms}^{-1}$ in Chiba & Beers (2000) and $63 \pm 4 \text{ kms}^{-1}$ in Soubiran et al. (2008). The thick disc mass is about 6 - 13% that of the thin disc (Chen et al., 2001). The stars are

old (> 5 Gyr) and are alpha enhanced (Bensby et al. 2003; Feltzing et al. 2003; Mishenina et al. 2004; Bensby et al. 2005; Ramírez et al. 2007), as well as more metal poor with a metallicity distribution function (MDF) ranging between $-2.2 \leq [\text{Fe}/\text{H}] \leq 0.0$ dex (Bensby et al. 2007). Analysis of surface brightness profiles of edge-on spiral galaxies from deep broadband imaging have shown breaks in the profiles at large scaleheights and low surface brightnesses also indicative of a second thicker component (Yoachim & Dalcanton (2005); Pohlen et al. (2004)).

The formation of the thin disc is well explained by the dissipational collapse of a gas cloud. However, the formation of the thick disc is still to date poorly understood and therefore a number of different formation scenarios for the thick disc exists in the literature. We provide a brief summary of the most common of these formation theories.

The Thick Disc: Formation Scenarios

- **Disc Heating Through Internal/Secular Processes:** The steady kinematical heating of a thin galactic disc via internal mechanisms is described in Haywood (2008) and Schönrich & Binney (2009). In this scenario the thick disc is created without accretion from outside the galaxy, i.e. the thick disc forms *in-situ*. Recently, models of discs which are entirely isolated from the satellite bombardment that is predicted in Λ CDM, have shown that radial migration of stars from inner to outer radii as well as the gravitational interactions with spiral structure and giant molecular clouds, that scatter the stars to large scaleheights, can explain the observed kinematics, structure and chemical properties of the thin and thick disc (Loebman et al., 2010) In this context, stars with different ages will have different velocity dispersions, which gives rise to a vertical age gradient that has been observed both in the Milky Way as well as other external edge-on spiral

galaxies and low-mass galaxies (Seth et al. 2005). If a pre-existing thin disc was kinematically heated gradually and continuously via internal processes, it would produce a continuation of the thin disc above the plane, often referred to as the old thin disc. Observations of the Milky Way's thick disc by Quillen & Garnett (2001) show an abrupt increase in the vertical velocity dispersion at older ages. This cannot be explained through gradual internal heating. On the other hand, observational results from Holmberg et al. (2008) show conflicting results, where the vertical heating in the Milky Way's disc seems to be increasing gradually with age, agreeing with theories that internal heating forms the thick disc. However, models based on radial migration have difficulties in explaining counter-rotating discs observed in external spiral galaxies (Yoachim & Dalcanton 2005).

Recent models by Schönrich & Binney (2009) show that transient spiral arms in the galactic thin disc can in fact lead to the formation of a thick disc. These models have successfully reproduced thick disc dynamical and chemical properties. If heating is the cause of the thick disc then one would expect radial and vertical metallicity gradients. The old metal poor stars in this context are the ones being pushed out to larger distances from the plane and therefore we would observe metallicity gradients going from high metallicities in the inner regions formed by young stars, that have not yet migrated, to lower and lower metallicities for older stars as we go further out in the galaxy. Observations of external edge-on spiral galaxies in the literature however, have not found gradients in metallicity for thick discs.

- **Disc Heating Through A Merger/Accretion Event:** In this scenario a previously existing thin disc is heated kinematically, like above, only this time the heating is induced by external sources such as merger/accretion events during the hierarchical process. Described in Quinn et al. (1993);

Velazquez & White (1999); Villalobos & Helmi (2008); and Kazantzidis et al. (2008), they show how accretion events can puff up or even destroy the disc of galaxies early on in their formation. These models predict some of the distinct global properties, such as the the scaleheight and kinematics of the thick disc stars. Simulations in this context of thick disc formation, e.g Quinn et al. (1993), predict that infalling satellites increase the velocity dispersion of thick disc stars but they do not substantially change their initial angular momentum. Now, because these thick discs form from heated thin disc stars then their net rotation should be similar. Observations by Yoachim & Dalcanton (2005) that show external galaxies with counterrotating disc cannot be explained through this scenario.

Disc heating via a merger or accretion event takes place over a relatively short timescale compared to say disc heating through internal processes, which heat the disc gradually over time. Because of this, in the merging scenario no vertical metallicity or age gradients are expected, comparable to the gradual secular heating model.

- **Thick Disc Formation Through Gas Rich Mergers:** This formation scenario was first proposed by Brook et al. (2004). In this model the thick disc forms *in-situ* after a series of gas-rich mergers that trigger star formation at large scaleheights forming the thick disc. This raises the question of whether the age-dispersion relation as measured by Quillen & Garnett (2001) is at least in part due to the earlier discs being, in general, hotter than the later discs – i.e. the old stars were born hotter than the younger stars, possibly related to earlier mergers in Λ CDM having higher mass ratios between the mass of the central galaxy to the accreted satellite in general than later mergers (Brook et al. (2005)). Recent observations showing that high redshift discs are quite thick (Dalcanton & Bernstein (2002); van

Starkenburger et al. (2008); Lemoine-Busserolle & Lamareille (2010)) possibly show evidence for this formation scenario. Because the thick disc stars form *in-situ* from well mixed enriched material, no gradients in metallicity are expected to be present in this scenario.

- **Thick Disc Formation Through Direct Accretion From Satellites:** Abadi et al. (2003a) proposed that a satellite that was accreted by a disc galaxy may be dragged into the plane of the disc via dynamical friction, hence forming the thick disc. This scenario differs from all the above such that the thick disc in this case is formed out of *accreted* stars and not stars born in the main halo. However, studies which compare the abundances of dwarf spheroidal and irregulars with the different components of the Milky Way have shown that they are chemically distinct, ruling out that at least the Milky Way's thick disc could have formed by the accretion of satellites which resemble local dwarfs (Venn et al., 2004).

In Chapter 7 we will see that one of our simulated dwarf galaxies has a component which resembles a thick disk, and is composed of *accreted* stars from the last major merger (LMM) at a high redshift, $z = 2$, with a mass ratio of $\sim 1:1$. The angular momentum of the system today stems from this last major interaction of these two proto-galaxies of similar mass. We will propose that some observed thick discs may form via this manner. We also show in a second simulated dwarf a thick disc that forms from a combination of gas rich mergers and is also heated from the mergers during its epoch of formation.

1.3.3 The Bulge

The centre of the Milky Way is characterised by its bulge, a slightly flattened spherical distribution of stars. Observations (Williams et al., 2011) showed that these boxy bulges are actually an elongated component identified as their bar.

Its metallicity distribution shows a significant spread, $-1.5 \leq [\text{Fe}/\text{H}] \leq 0.5$ dex, with a peak at ≈ 0.25 dex (Zoccali et al. 2008). The bulge of the Milky Way is rotating, peaking at $\sim 75 \text{ km s}^{-1}$ and has a large velocity dispersion of 120 km s^{-1} . The stellar population of the bulge tends to be fairly old, typically older than ~ 10 Gyr. However, recent observations have revealed the presence of young massive stars in the bulge indicating recent star formation in this region. It is therefore now believed that the bulge is comprised of two populations, an old spheroidal population that formed rapidly early on and a newer younger population that forms over a longer period through secular evolution in the disc (Minniti & Zoccali 2008).

1.3.4 The Stellar Halo

The stellar halo is a spherical component of approximately $10^9 M_{\odot}$ (Morrison, 1993) of old stars and globular clusters, with ages of $10\sim 14$ Gyr. Only 1% of the total Milky Way's stellar content is found in the stellar halo. The stars in the stellar halo have large random motions and it is therefore largely supported by velocity dispersion.

Although the stellar halo was once considered a single component, it is now well established that it can also be separated into two overlapping components, the inner and outer stellar halo (Carollo et al. 2007). The inner stellar halo dominates the population of halo stars up to 10 - 15 kpc. It has stars that present a flattened spatial density distribution and exhibit a small prograde rotation of around 7 km s^{-1} (Carollo et al. 2010). The inner halo stars have large random motions with velocity dispersions up to 150 km s^{-1} (Carollo et al. 2010), meaning that this component is largely supported by velocity dispersion. The stellar population of the inner halo has higher metallicities than the outer halo stars, with its metallicity distribution function (MDF) peaking at $[\text{Fe}/\text{H}] = -1.6$. The

density profile of the inner halo is best described by a power law of the form $\rho_{in} \sim r^{-\alpha}$ with $2 \leq \alpha \leq 3$ according to Bell et al. (2008). The outer halo, on the other hand, has a much more spherical distribution and a stellar population with net retrograde rotation, between -40 and -70 kms^{-1} . Its stars also have lower metallicity, peaking at $[\text{Fe}/\text{H}] = -2.2$. It exhibits a different and steeper density profile, $\rho_{out} \sim r^{-\alpha}$ with $3 \leq \alpha \leq 4$ (Bell et al. 2008).

It is believed that some fraction of the halo stars comes from the debris of accreted and disrupted satellite galaxies during the formation process of the Milky Way. However, there is also strong evidence of *in-situ* stars in the stellar halo, which are a result of stars born in the centre of the Galaxy and are heated and expelled, due to mergers, to the inner halo (Zolotov & Friends 2009; Zolotov et al. 2010).

1.3.5 The Dark Matter Halo

Last but by far not least is the most dominant component of the Milky Way, the dark matter halo. One of the most challenging tasks for modern cosmology is to determine the nature and origin of this dark component. Its presence rather than observed is inferred from the outer rotation curve of the Galaxy. One thing that is evident from observations is that its distribution is far more extended than the luminous component of the Milky Way, extending well beyond 100 kpc from the Galactic centre. The estimated total mass of this unseen distribution of dark matter is about $10^{12} M_{\odot}$ (Zaritsky et al. 1989; Wilkinson & Evans 1999; Battaglia et al. 2005). These observations support the idea that galaxies in the Universe reside in extended dark matter halos, as suggested by cosmological models.

1.4 Chemical Evolution

Studying the changes in the abundances of chemical elements in the Universe is an important study for galaxy formation and evolution. Current cosmological models show that the Big Bang produced primordial gas composed of mostly hydrogen, 91%, and helium, 9%, with small traces of Lithium (Mo et al., 2010). This is known as *primordial nucleosynthesis*. The baryonic material in the Universe today, however, contains other elements. Astronomers refer to these elements heavier than helium as *heavy elements* or *metals*. The term *metallicity* is used for the fraction of heavy elements, expressed as a fraction by mass.

The heavy elements have been synthesised in nuclear reactions in the cores of stars. This process is known as *nucleosynthesis* (Matteucci, 2007). In the later stages of stellar evolution, the metal enriched material in the stars can be expelled to the interstellar gas through mass loss and supernova explosions. Subsequent star formation from this pre-enriched gas in turn results in newly formed stars with enhanced abundances of heavy elements. This cycle of star formation and expulsion of metal rich material repeats over time gradually increasing the metallicity of the interstellar medium.

As heavy elements are ejected into the interstellar medium through supernovae, they are important in the context of chemical enrichment. Massive stars ($M \geq 8 M_{\odot}$) end their lives as supernovae type II, SNeII, which are short-lived explosions (Matteucci, 2007). The material they eject is enriched in α -elements, such as O, Ne, Mg, Si, S (Nomoto et al., 2002). In contrast, supernova type Ia, SNeIa, are probably caused by explosive fusion reactions in low mass stellar binary systems ($1-8 M_{\odot}$) (Matteucci, 2007). They mainly eject Fe-peak elements into the surrounding gas (Nomoto et al., 2002). They have longer lived progenitors than SNeII and therefore one sees a delay in the production of Fe compared to the α -elements. Due to the different timescales at which these two types of

supernovae occur and the fact that they enrich the surrounding material with different heavy elements, it is common to analyse the $[\alpha/Fe]$ ratio as it contains information about the timescales of formation in galaxies. The chemical signatures of stars and galaxy, therefore act like fingerprints, where they hold clues as to the formation process at early times as well as their evolution.

1.5 Our studies

In this thesis we explore aspects of galaxy formation, which all relate to the origin of galactic components in Λ CDM. We look specifically at:

1.5.1 Disc Heating

A principal difficulty resides in trying to accommodate the early collapse and violent merging history intrinsic to the canonical framework of “hierarchical assembly” of galactic structure with the apparent stability of what should be fairly fragile thin galactic discs. Observations show that there is a relation between age and velocity dispersion for disc stars. The oldest and kinematically hottest stars comprise a separate thick disc component.

We study the causes of the age-velocity dispersion relation of disc stars using a suite of cosmological simulations of disc galaxies. We sample a wide range of disc galaxy formation pathways. In particular, we determine whether disc stars are born hot or cold at early times, and the degree to which they subsequently heat vertically.

1.5.2 Resolution and Star Formation

The issue of the effects of numerical heating is important in all studies of disc heating. We show that numerical heating is not causing the measured disc heating

in the simulations. We highlight the role of the implementation of star formation recipes, and the modelling of the interstellar medium in which stars are formed, as determinants of a dispersion “floor” for the simulations.

1.5.3 Feedback Effects

The loss of angular momentum in the luminous component of disc galaxies has been a major problem in cosmological simulations. In these simulations, gas cools efficiently via radiative processes, causing baryons to collapse rapidly during the earliest phases of the hierarchical clustering process. The luminous component ends up transferring angular momentum to the dark matter halo making the luminous component deficient in angular momentum. This is often referred to as the “angular momentum problem” (Navarro & Benz 1991; Steinmetz & Navarro 2002). As a result, these simulations typically produce galaxies with an overly-dominant spheroid component and an overly small disc (Abadi et al. 2003a; Scannapieco et al. 2009), in disagreement with observations of disc galaxies (Brook et al. 2004). This problem has largely been alleviated by the introduction of greater feedback (Thacker & Couchman, 2000; Brook et al., 2004; Governato et al., 2007). We examine the effects of different supernova feedback recipes on the accretion history of our simulated galaxy. We look at the decrease in the amount of accreted stars when increased feedback is included, and examine the effects on the chemical abundances of the resultant galaxies.

1.5.4 Mass-Morphology Relation

Structure formation which occurs in cold dark matter cosmologies is scale free. That is, the hierarchical build up of low mass dark matter halos is essentially self similar to more massive halos. Small differences in the power spectrum do exist, and will effect statistical studies of galaxy formation. However, the similarities

between the mass ranges is close enough that it is evident that astrophysical rather than cosmological factors are driving the differences between low and high-mass galaxies. That is to say, the physics involved in modelling the gas, star formation, and feedback account for the differences in low and high-mass galaxies. We do an experiment which assumes exact self similarity of structure formation of a dark matter halo at different masses, in order to isolate the effects of our model's input physics from the differences in merger histories, and to examine how the physics has different effects at different mass scales.

1.5.5 Hierarchical Formation in Dwarf Galaxies

Dwarf galaxies have been observed to have different stellar populations, which have been related to different components (Smecker-Hane et al. 2002; Pompéia et al. 2008; Yoachim & Dalcanton 2006). In the context of hierarchical formation, mass assembly is expected to be scale free. Yet as mentioned above, baryonic physics has different effects at different mass scales. Therefore, we will test whether hierarchical structure formation plays a role in forming these different stellar populations. The relation between these populations and galactic components will also be examined.

Chapter 2

Numerical Method

2.1 Introduction

Cosmological simulations have become the primary tool with which we model the growth of structure in the Universe. In our current understanding of the formation and evolution of the Universe, after the Big Bang, space is homogeneous and isotropic. Shortly after small scale fluctuations evolve in the radiation matter and density fields to form large scale structures, like galaxies and galaxy clusters, as we see them at the present time. All cosmological simulations assume that the Universe is dominated by dark matter interacting merely gravitationally. The preferred, most widely accepted model is the so-called Cold (non-relativistic) Dark Matter (CDM) theory. In this framework, the energy density is dominated by CDM and a cosmological constant (Λ) and where baryons only contribute a small fraction ($\sim 5\%$) of the total matter in the Universe. In this cosmological context matter forms hierarchically where small objects collapse and continuously merge to form the larger structures, such as galaxies, galaxy clusters and galaxy groups. Because dark matter dominates in mass over baryonic matter, the gas collapses within dark matter halos eventually forming a galaxy where structure, both dark and baryonic, build up via continuous accretion.

In order to study the past, present and future of our Universe, observations alone are insufficient. We therefore use cosmological simulations that capture important processes and use them to bridge the gap between observations of the early Universe and how we see it today. In a way, simulations are “experiments” that are used to verify theories of formation and evolution of the Universe.

2.2 Numerical Method

In this study we use N-body hydrodynamical simulations to model the formation and evolution of galaxies in the Universe. In cosmological simulations one needs to firstly generate the initial conditions according to the cosmological structure formation model as a result of tiny quantum fluctuations in an initially homogeneous Universe (as seen by the cosmic background radiation) and secondly the density field which is evolved forward in time. Simulations take advantage of large parallel supercomputers in which hundreds of processors are used simultaneously to compute these forces and advance the system to the next timestep.

N-body simulations are used in cosmology to determine the evolution of a large number of masses under the influence of their own gravitational attraction. They use a very simple principle and that is, from the particle’s position, it derives the gravitational force on each particle. This calculated force is then used to advance the position and momentum of each particle in order to create new forces. This is repeated so that we get information about the time evolution of the system in question. Computationally this is done with an N-body algorithm

Hydrodynamics is the physics of fluids in motion. It is based on the conservation laws of mass, momentum, and energy and is used to calculate physical properties of the fluid such as its velocity, pressure, density and temperature as a function of space and time. This part of the code deals with the gas physics in the simulations such as the processes of radiative cooling, star formation, and

feedback from supernovae. The hydrodynamic part of the code, i.e. the gas, can be modelled with two different techniques, either using a Lagrangian particle code (SPH) or a Eulerian grid code (AMR). Despite the use of very different numerical schemes, both yield similar results. I will discuss the differences each technique uses in this next section.

2.2.1 SPH

The smoothed particle hydrodynamics technique uses a set of discrete elements referred to as particles. These discrete particles have a spatial distance that separate them, which is known as the smoothing length, normally represented by h . This smoothing length determines at what distance the physical properties of such particles are “smoothed”, hence the name. The function that is usually used is the kernel function.

The basis of any SPH formalism can be described with the equation:

$$f(\mathbf{r}) = \sum_i \frac{m_i}{\rho_i} f(\mathbf{r}_i) W(|\mathbf{r} - \mathbf{r}_i|, h), \quad (2.1)$$

where $f(\mathbf{r}_i)$, W , m_i , and ρ_i are the scalar value, smoothing function, mass and density of particle i , and i ranges through all particles in the smoothing kernel, W .

The smoothing length of the particles in an SPH simulation can be fixed. However, to achieve greater resolution and to make better use of the computing power it is wiser to assign each particle its own smoothing length and allowing it to vary with time and also to adapt depending on local conditions.

2.2.2 AMR

The mesh codes combine an N-body solver used to follow the evolution of collisionless dark matter with a Eulerian method that uses geometric grids to track

the movement of the gas in the simulation. These grids can be fixed or adaptive (adaptive mesh refinement (AMR)). In the AMR codes there is an adaptive hierarchy of grid patches varying the level of resolution. Each rectangular grid patch, which is referred to as a “grid”, covers some region of space in its parent grid which requires higher resolution, and can itself also become a parent grid to an even more highly resolved child grid. In this way you have higher levels of refinement chosen at the densest regions which will have higher resolution. The grid is continuously refined or de-refined throughout the length of the simulation to ensure that the mean number of particles remains constant to keep two-body heating to a minimum.

2.2.3 Star Formation

An important aspect in galaxy formation codes is the manner in which star formation recipes are modelled and different star formation models used by different groups are very similar. Essentially, they describe the conversion of gas into stars, as stars form from the gravitational collapse of dense gas clouds. These models are based on the idea that stars can only form when the gas reaches a certain density threshold, generally being 0.1 atoms/cm^3 . We will discuss the effects that implementing more realistic density thresholds has on galaxy simulations in Chapter 4. Once a region of gas in the simulation is above this density, stars are allowed to form over a timescale proportional to the dynamical time. One regulates the amount of stars formed during this period with an efficiency parameter, the star formation efficiency (c_*), which is tuned to observed star formation rates of real galaxies. Eligible gas particles are converted into stars according to the equation:

$$\frac{\Delta M_\star}{\Delta t} = c_\star \frac{M_{gas}}{t_{dyn}} \quad (2.2)$$

Here, ΔM_* is the mass of star particles formed, Δt is the timestep between star formation events, M_{gas} is the mass of the gas particle, t_{dyn} is the dynamical time of the gas particle, and c_* is the efficiency parameter.

There is a well known observed correlation between the average star formation rate and gas density, known more commonly as the Schmidt-Kennicutt law (Kennicutt 1998). Specifically, it states that the density of cold neutral gas, mostly atomic hydrogen, correlated with global star formation. All galaxy formation models, independent of their different star formation recipes, reproduce this fundamental relation, shown in Figure 2.1.

2.2.4 Feedback

As we shall see in chapter 5, the correct modelling of supernovae feedback is fundamental for simulating disc galaxies in a cosmological context. Structure formation in cosmological simulations is driven by dark matter that eventually collapses due to local overdensities. The gas initially traces the dark matter and star formation is triggered in the most dense regions as we discussed above. When the most massive stars end their lives they “feedback” energy from their supernova explosion into the surrounding interstellar medium. Without the effects of feedback, gas cools to the central regions of proto-galaxies, and rapidly forms stars prior to their merging/accretion, with angular momentum lost to dynamical friction as the central galaxy is assembled. This is best known as the “angular momentum problem” (White & Frenk, 1991). Early simulations of disc galaxies suffered from the loss of angular momentum, forming overly-dominant spheroids. The angular momentum problem has been shown to be at least alleviated, and perhaps solved, by improved modelling of energetic feedback from supernovae, coupled with increased resolution (Thacker & Couchman, 2000; Governato et al., 2007).

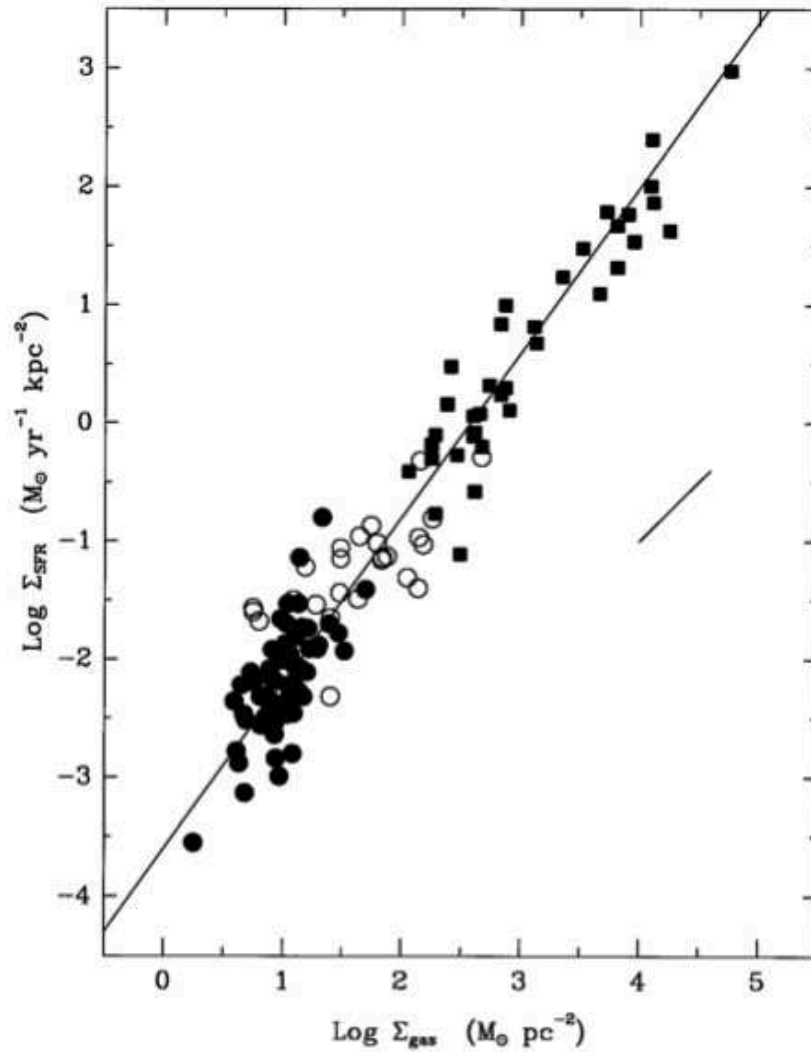


Figure 2.1: The Schmidt-Kennicutt Law, with normal spiral galaxies shown as filled circles and the starburst galaxies as squares. The open circles show the star formation rates and gas densities for the centres of the normal disc galaxies. The line is a least-squares fit with index $N=0.4$ and is the famous Schmidt-Kennicutt slope for disc galaxies (Kennicutt 1998).

Various methods have been suggested to incorporate the supernovae feedback into numerical simulations. Three common models are “thermal feedback”, “kinetic feedback” and “adiabatic feedback”.

Thermal Feedback

Early models simply inject thermal energy to the surrounding gas particles. This type of feedback was found to be highly inefficient (Katz et al., 1992), because in the dense regions where star formation occurs and hence where gas is heated by supernovae, the cooling times are shorter than the simulation timesteps. The thermal energy was therefore lost before it had an effect on the surrounding particles. This problem of resolution has led researchers to implement feedback in different ways, which are included in a manner that try to capture the effects which are occurring on “sub-grid” scales.

Kinetic Feedback

In this model a fraction of the energy ejected by a supernova explosion is converted into kinetic energy, i.e. the kinetic energy is directly injected into the surrounding gas. It is motivated by the fact that the gas will not thermalise immediately due to its bulk motion. If kinetic energy is not injected, then the gas will lose very quickly the added energy from the explosion due to radiative cooling and therefore the feedback would become disused, which was the issue with the thermal feedback mechanism. In the kinetic feedback mechanism, the gas will eventually be radiated away but over longer timescales. As a result, less gas forms dense clumps and hence does not form stars. Overall, the gas loses less angular momentum producing larger discs. This model, however, does not account for a multi-phase interstellar medium.

Adiabatic Feedback

In this second model, the energy of a supernova explosion is damped to the gas as thermal energy, the same as in the kinetic feedback case, only in this method the radiative cooling is artificially turned off in the area where the supernovae explosion occurs, for a timescale long enough to allow the blast wave of the explosion to expand adiabatically and heat the medium. When applied to cosmological simulations this method of feedback has proven to be more effective than the kinetic feedback mechanism, and produces more realistic extended stellar discs as a result (Thacker & Couchman 2000). Another advantage of this model is that by temporarily preventing the hot phase created by the explosion to cool, it naturally produces a two-phase medium of hot bubbles, triggered by the supernovae, surrounding the colder gas.

2.2.5 Renormalisation Technique

Cosmological simulations, like the ones we will use throughout the thesis, need to properly compute tidal torques from the large scale structure of the Universe in order to generate the angular momentum necessary to produce galaxy-sized halos. This means that they require a large dynamical range going from Mpc scale of the large scale structure to sub-kpc scales to describe the dynamics of galaxies. However, large volume means more mass and hence high resolutions. A technique widely used in simulations of galaxy formation has been developed to overcome this issue, known as the renormalisation technique (Katz & White 1993). A low resolution dark matter only simulation is run first to redshift $z = 0$. Regions of interest where each galaxy forms, i.e. dark matter halos, are chosen and traced back to the initial conditions. The selected region in the initial conditions is then re-run only with increased resolution in this sub-region (Figure 2.2). Now the cosmological volume includes regions with varying mass and spatial resolution;

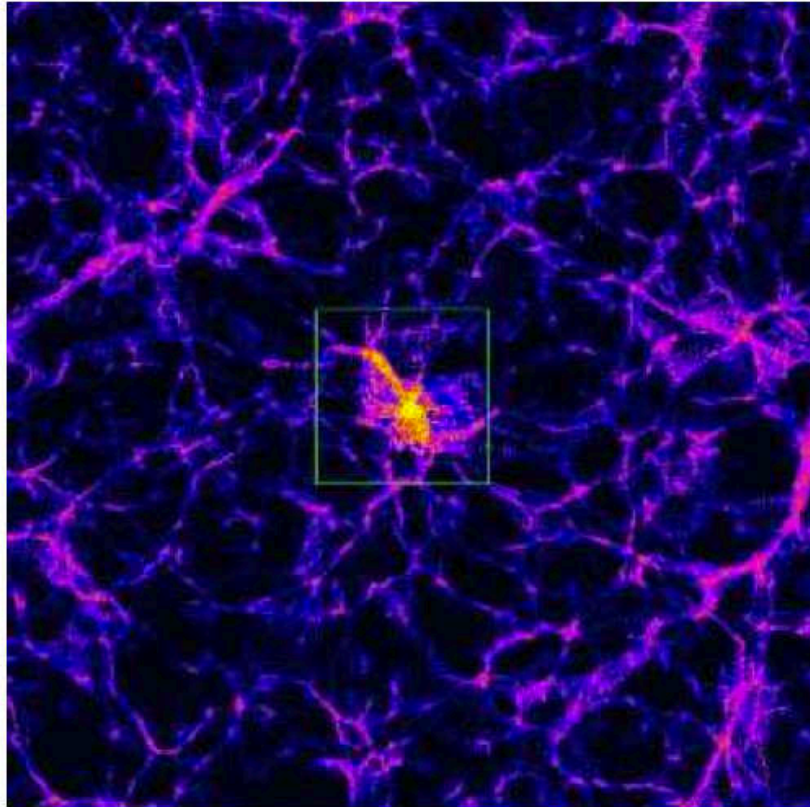


Figure 2.2: This shows an example of the renormalisation technique employed in cosmological simulations. Plotted are the dark matter particles only, showing overdense dark matter filaments merging in the hierarchical clustering process and colour coded by density. This shows the low resolution dark matter only simulation, where the region in the box is a selected dark matter halo which will be resimulated at higher resolution. This image was taken from Mayer et al. (2008).

the particle masses and their separation increases with distance from the selected region. By doing this, most of the particles are in the region of interest, for example a galaxy-size halo, making the computer time more efficient.

2.2.6 Producing Mock Images

In order to compare the photometric properties of the simulated galaxies to observed galaxies in the Universe, one can generate artificial optical images by calculating the spectral energy distributions (SEDs) using the Monte Carlo radiation transfer code called **SUNRISE** (Jonsson, 2006). The code calculates the radiative transfer through scattering and absorbing astronomical dust, which is crucial for comparing theory with observations where dust significantly affects the radiation emerging from the observed object. The outputs obtained from **SUNRISE** generate mock observations of the simulation at any wavelength from the far ultraviolet (UV) to the near infra-red (IR), mimicking band-passes of the major telescopes and observational data sets, such as **SDSS**, and the **HST**. We use this technique in the thesis to produce mock observations of certain simulated galaxies. We show an example of these mock images in Figure 2.3 of a cosmological disc galaxy simulation that we will analyse in latter chapters, showing its edge-on dust reddened i-band surface brightness map.

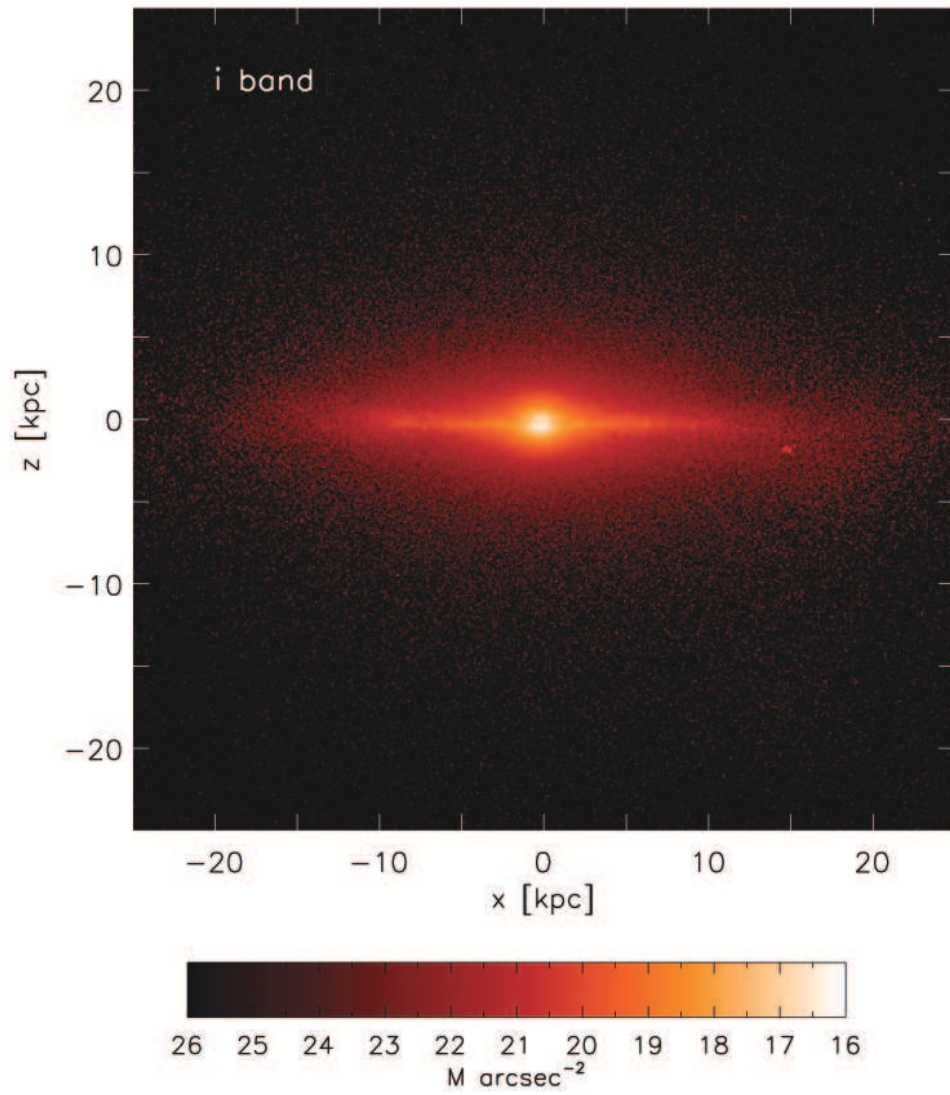


Figure 2.3: A surface brightness map using the SUNRISE code to produce mock images that mimic observations.

Chapter 3

Disc Heating

3.1 Introduction

A primary challenge facing disc galaxy formation in the Λ CDM scenario is the old age of the Milky Way’s thin disc. This seems at odds with the heating that one expects from merging and accretion events within a Λ CDM paradigm. Indeed, several studies of isolated discs being bombarded by satellites have shown that one would expect that the disc would be destroyed, or at least severely heated, by accretion events (Quinn et al. 1993; Kazantzidis et al. 2008, 2009; Read et al. 2008). Two recent studies have included gas in the main disc, with one (Moster et al. 2010) finding a significant decrease in heating, by 25% to 40% for gas fractions of 20% and 40% respectively, with the other (Purcell et al. 2010) finding that the effects of gas are somewhat less dramatic. What is clear is that all studies which use contrived initial conditions that are bombarded with satellites are necessarily restricted in their application, both for the disc and satellites. For example, how best to assign an appropriate velocity dispersion, mass, and scalelength of the Milky Way disc at redshift of two, say? Were the stars already kinematically “hot” in this early disc, or have they been heated subsequently? Idealised studies with pre-formed discs can be powerful, but they do not address

directly the issues pertaining to disc formation and how this relates to merger events as they occur within a hierarchical cosmology. Suffice to say that the existence of thin discs remains a challenge for Λ CDM cosmology. Stewart et al. (2009) argue that gas rich-mergers can explain the number of low mass galaxies on the blue sequence and mass-morphology relation, but their analysis is not able to address the issue of the thinness of the discs which survive mergers. In fact, it has been shown (Brook et al. 2004; Springel et al. 2005; Robertson & Kravtsov 2008; Governato & Brook 2009) that gas rich mergers in simulations result in hot thick discs, with thin discs forming in the subsequent quiescent period.

The degree of heating of thin disc stars is certainly complicated by an old, hot “thick disc” of stars. Observations of the kinematics of disc stars of our Galaxy have been carried out throughout the years in order to understand the mechanisms governing the formation of the disc. These studies include Nordström et al. (2004) and the follow up study by Holmberg et al. (2007), Soubiran & Girard (2005), Soubiran et al. (2008), Quillen & Garnett (2001), and Dehnen & Binney (1998). These studies however, have provided different pictures of the relationship between the ages of disc stars and their velocity dispersions (the age-dispersion relation). Quillen & Garnett (2001), using the data of Edvardsson et al. (1993), found that vertical disc heating for the Milky Way saturates at $\sigma_w \sim 20 \text{ kms}^{-1}$, with the value of dispersion virtually constant for stars of ages between ~ 2 and ~ 9 Gyr. A discrete jump is apparent for stars with ages > 9 Gyr which is generally interpreted to be the signature of the thick disc. Thus, this study supports the notion of a thick disc as a separate component to the thin disc, and suggests different formation scenarios for each component. By contrast, Nordström et al. (2004) and the follow up study of Holmberg et al. (2007) advocate a picture in which the disc has undergone continual heating over the past ~ 10 Gyr. It is not clear from these later studies whether a thick disc should be considered as

a separate component: firstly, the selection is biased toward thin disc stars, and secondly, if the thick disc is a separate component, it is possible that their result is driven by increasing contamination of their sample by thick disc stars as older and older stars are examined (Navarro et al. 2010). One of the main points of contention in such studies, and a possible explanation for the different findings, is the difficulty in determining the ages of stars (Anguiano et al. 2009; Aumer & Binney 2009). Further, Seabroke & Gilmore (2007) showed that a power law fit as suggested in the Geneva-Copenhagen studies is statistically similar to disc heating models which saturate after ~ 4.5 Gyr, and is consistent with a minimal increase of σ_w for old stars. We will compare our simulations to both these data sets.

We aim to provide further insight into the causes of the age-velocity dispersion relation of disc stars by using a suite of HPC simulations of disc galaxies, each run with a different hydrodynamical code, different initial conditions, different resolution, and different assembly histories, to sample a wide range of disc galaxy formation pathways. For this study we focus on the kinematics and heating of all stars within the disc region of our simulations, without any *a priori* distinction between the thin and thick discs. In particular, we determine whether disc stars are born hot or cold in early times, and the degree in which they subsequently heat vertically. Attention is given to any connection between heating rates and accretion histories. We will explore and discuss occasions where two components arise, in the hope of shedding light on the various scenarios which have been postulated to explain the formation of the thick and thin discs.

3.2 Simulations

For this study we analyse seven cosmological disc simulations run with different N -body hydrodynamical galaxy formation codes. We provide a summary of the

Table 3.1: Summary of the properties for the simulation suite

Name	Code	M_{vir} (M_{\odot})	Ω_0	h_0	Ω_b	t_{LMM} Gyr	ϵ (kpc)	Gas Res (M_{\odot})	Feedback
S09	RAMSES	7.6×10^{11}	0.3	0.7	0.045	2.4	0.4	1.0×10^6	kinetic
G07	GASOLINE	1.1×10^{12}	0.3	0.7	0.039	2.6	0.6	8.0×10^5	adiabatic
B09	GASOLINE	7.1×10^{11}	0.24	0.77	0.045	2.6	0.35	1.6×10^4	adiabatic
B05	GCD+	5.0×10^{11}	1	0.5	0.1	3.2	0.6	1.0×10^6	adiabatic
A03	GRAPESPH	9.4×10^{11}	0.3	0.65	0.045	6.1	0.5	2.0×10^6	kinetic
H09	RAMSES	7.6×10^{11}	0.3	0.7	0.045	2.4	0.2	1.3×10^5	adiabatic
R08	GASOLINE	1.0×10^{12}	0.3	0.7	0.039	N/A	0.05	0.2×10^5	adiabatic

main properties of each simulated disc in the following sections. For full details, references are provided.

Two of the simulations we analysed in this study are run with **RAMSES** (Teyssier 2002), which models the gas hydrodynamics using an adaptive mesh refinement (AMR) scheme, while the other codes use a smoothed particle hydrodynamics (SPH) approach, both of which have been discussed in Chapter 2. Using examples drawn from these different fundamental approaches should provide greater confidence in the robustness of our results. To the best of our knowledge, our study is the first to compare properties of simulated disc galaxies formed using these two commonly-adopted methodologies.

All simulations (except R08) have cosmological initial conditions where small scale structures merge to form increasingly larger objects in the Universe as part of the so-called hierarchical framework. They all have a similar Milky Way-type mass halo and all the different codes self-consistently include the primary physical processes needed to model galaxy formation and evolution. These consist of the effects of gravity, hydrodynamic pressure and shocks, star formation and feedback, radiative cooling, and a photoionising UV background. They all adopt a type of Schmidt law for converting gas particles into stars, where the star formation rate is proportional to the gas density to some power.

The main difference between the simulations is that they have different initial

conditions, and hence merger and assembly histories. They also adopt different recipes for feedback from Type II supernovae (SNeII). Two of our simulations use kinetic feedback, while the rest use an adiabatic approach. Pure “thermal feedback” is used in the case of Type Ia supernovae (SNeIa), where the longer lifetimes of the progenitors (relative to SNeII) means that the energy is not released into the same high density regions from which the stellar particles formed (and hence, the associated energy is not radiated away as efficiently as for the case of SNeII).

Each of the simulations employ star formation recipes, as described in detail in Chapter 2, which are similar in all cases; stars can form only from gas above a certain density threshold. Since cosmological simulations typically lack resolution below a few hundred parsecs, this sets a maximum density that the simulations can resolve on the order of 0.1 cm^{-3} ; all of simulations here adopted this star formation threshold. We shall discuss the impact of this threshold selection in Chapter 4.

The main properties of each of our simulations are presented below, and summarised in Table 3.1.

3.2.1 S09_YCosm_AMR_RAMSES

We ran a high-resolution fully-cosmological (YCosm) disc simulation to redshift zero using the adaptive mesh refinement (AMR)-based code **RAMSES** (Teyssier 2002). The supernova feedback (SN) is modelled by directly injecting kinetic energy into the surrounding gas – i.e., kinetic feedback.

The simulation (S09, hereafter) was run within a “concordance” cosmology framework, with $\Omega_0 = 0.3$, $h_0 = 0.7$, $\Omega_b = 0.045$, and $\Omega_\Lambda = 0.7$. Preliminary analysis for this simulation was presented in Gibson et al. (2009), while its optical properties were categorised extensively by Sánchez-Blázquez et al. (2009). The

simulated disc had its last major merger (LMM, defined as having total mass ratio of 1:3 or higher) at a redshift of $z = 2.6$, i.e. $t_{LMM} = 2.4$ Gyr (where t_{LMM} is time of the last major merger), however, interactions with smaller satellites still occur at lower redshifts. We discuss the LMM later in the paper. Its final virial mass is $7.6 \times 10^{11} M_{\odot}$ at $z = 0$.

3.2.2 G07_YCosm_SPH_GASOLINE

This galaxy is the simulation denoted as MW1 in the work of Governato et al. (2007), and is referred to as G07, hereafter. The code used for this fully-cosmological (YCosm) simulation is the smoothed particle hydrodynamics (SPH) code `GASOLINE` (Wadsley et al. 2004). The SN feedback mechanism uses an adiabatic feedback approach where cooling was stopped artificially to allow blast waves from SNe to expand and heat the surrounding interstellar medium (ISM). In all the simulations run with `GASOLINE` presented here, 40% of the SNe energy is coupled to the surrounding gas. Such a prescription results in a decrease in the amount of gas cooling early in the galaxy’s formation, reducing the loss of angular momentum resulting from the merging of dense stellar systems.

The simulation employed was run within a concordance cosmology with $\Omega_0 = 0.3$, $h_0 = 0.7$, $\Omega_b = 0.039$, and $\Omega_{\Lambda} = 0.7$; the last major merger was at redshift $z=2.5$, i.e. $t_{LMM} = 2.6$ Gyr, with several late minor interactions thereafter. The final virial mass is $1.1 \times 10^{12} M_{\odot}$.

3.2.3 B09_YCosm_SPH_GASOLINE

This simulation was also run with `GASOLINE` and was previously studied in Brooks et al. (2009), and is referred to as B09, hereafter. The simulation was run in a concordance cosmology, with $\Omega_0 = 0.24$, $h_0 = 0.77$, $\Omega_b = 0.045$, and $\Omega_{\Lambda} = 0.76$. The redshift of LMM is also at $z=2.5$, i.e. $t_{LMM} = 2.6$ Gyr, but unlike the case

for G07, this simulation experiences no mergers or accretion events since $z \approx 0.7$ or $t = 7$ Gyr. The force resolution is also somewhat higher than for G07.

3.2.4 B05_NCosm_SPH_GCD+

This simulation was taken from the work of Brook et al. (2004, 2005) called SGal1, and is referred to as B05, hereafter. The SPH code GCD+ (Kawata & Gibson 2003) was employed, although this particular run was not fully cosmological (NCosm). Semi-cosmological models, like B05, consist of an isolated sphere of dark matter and gas instead of a large cosmological volume. Small-scale fluctuations are superimposed on the sphere to allow for local collapse and subsequent star formation. Solid-body rotation is also applied to the sphere to incorporate the effects of longer wavelength fluctuations that a semi-cosmological model does not otherwise account for. Feedback from SNeII was assumed to be adiabatic, with cooling turned off in the surrounding gas.

The cosmological framework in which B05 was run is quite different from the simulations discussed thus far; specifically, it used $\Omega_0 = 1$, $h_0 = 0.5$, $\Omega_b = 0.1$, and $\Omega_\Lambda = 0$. While using the currently favoured Λ CDM framework would have a significant impact upon simulations of large-scale structure formation from Gaussian random noise initial conditions, it has been shown that, within the context of single galaxy formation models such as B05, the resulting differences are negligible (Brook et al. 2005). In terms of its merger history, B05 is not dramatically different from B09, in the sense of their being little or no merger activity since redshift $z \approx 0.5$ or $t = 7$ Gyr.

3.2.5 A03_YCosm_SPH_GRAPESPH

This simulation (hereafter referred to as A03) was first presented in Abadi et al. (2003a,b). It is a fully-cosmological (YCosm) Milky Way-like disc galaxy, simulated with the GRAPESPH code (Steinmetz 1996). Feedback is predominantly thermal, with 5% of supernova energy converted into kinetic feedback and injected into the surrounding gas particles. A flat Λ CDM cosmology was assumed, with $\Omega_0 = 0.3$, $h_0 = 0.65$, $\Omega_b = 0.045$, and $\Omega_\Lambda = 0.7$. Its final virial mass was $9.4 \times 10^{11} M_\odot$ and its last major merger occurred at $z = 1$, i.e. $t_{LMM} = 6.1$ Gyr, although a number of minor interactions occur thereafter.

3.2.6 H09_YCosm_AMR_RAMSES

This simulation (H09, hereafter) traces the same halo as S09_YCosm_AMR_RAMSES described in § 3.2.1, but run with a higher spatial resolution, and employing a different feedback mechanism for SNeII. Instead of using kinetic feedback as in S09, it relies on an adiabatic feedback scheme.

3.2.7 R08_NCosm_SPH_GASOLINE

This simulation (R08, hereafter) is taken from Roškar et al. (2008). It is an isolated Milky Way-type disc galaxy ($1.0 \times 10^{12} M_\odot$) with solid body rotation added, similar to the B05_NCosm_SPH_GCD+ simulation; where it differs from the latter is that R08 does not incorporate small scale density fluctuations. This means that this isolated simulation experiences no merger or accretion events. It is evolved for 10 Gyr using the same GASOLINE code as G07 and B09, but at extremely high spatial resolution (softening length of 50 pc).

The simulations described above are Milky Way-*like*, which means they are disc galaxies similar to the Milky Way but are not exact replicas of it. Part of our study compares these cosmological simulations with observations of our Galaxy

Table 3.2: Structural parameters of the simulation suite.

Name	M_{vir} (M_{\odot})	R_d (kpc)	z_d (kpc)
S09	7.6×10^{11}	2.17	1.02
G07	1.1×10^{12}	2.33	1.21
B09	7.1×10^{11}	2.46	0.91
B05	5.0×10^{11}	2.68	0.80
A03	9.4×10^{11}	2.68	1.21
H09	7.6×10^{11}	2.50	0.88
R08	1.0×10^{12}	3.34	0.40

in order to try and constrain some of the properties of numerical simulations. In order to justify our comparison somewhat, we measure the disc scalelengths for each simulation, summarised in Table 3.2, to show that they are comparable to one another and are similar to scalelength obtained for the Milky Way’s disc.

3.3 Disc Heating

For observed solar neighbourhood stars, it is well established that there is a relationship between their velocity dispersion and age. We refer to the increase of the dispersion with time as *disc heating*, where the relationship for the solar neighbourhood indicates that the older disc stars are kinematically “hotter” than its younger counterparts. Examining the dynamics of stars as a function of time therefore contains valuable information about the heating processes - driven by some combination of secular and satellite merger-driven phenomena. We focus on the vertical heating (σ_w , perpendicular to the plane of the galaxy) as this out-of-plane heating is more susceptible to mergers/interactions. In-plane heating (σ_u and σ_v) is more sensitive to spiral wave and bar-driven heating which are not resolved in the current cosmological simulations we analyse here. Further, Seabroke & Gilmore (2007) showed that dynamical streams can contaminate the

local in-plane velocity distributions, which can complicate and compromise the comparison with simulated in-plane velocity distribution functions which do not capture adequately structure on that scale.

In what follows, we first examine the velocity-dispersion age relation, similar to the manner by which observers study the same relation within the Milky Way, but now for stars within the simulated discs at $z = 0$. When considering the relation between dispersion and age, an ambiguity remains: old stars may have higher velocity dispersion due to being born already kinematically hot, or they may be born cold but are then heated subsequently. Therefore, since the dispersion of stars at $z = 0$ does not provide direct information as to the velocity dispersion of the population *at birth*, we extend our analysis to study the time evolution of the heating of sub-populations of disc stars. Specifically, we will attempt to ascertain whether stars which are kinematically hot *today* were “born hot” or were “born cold and heated” (by whatever means), thereafter. Finally, once identified, we will trace the heating history of stellar populations born at different epochs, in each of our simulations. Armed with this information, we will try to shed light on processes which result in the observation that older stars are kinematically hotter than young stars.

3.3.1 Age-Velocity Dispersion Relation

We first examine the velocity dispersion perpendicular to the plane of the galaxy (σ_w) for all stars at $z = 0$ within the “local” disc, which we define as $7 < R_{xy} < 9$ kpc and $|z| < 1$ kpc, as a function of age (Fig 3.1). That is to say, “young stars” have “small ages”, in Fig 3.1, and “old stars” have “large ages”. With such a selection function, all the simulations show little in the way of evidence for stellar heating for young stars with ages ~ 1 to ~ 3 Gyr, as well as much higher dispersions for old stars (consistent with observations of the Milky Way).

We should point out that for the semi-cosmological simulation, B05, we used a slightly larger radial cut of $4 < R_{xy} < 8$ kpc and $|z| < 1$ kpc due to the smaller number of star particles in this particular run. We found that in the smaller region of $7 < R_{xy} < 9$ kpc, there were not enough stars for some age bins to measure an accurate velocity dispersion. We were therefore forced to use a larger region for this simulation. However, we also tested our results in all the simulations for three different radial cuts to ensure that the trends remain the same independent of the precise volume analysed.

The simulations show broad similarities in their heating profiles, all showing increased dispersion with age, but also there are differences in the degree and nature of the heating that we will explore. Broadly speaking, while there is a continuum of heating “profiles” on display in Figure 3.1, at one end of the spectrum, several of the simulations (e.g., S09, H09, G07) show a temporal heating profile which becomes apparent at younger ages (~ 3 Gyr) relative to several at the opposite end of the spectrum (e.g., B05, B09) which only begin to show evidence of significant heating in older stars (> 6 Gyr). If we associate these relatively flat periods at late times with the thin disc, then none of the simulations have thin discs as old as that of the Milky Way, which is considered to be between 8-10 Gyr old.

The S09 and H09 simulations show little sign of heating for stars younger than ~ 3 Gyr; for older stars, several discrete “jumps” in velocity dispersion can be discerned. Similar trends and small discrete jumps are also seen in the G07 simulation, in addition to a discontinuity in the dispersion for stars of age ~ 8 Gyr. The latter can be traced to a period of enhanced merger activity early in the galaxy’s evolution, just prior to the establishment of its stable disc.

Like all the simulations, A03 also shows dispersion trends consistent with the signature of continual/secular heating at later times. Stars older than ~ 9 Gyr,

in particular, possess a significantly large velocity dispersion. These high dispersions are a signature of the so-called “angular momentum problem” mentioned in Chapter 1 and 2, which results in the formation of an overly-dominant spheroid compared to observations. The spheroid component is dominated by old stars which are ultimately the responsible agents in the production of the high dispersions seen to the right-hand side of Figure 3.1.

The absence of significant heating seen in all simulations for stellar ages of $\sim 1\text{-}3$ Gyr extends to somewhat older stars (up to ~ 6 Gyr in age), for both B09 and B05. For older stars, discrete jumps in the dispersion, superimposed upon a continual heating profile, are evident. The longer period during which stars show little heating is reminiscent of the Quillen & Garnett (2001) interpretation of extant observations that this reflects “saturation” in the thin disc’s kinematic heating. The older, kinematically hotter, stars in these simulations have been suggested to be a signature of the thick disc (e.g., Brook et al. 2004).

One of the natural consequences of the merging which occurs within the hierarchical clustering paradigm is a degree of kinematical heating. As such, we set out to examine the merging histories for each of the simulations, to see whether they shed light on the characteristic heating profiles and discrete “jumps” seen in the age-velocity dispersion plane (Figure 3.1); these merging histories will be discussed shortly.

3.3.2 Stars Born in the Disc

One thing which is readily apparent from our analysis is that *all* of the simulations show much higher velocity dispersions for the older stars in the disc, consistent with the behaviour seen in the Milky Way. That said, there is also a consistent offset, in the sense that all of the simulated discs are substantially hotter than that of the Milky Way. Part of this discrepancy relates to the fundamental problem in

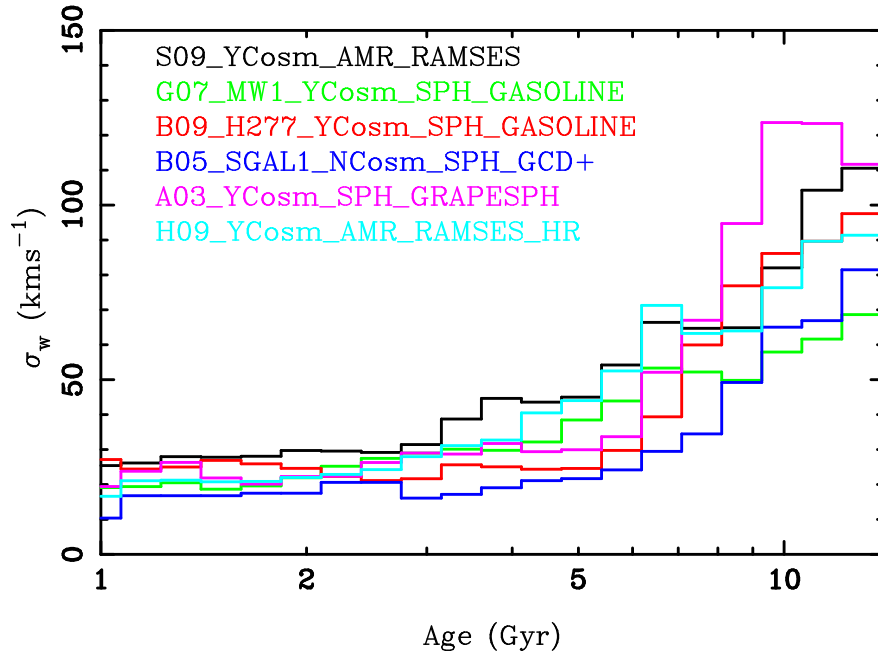


Figure 3.1: Age-velocity dispersion relation in the vertical direction for “local” disc stars in our suite of simulations.

cosmological simulations, specifically, that gas cools efficiently allowing baryons to collapse early during the merging process of galaxy formation, resulting in unrealistically large spheroidal components. These old spheroidal stars can have a significant impact on the derived dispersions, in the sense of “contaminating” what one would like to be a “pure” disc sample. In other words, rather than measuring the dispersion of disc stars, which reflects the observational case, one is instead probing the additional impact that the dispersion of the spheroid stars have upon the sample. This is problematic, at some level, for all of the simulations - it is reflected in the very high dispersions seen at large ages in Figure 3.1. In order to make a fair comparison with disc stars from the Milky Way, we clean (in a very straightforward manner) our sample of these spheroidal contaminants by selecting *in-situ* stars, i.e. those that are born in the central galaxy. These *in-situ* stars are identified as those which form anywhere within the central galaxy, while

stars that end in the central galaxy at $z = 0$ but were born within a satellite or substructure are called *accreted*. We then derive the velocity dispersions of *in-situ* stars in our disc defined region, $7 < R_{xy} < 9$ kpc and $|z| < 1$ kpc, at $z = 0$.

By selecting *in-situ* stars we are examining the heating of disc stars. Whether this results in forming the thick disc or merely the old, hot thin disc, is left open to interpretation. Of the thick disc formation mechanisms proposed (see Chapter 1), the direct accretion of satellites scenario is thus not explicitly addressed in this part of the study. In this analysis we merely assume that a rotationally supported disc forms *in-situ* and can be born relatively hot or cold, and then may be heated by a number of processes. Further, recent simulation results have shown that some *in-situ* stars will form part of the stellar halo (Zolotov et al., 2010), and thus may affect our dispersion results. However, these stars are in the halo, with too few in our defined disc region to affect the dispersion-age plots presented here.

We plot in Figure 3.2 the age-dispersion relation of these *in-situ* stars from the simulations along with three sets of observational data for the Milky Way disc: Quillen & Garnett (2001), a combined set from Soubiran & Girard (2005) and Soubiran et al. (2008), and Holmberg et al. (2008). Quillen & Garnett (2001) use a sample of 189 nearby F- and G-dwarfs from Edvardsson et al. (1993); from their resulting σ -age relation, they suggest that the Milky Way disc has been relatively quiescent with little heating for stars with ages between 3 and 9 Gyr, with stars older than that having been subject to an abrupt heating event. The second set of observational points is taken from Soubiran & Girard (2005) and Soubiran et al. (2008). We have merged these two catalogues, in order to include a larger number of old disc stars in the sample. We note that this data includes the Reddy et al. (2003), Bensby et al. (2003) and Bensby et al. (2004) samples, which target the thick disc specifically by using a kinematic selection, and this is the reason that their old stars are hotter than in the Holmberg et al. (2008) samples.

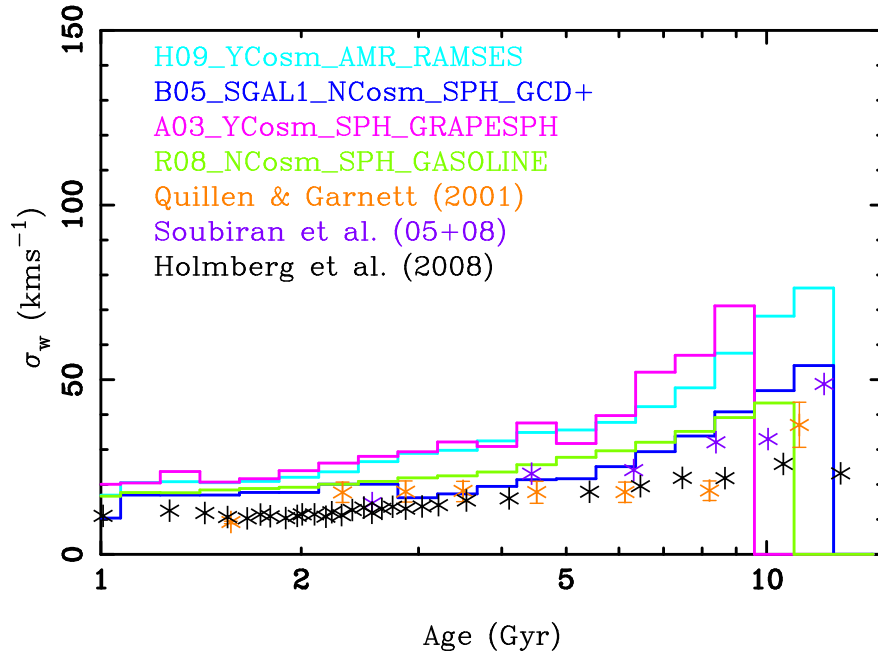


Figure 3.2: Vertical age-velocity dispersion relation for *in-situ* disc stars within our suite of simulations, compared with observations from Quillen & Garnett (2001); Soubiran & Girard (2005); Soubiran et al. (2008); and Holmberg et al. (2008).

Their analysis is consistent with that of Quillen & Garnett (2001), where the age-velocity relation of the thin disc is characterised by the saturation of the vertical dispersion at $\sim 25 \text{ km s}^{-1}$ at ages $\sim 4\text{--}5$ Gyr. The final set of observations is that from Holmberg et al. (2008); they present a sample of F- and G-dwarfs from the Geneva-Copenhagen Survey of the solar neighbourhood (Nordström et al. 2004, GCS) suggestive of a scenario consistent with continual heating of the local disc throughout its entire lifetime.

By only considering *in-situ* disc stars, we have eliminated a significant fraction of the high dispersion old spheroidal components' contaminants; this is reflected in the $\sim 20\text{--}30\%$ decrease in σ_w for stellar ages in excess at $\sim 7\text{--}8$ Gyr. We have only included four of the simulations in Figure 3.2, although the results that follow apply to the entire suite. The overall trend in Figure 3.2 matches that

of Figure 3.1, in the sense that a range of heating “profiles” are seen, with both continual and discrete events being evident.

We also compared the velocity dispersions in Figure 3.2 in three different regions for our highest resolution simulations (so H09, R08 and B09, with selected regions being $4 < R_{xy} < 8$ kpc, $6 < R_{xy} < 9$ kpc, and $7 < R_{xy} < 9$ kpc). These simulations have enough stars to examine much smaller volume cuts. We found that the trends in velocity dispersion remain the same, independent of radial cut, with quantitative differences in Figure 3.2 being insignificant.

It might be argued that the three simulations with the (relatively) oldest cold disc component (B09, B05, R08) - also, those with relatively flat σ -age relations for ages up to ~ 6 Gyr - are a somewhat better reflection of the relation inferred from the observations. We will show in § 3.3.4 that the merger history of these systems is a primary driver in the establishment of this relationship, and examine the role played by numerical effects.

An interesting observation from Figure 3.2 is that there is a significant offset, even when including just *in-situ* stars, with all simulations compared with observations at any time in the galaxy’s evolution, in the sense that the stars in the simulations are hotter than the observed stars at all times (with the exception of the semi-cosmological simulation, B05). This offset is particularly high when looking at old stars but is also significant for young stars. Several possibilities might be responsible for driving such a discrepancy: (i) numerical heating due to limited force resolution, (ii) the treatment of heating and cooling within the ISM of the simulations, and (iii) the adopted low star formation threshold.

The issue of numerical heating will be addressed at length in Chapter 4; here, we simply note that the offset also exists in the simulation of Roškar et al. (2009), which has a force resolution of 50 pc, and it also exists in other high resolution isolated disc simulations in the literature (e.g., Kazantzidis et al. 2008,

2009; Stewart et al. 2009). In Figure 3.2, one can view our highest resolution simulation (R08), as well as our lowest (B05); if numerical heating was the main agent of the observed offset between the simulations and observations, one might expect the lowest resolution simulation to be (kinematically) the hottest. This is not the case though and, in fact, B05 has the lowest resolution and is the coldest in the sample.

Another important aspect to consider is the effect of secular heating; R08 has sufficient resolution to account for heating from internal processes such as from spiral arms. As the simulation is isolated and therefore removed from a cosmological context, the observed heating profile in this simulation must be secular due to spiral arms directly heating stars as well as causing migration (Loebman et al., 2010). For the R08 simulation, these internal heating processes *alone* are enough to match the observations of Holmberg et al. (2008).

3.3.3 Disc Heating

In this section, we aim to answer several questions that emerged from the above kinematical analysis of $z = 0$ stars: were the kinematically hot, old, stars in Figures 3.1 and 3.2 born with these high velocity dispersions, or were they born “cold” and heated subsequently? If the latter, then what is the source of this heating? To answer these, we examine the kinematics of disc stars at the time of their birth for different epochs of a galaxy’s formation. We do this by selecting disc stars born in the “disc” region, $4 < R_{xy} < 8$ kpc and $z < 1$ kpc, at the time of their birth, using a fairly arbitrary time “slice” of 200 Myrs - i.e., we are deriving the velocity dispersion of young disc stars in each simulation at various epochs. We tested our results with different radial cuts and age range, and found that our results and conclusions are not reliant on the used values. The slightly larger radial slice used in this section allows us to obtain a larger sample of stars to

derive their dispersions.

Figure 3.3 shows the derived velocity dispersions for young stars at different times throughout the respective simulations' evolution. Each of the orthogonal components of σ are highlighted, although as noted earlier, our analysis will concentrate solely upon σ_w . For clarification, stars born at early times are situated to the left of each panel in Figure 3.3, while stars born more recently are located towards the right - i.e., the abscissa now reflects “time” rather than “stellar age” (as was employed in Figures 3.1 and 3.2).

For the S09 simulation (top left panel of Figure 3.3), all disc stars, independent of time, are born cold with low vertical velocity dispersions of $\sigma_w \approx 30 \text{ kms}^{-1}$, on average. There is a slight increase in the dispersion for stars with formation times between ~ 7 and 10 Gyr, where the dispersion increases by $\sim 25\%$. This epoch corresponds to a period of enhanced minor merger activity, during which the ISM is heated kinematically relative to the adjoining quiescent phases.

For the G07 simulation (top right panel of Figure 3.3), stars are born on average with vertical velocity dispersions between $\sigma_w = 20$ and $\sigma_w = 30 \text{ kms}^{-1}$, except for the period between ~ 3 and 5 Gyr. During this time there are several minor mergers with satellites which result in these stars being born with velocity dispersions roughly twice that of the adjoining phases ($\sigma_w = 60 \text{ kms}^{-1}$). It is also important to note that these mergers produce a short-lived warp at $z = 2$ - i.e., at $t = 3.2$ Gyr. The stars that we detected in the disc during this period were located within this warp region. Because of their potential to dominate over in-plane stars at only a few scalelengths, stars in the warp should be treated carefully, particularly in the case of studying their kinematics, as they can result in an apparent increase in the velocity dispersion (Roškar et al. 2010). These “warp” stars are kinematically “disturbed” and born with higher σ_w . This is a very similar trend to that seen in the H09 simulation (bottom right panel of

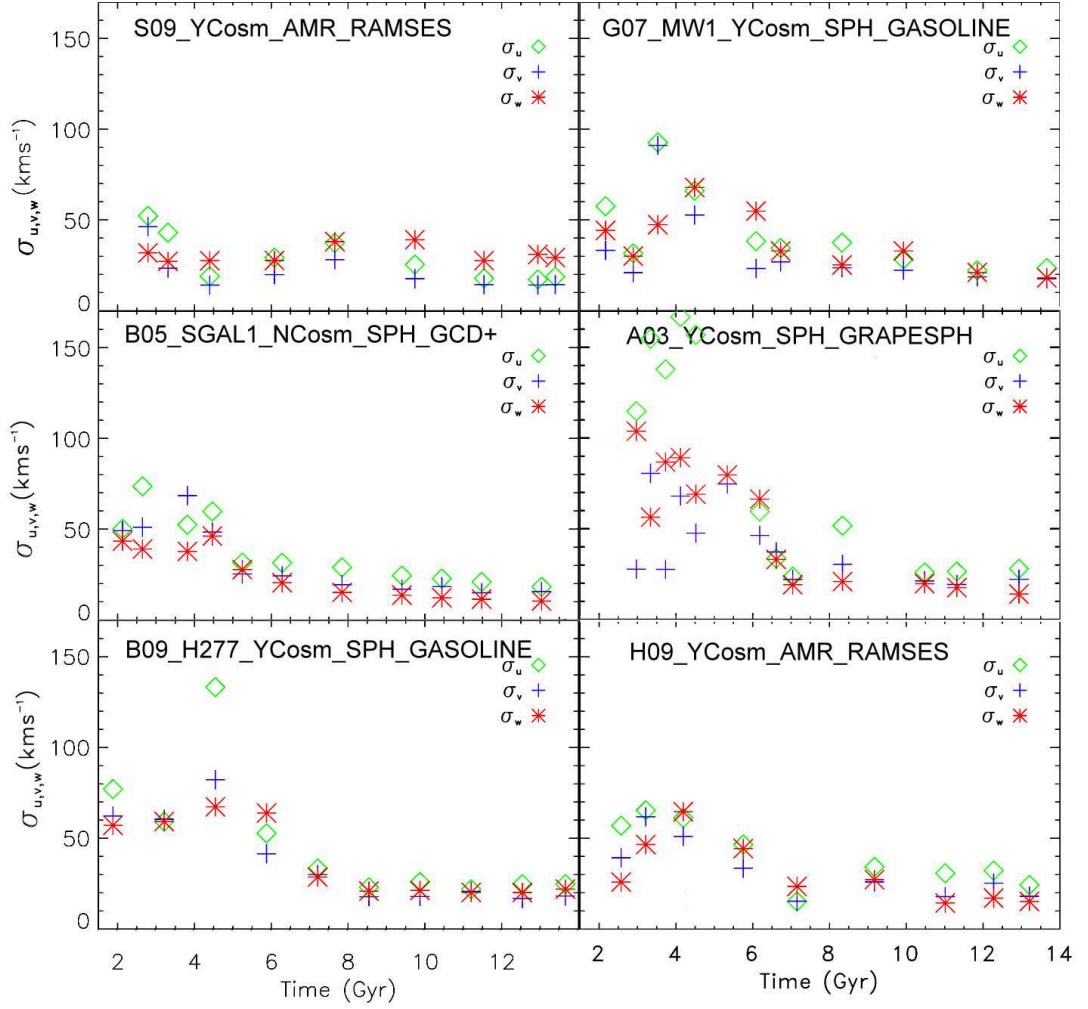


Figure 3.3: Radial, tangential, and vertical velocity dispersion components (σ_u , σ_v , and σ_w , respectively) for young stars (<200 Myrs) at the time of their birth for different epochs, within the defined disc annulus $4 < R_{xy} < 8$ kpc and $|z| < 1$ kpc.

Figure 3.3) where stars, on average, tend to have dispersions between $\sigma_w = 20$ and $\sigma_w = 30 \text{ kms}^{-1}$ at the time of birth, but there is a period between ~ 3 and 5 Gyr, again, where this dispersion doubles to about $\sigma_w = 60 \text{ kms}^{-1}$. As for G07, this period coincides with an epoch of enhanced satellite interaction with the main galaxy, although in G07 the warp is the primary cause of the high velocity dispersion during this period and not the minor mergers.

A distinct trend is noticed for the B09, B05, and A03 simulations. Stars born at late times (over the past ~ 6 Gyr) are born cold, with velocity dispersions between 10 and 20 kms^{-1} , while stars born prior to this are born hot (with vertical velocity dispersion of $\sim 70 \text{ kms}^{-1}$). It is tempting to interpret this as the signature of separate thin and thick discs, where the thick disc is composed of older stars which were born hotter than the younger, colder, thin disc (Brook et al. 2004).

The high velocity dispersion measured at early times in A03, i.e. from ~ 2 to 6 Gyr, is due to the numerous merger events that this simulation undergoes at early times (see Abadi et al. 2003a). The feedback mechanism is not particularly effective and therefore the satellites that merge with the main galaxy contain a large stellar component, which affect the high velocity dispersions derived. We address this issue later in Chapter 5. The merger activity is largely over by ~ 6 Gyr and the disc is allowed to settle and form. The low velocity dispersion that stars have at birth in Figure 3.3 from $t = 6$ Gyr onwards can be interpreted as a signature of the formation of such disc after the merging epoch is over.

Having identified the velocity dispersions of stars *at birth*, we now wish to determine whether they maintain the self-same dispersion as they age - i.e., are these stars being heated with time? We do this by selecting the same “young” stars at a particular time and then tracing them forward in time, in order to quantify the degree of evolution in the velocity dispersion of these ensembles of stars. This is shown in Figure 3.4, where the evolution of the velocity dispersion

of stars born at each epoch is represented by the coloured curves. Because we are interested in stars born in the disc of the galaxy we necessarily choose epochs after the disc has formed, with the exception of A03 where the disc forms much later compared to the other simulations. For each galaxy this time can vary depending upon the time of the last major merger. We therefore do not look at stars beyond $z \sim 2.5$ (or before $t = 2 \text{ Gyr}$) because, in general, the discs in these galaxies have not yet formed.

Looking first at the S09 simulation, the stars born at $t = 2.5 \text{ Gyr}$ have an initial velocity dispersion of $\sigma_w = 30 \text{ kms}^{-1}$, increasing to $\sigma_w = 70 \text{ kms}^{-1}$ over the subsequent $\sim 2 \text{ Gyr}$. This behaviour is qualitatively repeated for all stars born (and tracked) in the first $\sim 6 \text{ Gyr}$: i.e., stars are born relatively cold but rapidly heat to more than double their initial velocity dispersion within $\sim 1 \text{ Gyr}$, before the heating begins to “saturate”, while stars born over the past $\sim 6 \text{ Gyr}$ (while also born “cold”) heat much more gradually. Indeed, stars born over the last $\sim 4 \text{ Gyr}$ experience essentially no kinematic heating.

G07 presents a qualitatively similar heating profile to that of S09, in the sense of (a) older stars experiencing a doubling of their vertical velocity dispersion in the first few Gyr after birth, before the heating saturates, and (b) younger stars experiencing little, if any, kinematical heating. One subtle difference between G07 and S09, though, is that older stars in the former are born relatively hot compared with their younger counterparts, while in S09, all stars, independent of birth epoch, are born with essentially the same vertical velocity dispersion.

A03 is similar to G07 in the sense that older stars are born relatively hot compared with the younger stars in the disc. The difference in this simulation compared to both S09 and G07 is that the younger stars also experience heating, where their dispersions double in the first few Gyr. It can be seen that even stars born at $t = 13 \text{ Gyr}$ are being heated with time (see red curve in middle right

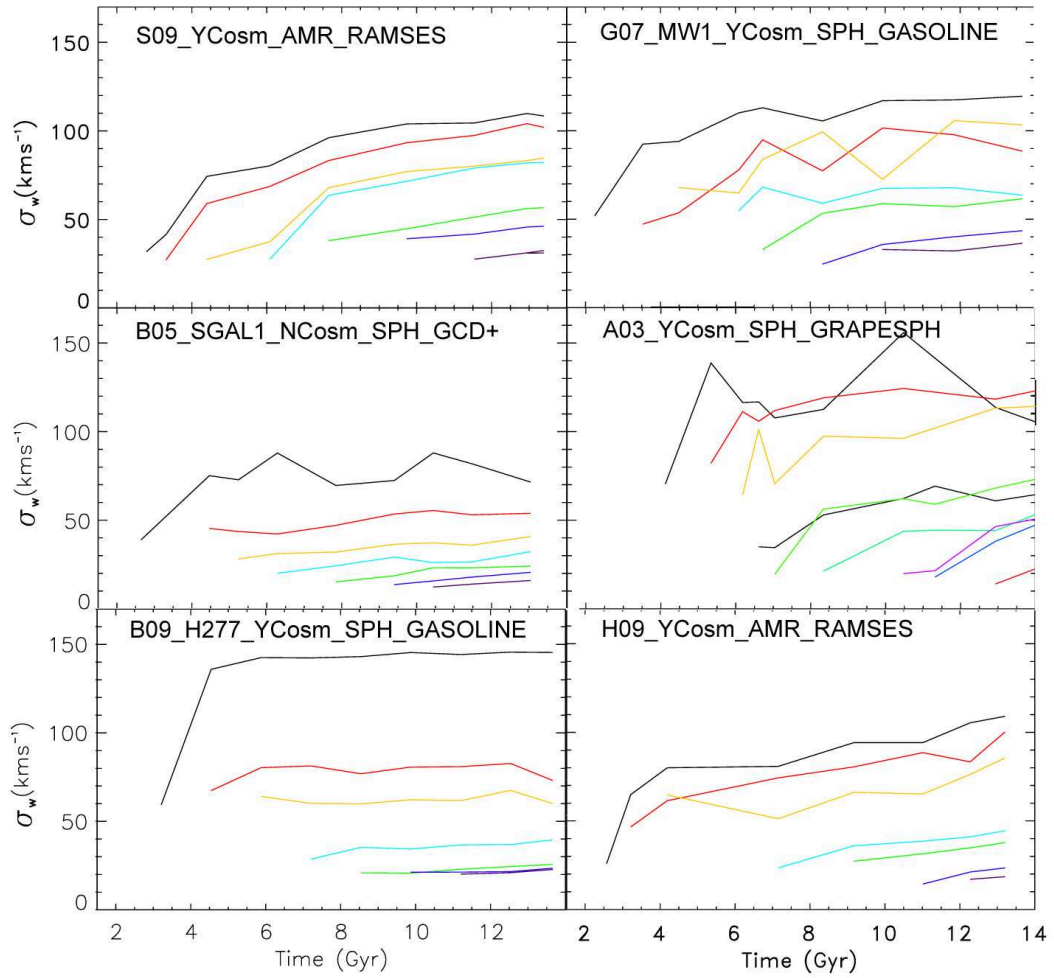


Figure 3.4: Velocity dispersion perpendicular to the plane (σ_w) of young stars (ages < 200 Myrs) at various epochs (represented by different colours, and different starting times), traced forward in time to quantify their temporal heating profile.

panel of Figure 3.4).

Both B09 and B05 present somewhat different heating profiles. With the exception of the first epoch in both (coinciding with the time of the last major merger in both cases), the vertical velocity dispersion is essentially invariant - i.e., older stars (which are born hotter than their contemporary counterparts, as in G07) and younger stars maintain their birth velocity dispersion for the lifetime of the simulation.

The next questions that need addressing are: what are the responsible agents driving the assorted heating profiles seen in Figure 3.4? What is the quantitative relationship to their respective merger histories? Is the effect of warps playing an important role? Are numerical effects plaguing the analysis? We address these over the following sub-sections.

3.3.4 The Effects of Mergers

As noted above, our efforts have concentrated upon the out-of-plane heating within the simulations, due to its stronger sensitivity to mergers and interactions. It is crucial to derive and quantify the merger histories of our simulations, in order to link the observed heating trends with the interactions they have experienced during their evolution.

We have already seen indirect signatures of mergers in the above analysis. Stars born with hotter kinematics during early stages of a galaxy's evolution (Figure 3.3), as well as the dramatic heating of stars born at early times over fairly short timescales (Figure 3.4), can be related to the last major merger (LMM) of each galaxy (see Table 3.1 for the time, t_{LMM} , at which the LMM occurred for each simulation). Major mergers are defined to have a total mass ratio of 3:1 or higher.

In what follows, we examine minor mergers of satellites with mass $\geq 4\%$ the

mass of the disc at the time of the merger, back to $z \sim 2$. Such mergers are able to disturb disc structure (Quinn et al. 1993). We are, unfortunately, limited by time resolution due to the available number of outputs for each simulation. We are thus not able to trace directly the trajectories of the satellites and determine whether they penetrate the disc, or the number of close passages which occur prior to the final coalescence. We restrict our analysis to satellites which have contributed stars to the inner 10 kpc of the central galaxy by $z = 0$, indicating that these satellites have interacted with the disc.

The last major merger in the S09 simulation occurs at time of $t_{LMM} = 2.4$ Gyr in Figure 3.3. It has a mass ratio of 3:1 ($M_{vir}=9 \times 10^{10} M_{\odot}$ and $M_{sat}=2.9 \times 10^{10} M_{\odot}$). This major merger heats the disc stars significantly as can be seen in the black line in the top left panel in Figure 3.3. After the LMM there are several minor baryonic mergers, the most noteworthy of which occurs between redshifts $z=0.8$ and $z=0.7$ (a time corresponding to ~ 6.3 Gyr in Figure 3.3). This minor merger has a mass ratio of 8:1 ($M_{vir}=5.7 \times 10^{11} M_{\odot}$ and $M_{sat}=6 \times 10^{10} M_{\odot}$). Stars born during this period are somewhat hotter kinematically-speaking, relative to those born before and after (Figure 3.3). In addition, stars born in the preceding ~ 3 Gyr to this merger appear to have been subject to rapid heating (see the yellow and cyan lines in upper left panel of Figure 3.4). Additional (less significant in terms of mass) mergers occur at redshift $z = 1.75 - 1.44$, i.e. $t = 4 - 4.5$, with a mass ratio of 16:1. The effects of these mergers are not obvious in our plots, although the impact of the former likely plays a role in the heating seen between times 3 and 4 Gyr in the upper left panel of Figure 3.4. This simulation undergoes minor mergers up to redshift $z = 0$.

G07 undergoes its LMM at time $t_{LMM} = 2.6$ Gyr, in Figure 3.3. This major merger has a mass ratio of 4:1 ($M_{vir}=9 \times 10^{10} M_{\odot}$ and $M_{sat}=2.5 \times 10^{10} M_{\odot}$), where the heating caused by this merger can be seen in the increase in the dispersion

for stars during this period (see black line in top right panel from Figure 3.3). It undergoes several minor mergers at time $t = 3.2$ Gyr with mass ratios of 10:1 and 15:1, the effects of which can also be seen in Figure 3.3 and 3.4. Hereafter, it undergoes minor interactions the last one occurring at $t = 7.68$ Gyr. These interactions are apparent near $t = 8$ Gyr in Figure 3.3 and 3.4, although their heating “impact” is not particularly obvious in Figure 3.3 - i.e., the stars born at $t = 8$ Gyr (upper right panel of Figure 3.4) are not kinematically hotter than those born within ~ 2 Gyr of these mergers; similarly, the impact on the heating of these stars is not particularly dramatic (upper right panel of Figure 3.4). The effect that the LMM (at $t \sim 2.6$ Gyr) has in heating the ISM of G07 is felt over the subsequent ~ 3 Gyr (Figure 3.3), and impacts upon the temporal heating profiles of stars born during this period as well (Figure 3.4). G07 hosts fairly significant warps during and after these periods of merger-driven activity. As noted previously in § 3.3.3, warps can result in an increase in the velocity dispersion of stars, which are kinematically disrupted by the warp (Roškar et al. 2010).

For B09 there is a clear distinction between stars born at early times and those formed at later times, which can be ascribed to the simulation’s merger history. The LMM in this simulation occurs at a time of $t_{LMM} = 2.6$ Gyr in Figure 3.3 and has a mass ratio of 3:1 ($M_{vir} = 6 \times 10^{10} M_{\odot}$ and $M_{sat} = 2 \times 10^{10} M_{\odot}$). During the period between $t = 2$ and 3.4 Gyr, a significant number of both major and minor interactions take place, with a final baryonic interaction at $t \sim 3.4$ Gyr (with a mass ratio of 100:1). This period of merger activity maps directly onto the time during which the ISM is significantly hotter (bottom left panel of Figure 3.3). The complete lack of major or minor baryonic mergers subsequent to this point is reflected in the absence of detectable temporal heating in stars born since $t \sim 4$ Gyr.

We have already discussed the similarity between the heating profiles of B05

and B09, where there is a clear distinction between stars born at early epochs and those born later. B05 has its LMM at a time of $t_{LMM} = 3.2$ Gyr in Figure 3.3 and has a mass ratio of 3:1 ($M_{vir}=6\times 10^{10} M_{\odot}$ and $M_{sat}=2\times 10^{10} M_{\odot}$.) It experiences only one minor 30:1 ($M_{vir}=6\times 10^{10} M_{\odot}$ and $M_{sat}=2\times 10^9 M_{\odot}$) interaction at $t\sim 6$ Gyr after the LMM, the signature of which is not readily seen in Figure 3.3 or Figure 3.3.

A03 undergoes the last major merger with mass ratio 3:1 ($M_{vir}=3.1\times 10^{10} M_{\odot}$ and $M_{sat}=1.3\times 10^{10} M_{\odot}$.) at $t\sim 6$ Gyr and it lasts for ~ 1 Gyr. The ISM is hotter during this LMM phase, as evidenced in the higher σ_w at time $t\sim 6.5$ Gyr in the middle right panel of Figure 3.3. At times earlier than $t\sim 6$ Gyr, there are many merger events as can be seen by the large velocity dispersions measured for these stars. It undergoes its last merger event at $z\sim 0.74$, i.e. $t = 7.5$ Gyr in Figures 3.3 and 3.4 and has completely merged with the disc of the main galaxy by $z\sim 0.48$, i.e $t = 9.2$ Gyr, with a mass ratio of 45:1 ($M_{vir}=9\times 10^{11} M_{\odot}$ and $M_{sat}=2\times 10^{10} M_{\odot}$). See Abadi et al. (2003b) for details of this satellite. The heating profile of stars formed more recently in A03 (i.e., those formed within the final 3 - 4 Gyr of the simulation) differs from those of the other simulations, in the sense that even these recently-formed stars within A03 experience significant heating. This can be associated to a companion satellite that survives at $z = 0$. It first appears within a radius of 15 kpc at $z = 0.33$, i.e., $t = 10.52$ Gyr, with a mass of $M_{sat}=5.8\times 10^9 M_{\odot}$.

3.3.5 The Central Concentration of the Satellites

The effect of heating that accreted satellites have on the disc is dependent on the mass distribution of the satellites, in the sense that the accretion of more massive, and more concentrated satellites, will cause a higher degree of heating (e.g. Barnes & Hernquist 1996; Velazquez & White 1999; van den Bosch et al.

2001).

Simulations produce rotation curves that rise rapidly in the inner regions with a central peak before dropping off (e.g. Mayer et al. 2008). However, observations of dwarf galaxies have shown that their rotation curves rise linearly in the central regions. Presumably, accreted satellites should have mass distributions which are similar to local galaxies. The more concentrated satellites in the simulations are related to the “angular momentum problem”, where the baryons are deficient in angular momentum and produce overly concentrated stellar bulges. This challenge for cold dark matter cosmology will be discussed in other chapters, but we note that several mechanisms have been proposed to resolve the discrepancy between theory and observation. Navarro et al. (1996); Mashchenko et al. (2008); Scannapieco et al. (2009); Governato et al. (2010) showed that resolution, which is high enough to form local star formation within an inhomogeneous ISM, will drive large scale supernova outflows and decrease the central mass concentration, producing simulated dwarfs which have a mass distribution that matches observed galaxies. The resolution required to create such dwarfs is not achieved in any simulation of a Milky Way mass galaxy in this study, or indeed in the literature.

We plot in Figure 3.5 the rotation curves of satellites in three simulations, S09, B09, and A03, chosen at redshift $z \sim 2$, each with a dynamical mass of $\sim 10^{10} M_{\odot}$. They all show peaked rotation curves indicative of an excess of central material. We have shown that the major source of disc heating in our suite of simulations is due to the interaction and accretion of satellite galaxies with the disc. The high central mass concentration of our satellites may be causing these effects to be exaggerated compared to the effect of real satellites, particularly if such satellites do indeed have “cored” rather than cuspy central density profiles and no bulge (e.g. Oh et al. 2010).

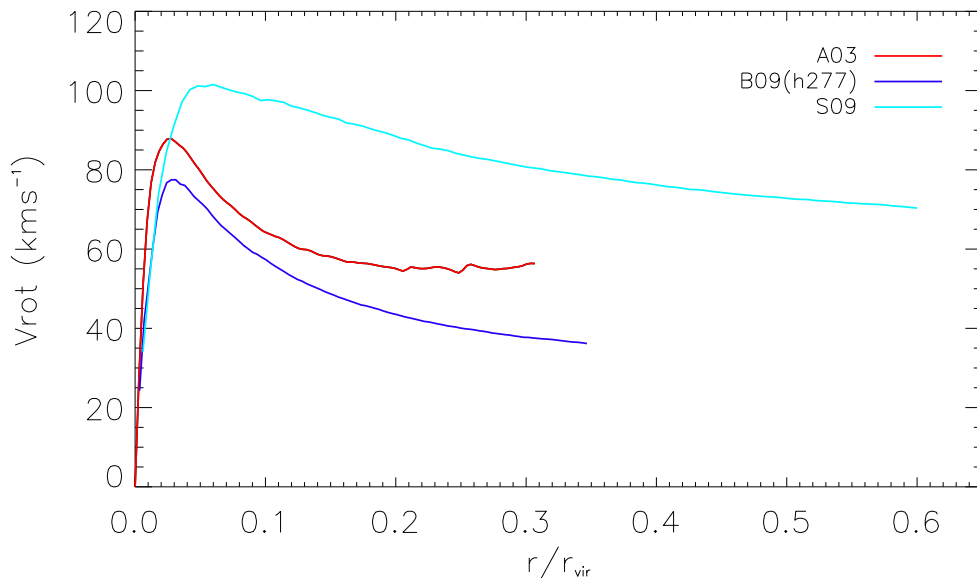


Figure 3.5: Rotation curves of satellite galaxies in three of the cosmological simulations plotted versus r/r_{vir}

This effect is perhaps the most important caveat to our work; future, increased, resolution which results in more realistic dwarfs (akin to those seen in Governato et al. (2010)) and analysed in Chapter 7 may reduce the heating rates seen in the current suite of cosmological simulations.

3.4 Conclusions

We have analysed the kinematics of disc stars in a suite of Milky Way-scale simulations which were run with different hydrodynamical cosmological codes and at different resolutions. Some were run using the Smooth Particle Hydrodynamics (SPH) approach whereas others used the Adaptive Mesh Refinement (AMR) method. This is the first study to compare cosmological disc galaxies run with these two different techniques. No differences in the analysed kinematic properties of the simulated galaxies were found to be dependent on the approach used

for the implementation of gas hydrodynamics.

We examined the velocity dispersion of our suite of simulations as a function of age for disc stars at redshift $z = 0$ and found that, even though there is a general offset between simulations and observations, in the sense that all the simulated galaxies are hotter than the Milky Way's disc, some interesting heating trends arise. Two of our simulations (B09 and B05) are in better agreement with interpretations made by Quillen & Garnett (2001), where a saturated disc is present for young stars up to $t = 6$ Gyr and discrete jumps seen in the dispersion for older disc stars. The other simulations (S09, G07, A03, and R08) seem to be in better agreement with the disc undergoing continuous heating, consistent with analysis of Holmberg et al. (2008), although the rate of heating in the simulations remains higher than that observed in nature.

We then proceeded to study the heating of these stars as a function of time; starting from the point at which the final disc was stable ($t \sim 2$ Gyr), we derived the dispersion of stars at the time of their birth and how those coeval ensembles evolved with time. We found that whereas in some simulations stars are born cold in the disc and are heated (S09, G07, A03, and H09), either numerically or due to a physical process, in other simulations (B09, B05 and R08) the stars maintain essentially the same dispersion as they possessed at birth. Further, in some simulations, stars are born with high dispersions - i.e., they are born "hot". This can be due to interactions (Brook et al. (2004)) and/or warps (Roškar et al. (2010)). Turbulence in the interstellar medium (ISM) not related to mergers could also be a cause of stars being born with large velocity dispersion. Recent observations of high redshift discs indicate that internal processes are a possible cause of the observed turbulent ISM (Genzel et al. (2008)). Bournaud et al. (2009) compared simulations formed internally in unstable gas-rich, clumpy discs with simulations of merger induced disc thickening, and found that thick discs formed

internally are a better match to observed high redshift discs. Mechanisms such as cold flows and supernova feedback are currently being discussed - in addition to mergers- as possible causes of the turbulent ISM in high redshift systems (Burkert et al. (2010); Förster Schreiber et al. (2010); Ceverino et al. (2010)).

Within the favoured cosmological paradigm of hierarchical clustering, merging and accretion of satellites onto host galaxies is fundamental. Our goal has been to examine the effects that these mergers might have upon the heating of disc stars. We find a clear relationship when looking at the heating profiles between those simulations that have late mergers and those that heat significantly. Four simulations (S09, G07, A03 and H09) have minor mergers at low redshift, and we map these interactions onto the increases seen in the velocity dispersion of their disc stars. The other three simulations (B09, B05, and R08), which have no interactions over the past ~ 7 Gyr, show little heating in the disc with time. We note that R08 is an isolated simulation which has no satellites, and hence no interactions, yet has sufficient heating due to spiral arms and migration to match observed heating rates of the Milky Way. The suite of cosmological simulations do not have the ability to resolve these secular effects, nor heating due to molecular clouds. In these simulations, it is only in the quiescent period since the last accretion events that heating is low enough to match the Milky Way's thin disc. None has a thin disc older than ~ 6 Gyr, indicating that it would be difficult to gain a thin disc as old as some estimates for the Milky Way thin disc within the current cold dark matter paradigm.

A caveat of our study is the overly concentrated mass distributions of our satellites, meaning that resolution of this persistent "old thin disc" problem may come from improved modelling of baryonic physics coupled with increased resolution, the subject of our next chapter.

Chapter 4

The Effects of Resolution and Star Formation Recipes

4.1 Introduction

It is important to determine whether numerical heating is influencing our results. A major problem in particle-based simulations is numerical two body heating. Two-body heating can have a dramatic effect on the increase in the kinetic or thermal energy of any type of particle, gas, stars or dark matter, due to the collision with another particle. In our case, it is important for the possible increase in the kinetic energy of a kinematically cold rotating stellar disc (Mayer 2004) and is, therefore, an important factor to take into consideration in our study. Such numerical effects are dependent upon resolution (Moore et al. 1996; Steinmetz & White 1997), so to partially overcome the problem of two body heating for all types of particles, gravity is decreased at small distances by means of the introduction of gravitational softening in N-body simulations.

In our sample of simulations we have a variety of resolutions; simulations with low number of particles employ larger gravitational softening lengths (ϵ),

so we quote such lengths as defining low and high resolution simulations. S09, G07, B05, and A03 have relatively low spatial resolution - with gravitational softening lengths between 400 and 600 pc - while B09 and H09 have somewhat higher resolution ($\epsilon \sim 300$ pc). The isolated disc from R08 has a much higher resolution ($\epsilon \sim 50$ pc). If the heating we see was dominated by numerical effects, one might expect a particularly large effect in the lowest resolution simulation: B05. In fact, this is the coolest of all the simulations studied. Further, we have shown that B09, B05, and R08 present similar trends in the heating of their disc stars during their quiescent period of evolution at low redshift, showing little stellar heating, despite having vastly different resolutions. Of the simulations which show significant recent merger activity, H09 is the highest resolution, yet it shows heating at low redshift in agreement with the lower resolution simulations which have similar merging histories (S09, G07, and A03). These trends appear to indicate that numerical heating is not the main driver of the inferred heating profiles.

However, the importance of the spectre of numerical heating means that one must proceed cautiously and examine the issue more quantitatively. In cosmological simulations, resolution dependence is more complicated than the case where isolated discs are used as the initial conditions. There is numerical heating, which will increase at low resolution, but on the other hand when we go to higher resolution we resolve more substructure, creating more heating. Another problem is that low resolution substructures tend to be (artificially) more concentrated (Barnes & Hernquist 1996; Velazquez & White 1999; van den Bosch et al. 2001), meaning that the heating effects of their interactions may be exaggerated. We have already discussed briefly the effects of centrally concentrated satellites in the previous chapter in § 3.3.5.

4.2 Isolated Milky Way Models

Table 4.1: Primary Galaxy Model Parameters

Parameter	Value	Definition
Disc:		
M_{disc}	$3.53 \times 10^{10} M_{\odot}$	Disc mass
R_d	2.82 kpc	Radial scale length
z_d	400 pc	Vertical scale height
R_{out}	30 kpc	Truncation radius
δR_{out}	1 kpc	Sharpness of truncation
σ_{R0}	124.4 km s^{-1}	Central radial velocity dispersion
$Q(2.5R_d)$	2.2	Toomre stability parameter
R_{\odot}	8 kpc	Solar radius
N_d	10^6	Particles in the disc
ϵ_d	50 pc	Gravitational softening
Bulge:		
ϵ_b	0.21	Energy cutoff defined by R_b
σ_b	435.7 km s^{-1}	Characteristic velocity dispersion
a_b	0.88 kpc	Scale length
α_b	0.5	Rotation parameter
M_b	$1.18 \times 10^{10} M_{\odot}$	Bulge mass
R_b	3.05 kpc	Tidal radius
N_b	5×10^5	Particles in the bulge
ϵ_b	50 pc	Gravitational softening
Halo:		
ϵ_h	0.1	Energy cutoff defined by R_h
σ_h	344.7 km s^{-1}	Characteristic velocity dispersion
r_h	8.82 kpc	Scale radius
α_h	0.5	Rotation parameter
M_h	$1 \times 10^{12} M_{\odot}$	Halo mass
R_h	244.5 kpc	Tidal radius
N_h	2×10^6	Particles in the halo
ϵ_h	100 pc	Gravitational softening

In order to separate numerical heating effects from heating due to mergers and accretions, we examine a set of isolated disc galaxies. We use the method by Widrow & Dubinski (2005), that calculates composite distribution functions (DF) for each component (disc, bulge, and halo) and produces equilibrium N-body models of disc galaxies, which are specified by a large number of parameters

fitted to a wide range of observational data of the Milky Way (see Table 4.1). This technique sets up realistic initial thin, equilibrium disc galaxies without the instabilities and transient effects that can be present in different schemes (Hernquist 1993).

The parameters employed are the same as those used in Kazantzidis et al. (2008) and were run using **GASOLINE**, using the best model fit in Widrow & Dubinski (2005), MWb with the model parameters summarised in Table 4.1. We give an overview of the parameters used for the isolated models but refer the reader to both Widrow & Dubinski (2005) and Kazantzidis et al. (2008) for full details of the parameters and initial conditions.

The Widrow & Dubinski (2005) three component models consist of an exponential stellar disc, a Hernquist model bulge (Hernquist (1990)), and an NFW dark matter profile (Navarro et al. 1997). The NFW dark matter halo density distribution function is given by the equation:

$$\rho_{NFW}(r) = \frac{\rho_h}{(r/r_h)(1+r/a_h)^2}, \quad (4.1)$$

where a_h is the scale radius of the profile, $\rho_h = \sigma_h^2/4\pi a_h^2$ is the characteristic density expressed in terms of the characteristic velocity dispersion σ_h .

The Hernquist model bulge follows the density profile:

$$\rho_H(r) = \frac{\rho_b}{(r/a_b)(1+r/a_b)^3}, \quad (4.2)$$

where a_b , $\rho_b = \sigma_b^2/2\pi a_b^2$ and σ_b are the characteristic scalelength, density and velocity dispersion respectively.

The surface density profile of the disc is assumed to be exponential in the radial direction. The vertical structure is given by a *sech*² function:

$$\rho_d(R, z) \propto \exp\left(-\frac{R}{R_d}\right) \operatorname{sech}^2\left(\frac{z}{z_d}\right), \quad (4.3)$$

where R_d and z_d represent the radial scale length and vertical scale height respectively. Note that for $z \geq z_d$, the sech^2 law mimics an exponential profile with scale height $h_z \approx z_d/2$.

The distribution functions for all three galactic components are characterised by 15 free parameters that may be tuned to fit a large range of observational data depending on what one wants to model. In our case we want to mimic the Milky Way, so we chose the best fit model parameters MWb from Widrow & Dubinski (2005). Table 4.1 list the 15 model parameters for the model MWb used as our primary galaxy.

The total mass of the final galaxy is $\sim 1 \times 10^{12} M_\odot$, similar to that of the Milky Way, with a disc gas fraction of 10%. To form a rotationally-supported disc we impart angular momentum to the gas component corresponding to a spin parameter of $\lambda=0.04$. We evolve each simulation for 1 Gyr, after allowing 0.2 Gyr for the system to relax. Kazantzidis et al. (2008) determined the appropriate settling timescale in their satellites-disc encounter simulations by monitoring the changes in the disc properties such as the velocity dispersions, surface density, and thickness, and concluded that allowing 100-200 Myr was an appropriate amount of time for the disc to settle. The disc has an initial Toomre stability parameter equal to $Q = 2.2$ (Kazantzidis et al., 2008), which means it is stable against any local non-axisymmetric instabilities.

The main differences between the isolated runs are summarised in Table 4.2. We run three simulations at different resolutions - high (ISO_HR_LT_GASOLINE), medium (ISO_MR_LT_GASOLINE), and low (ISO_LR_LT_GASOLINE) - and we employ the same star formation threshold (0.1 cm^{-3}) used in the cosmological simulations analysed in Chapter 3. The purpose of this is to see the effects resolution might have on heating stars in simulations. We then run another high resolution simulation, but employ a much higher star formation threshold (100 cm^{-3} :

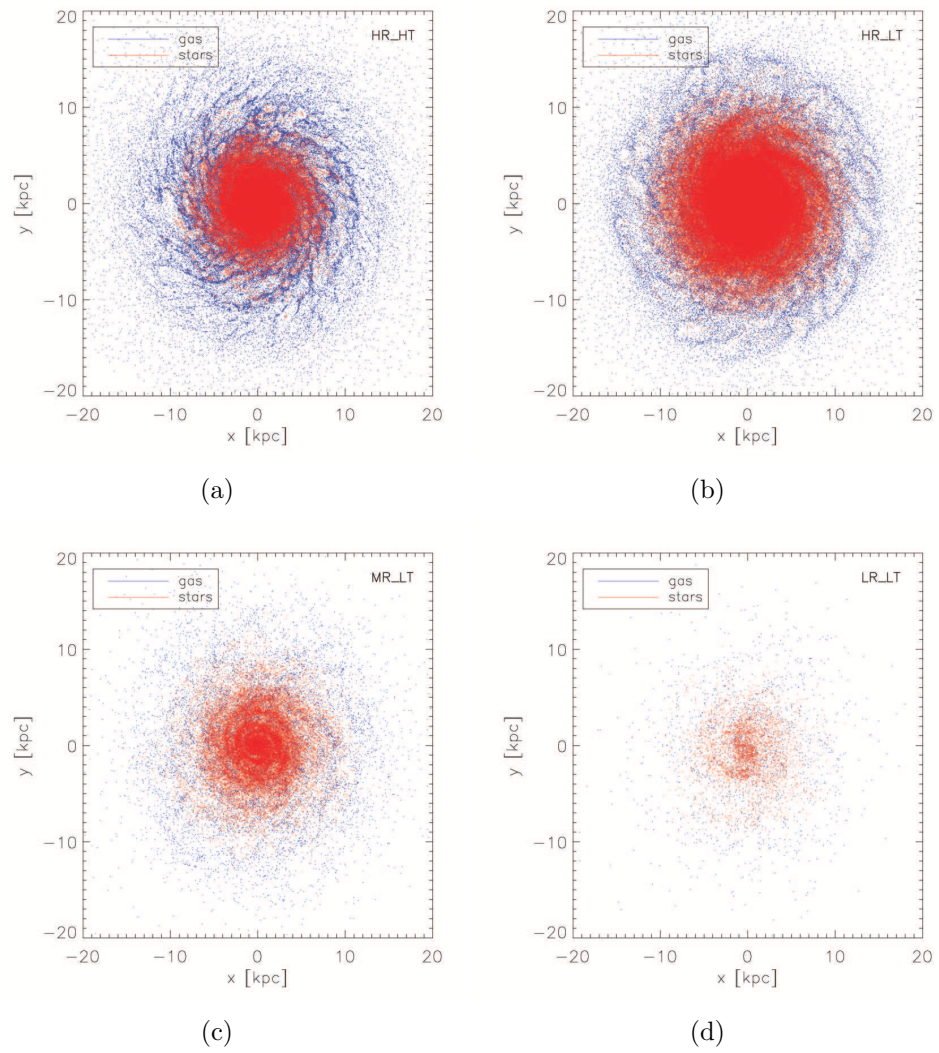


Figure 4.1:

Table 4.2: Properties of the Isolated Simulations

Name	Star Mass (M_{\odot})	Gas Mass (M_{\odot})	Dark Mass (M_{\odot})	ϵ^a (kpc)	Threshold (cm^{-3})
HR_HT	7×10^3	2×10^4	1×10^5	0.17	100
HR_LT	7×10^3	2×10^4	1×10^5	0.17	0.1
MR_LT	5×10^4	2×10^5	1×10^6	0.34	0.1
LR_LT	4×10^5	2×10^6	1×10^7	0.68	0.1

^asoftening length

ISO_HR_HT_GASOLINE), more comparable to the densities associated with star formation observed in molecular clouds.

We plot the face-on spatial distribution of stars (red) and gas (blue) for all four isolated runs in Figure 4.1

4.3 The Effects of Resolution and Density Threshold

In Figure 4.2, we plot the velocity dispersion as a function of time for stars within our set of isolated Milky Way disc galaxies. While there is a not surprising resolution-dependency in the vertical velocity dispersions of the stars at birth (ranging from ~ 16 km/s, to ~ 21 km/s, to ~ 29 km/s, for the HR, MR, and LR runs, respectively), there is little, if any, evidence for any significant heating within any of the simulations, irrespective of their different resolutions. We will return to the differences that resolution has upon the stellar velocity dispersions at birth, at the end of this section.

The differences in the velocity dispersions between the isolated runs seen in Figure 4.2 could be due to the effects of feedback in these simulations. In order to determine how important this effect may be when determining the dispersion in Figure 4.2, we compare the star formation rates (SFR) in all the isolated runs, plotted in Figure 4.3.

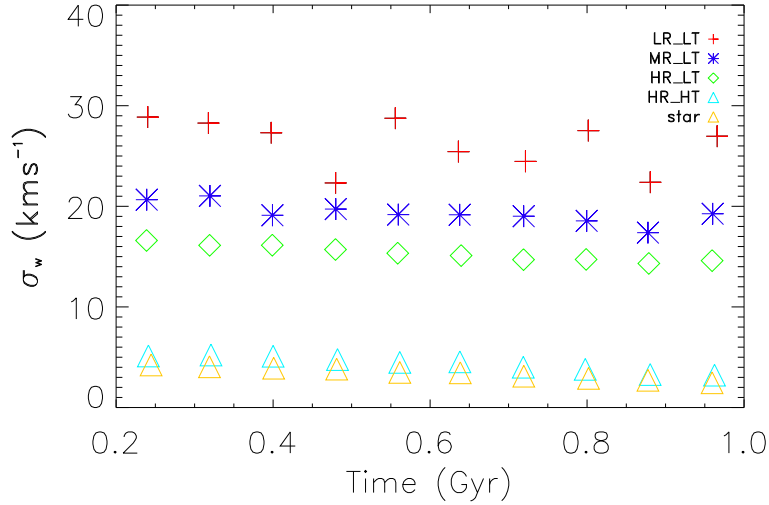


Figure 4.2: The vertical velocity dispersion as a function of time for disc stars ($4 < R_{xy} < 8$ kpc and $|z| < 1$ kpc) for four isolated Milky Way-scale simulations.

We find that the dispersion is not greatly affected by the feedback in the sense that, for example, changes in the star formation rate do not change the dispersions in Figure 4.2. As can be seen, star formation rates decrease significantly from the start of the isolated runs to the end, due to the consumption of the gas. Yet changes in the star formation rate by factors of 2 - 4 do not result in changes in the velocity dispersion, as shown in Figure 4.2. Further, comparison between the low and high threshold dispersion at times when they had equivalent SFRs, we find the same offsets as indicated in Figure 4.2. We ran an extra model to further test the effects of feedback, using the same parameters as for the high resolution and high density run only changing the feedback by increasing the star formation efficiency parameter. This is the run represented by the yellow dashed line in Figure 4.3 and named *star*. This has no effect on the dispersion.

The highest resolution isolated simulation, like the case of R08 from Chapter 3, is particularly interesting in the context of this section. Recall that the isolated simulation from Roškar et al. (2008), R08, has spatial resolution of 50 pc and is a

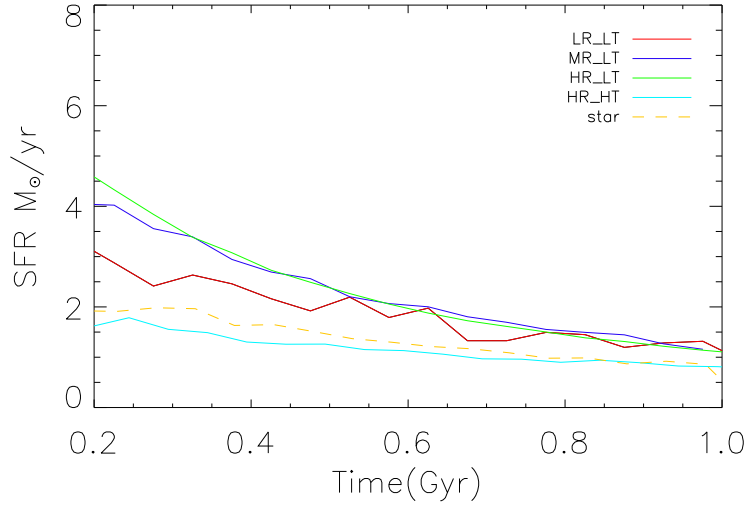


Figure 4.3: The star formation histories for our isolated Milky Way-scale simulations.

non cosmological simulation, similar to the isolated runs studied in this section, with no merger/accretion events. We found in Chapter 3 that even this simulation was kinematically “hotter” than the Milk Way disc. Both ISO_HR_GASOLINE and R08 have significantly higher resolution than the cosmological simulations analysed in Chapter 3 and are both isolated from a cosmological context. Hence, no heating from satellites occurs, yet these simulations have a vertical velocity dispersion “floor” of $\sim 15\text{--}20 \text{ km s}^{-1}$, similar to the “floor” in dispersions seen in the fully cosmological simulations during their respective quiescent periods. R08 uses the same star formation and supernova feedback physics as G07 and B09; this dispersion “floor” is tied directly to the implementation of ISM physics with in the code. Such physics is difficult to capture in cosmological simulations, as it is multi-scale, going from kpc-scale, where most of the gas is ionised, to pc-scale, where most of the gas is molecular. Cosmological simulations, like the ones analysed here, follow the formation of galaxies in a volume of at least several tens of Mpc because aspects of structure formation require that the large scale

gravitational field is properly modelled. Related to this, our inability to resolve locally collapsing high density regions means that we average star formation over large columns, using a low density threshold for star formation (0.1 cm^{-3} in the simulations analysed here). Yet star formation is observed to occur in regions where gas has cooled to significantly higher density. The low star formation threshold means that, within the simulations, gas may be forming stars in regions which remain relatively hot.

Recently, Governato et al. (2010) showed that with a spatial resolution of about ~ 100 pc, gas could be allowed to collapse to densities more representative of the average density observed in star forming giant molecular clouds. Using a star formation density threshold of 100 cm^{-3} , they successfully simulated the first bulgeless galaxy. We implement these High Threshold (HT) recipes within a high resolution isolated simulation (ISO_HR_HT_GASOLINE), and overplot the age-velocity dispersion relationship (cyan triangles) in Figure 4.2. Two striking features are immediately apparent: (i) the dispersion is much lower than for all the simulations which used a low star formation density threshold, even when using the same high resolution. The difference is far greater than the difference which was caused by resolution (see Pilkington et al. 2011, in prep, for a detailed analysis of the ISM velocity dispersion as a function of star formation threshold and resolution) (ii) very little heating occurs, even at these very low dispersions. This shows very clearly that numerical heating is not affecting our cosmological simulations. Rather, a dispersion floor is created by the inability of gas to cool sufficiently before forming stars when the star formation density threshold is set at a lower level (0.1 cm^{-3}).

Resolution-dependent differences in the dispersions of the isolated simulations are due to the differences in the degree to which the gas is able to cool before forming stars. This is supported by three pieces of information: (i) no heating

is apparent at any of the three significantly different resolutions, with the age-dispersion relation remaining flat; (ii) stars form with lower dispersion at higher resolution; (iii) even at the very low dispersion levels of the High Threshold simulation ($\sim 5 \text{ kms}^{-1}$), heating was negligible. These conclusions are supported by the fact that the temperature of the gas from which stars are born increases, as resolution decreases, with the average temperature being 7300 K, 6500 K, 5900 K and 400 K, respectively, for the LR, MR, HR, and HR_HT isolated galaxies.

4.4 Conclusions

In this chapter we focused on the effects of resolution and density threshold used for star formation in disc galaxy simulations, and the role they play in heating the stellar disc. In the previous chapter we saw how there exist an overall offset between the simulated disc galaxies and observations of the Milky Way, in the sense that the simulations are kinematically hotter than the Galaxy's disc. In order to determine which process is driving the observed offset, we ran a set of isolated Milky Way-type simulations in order to test the effects of resolution and the interstellar medium removed from any merger induced heating that may affect our results.

First of all, to study the effects of resolution, we compared isolated runs with different resolution and found that none of them show signs of heating, with a velocity dispersion remaining fairly constant with time. The interesting result from this test was that the high resolution simulation, in agreement with the findings from Chapter 3, is also hotter than the Milky Way's disc. This lead us to believe that maybe the treatment of the interstellar medium was playing a role in driving this offset. We therefore compared a simulation run with the same high resolution only this time increasing the density threshold from which stars form. The result is a simulation with a dispersion floor much lower than any of

the simulations that used a low density threshold.

We therefore conclude that the observed offset between the simulations and the Milky Way is driven in part by resolution and star formation threshold effects, although the latter is much more efficient at reducing the dispersion “floor” . We provide evidence that the dominant contributor is the low density threshold for star formation, which has been routinely implemented in simulations of Milky Way-scale galaxies, although we should point out that we only show this for non-cosmological simulations. This low density threshold means that stars are formed from unphysically high temperature gas, creating a dispersion “floor”. Indeed, our lowest resolution simulation has the least amount of kinematical heating. Future cosmological simulations with sufficient resolution to resolve the mean density of giant molecular clouds (akin to the Governato et al. (2010) dwarf galaxy simulations) will be a critical step forward in this work.

Chapter 5

The Effects of Feedback

5.1 Introduction

Cosmological simulations performed within a CDM Universe raised doubts about the ability of baryons to retain enough angular momentum to form disc dominated galaxies. The cause of the “angular momentum problem” was predicted early in CDM theory to be a consequence of the overcooling problem (White & Frenk, 1991). Without the effects of feedback, gas cools to the central regions of proto-galaxies, and rapidly forms stars prior to their merging/accretion, with angular momentum lost to dynamical friction as the central galaxy was assembled. Early simulated galaxies suffered from the overcooling problem and hence did not fall on the observed Tully-Fisher relation due to a severe shortage of angular momentum (Navarro & Steinmetz, 1997). The angular momentum problem has been shown to be at least alleviated, and perhaps solved, by improved modelling of energetic feedback from supernovae, coupled with increased resolution (Thacker & Couchman, 2000; Governato et al., 2007). One of the keys to the success of improved feedback recipes was to regulate star formation in low mass galactic building blocks. Improved feedback implementation also results in galaxies with a dominant disc, rather than a dominant stellar halo (Brook et al.,

2004). As we will highlight in this section, the disc morphology which results from the improved feedback implementations occurs largely because feedback changes the ratio of *accreted* and *in-situ* stars. Early simulations had high fractions of *accreted* stars, catastrophically lost angular momentum and had massive stellar halos.

In light of the improvement in the ability of simulations to produce realistic disc galaxies, we wish to consider the role of *in-situ* and *accreted* stars in cosmological galaxy simulations, which are dominated by a disc component. The feedback regulates star formation in the sub-halos which merge to form the larger galaxy. What therefore changes is the ratio of *accreted* versus *in-situ* stars. We shall discuss the issue of stellar feedback and show that feedback does indeed change the ratio of *accreted* to *in-situ* stars and analyse their accretion histories as well as the effects that feedback has on the global chemical properties of the galaxy.

5.2 Simulations

The first galaxy analysed in this section is taken from Stinson et al. (2010). All the simulations used in this study, were run using the SPH code `GASOLINE` described in Chapter 2. They are run in a Λ CDM cosmology with $\Omega_0 = 0.24$, $h_0 = 0.73$, $\Omega_\Lambda = 0.76$, and $\Omega_b = 0.04$. The dark matter particles have a mass resolution of $M_{dm}=2.2\times 10^6 M_\odot$. All the star particles have $M_{stars}=6.3\times 10^4 M_\odot$ and all the particles in the simulation have a gravitational softening of ~ 300 pc. The star formation and feedback recipe are described in detail in Stinson et al. (2006). The simulation analysed here is the one named g15784 from Stinson et al. (2010). It has a final virial mass of $1.4\times 10^{12} M_\odot$ and uses $E_{SN} = 0.4\times 10^{51}$ ergs as the energy released in each supernova explosion. We refer to this simulation from now on as 12m. We re-run the simulation with the same parameters and increase

the stellar feedback by a factor of 2.5, $E_{SN} = 1.0 \times 10^{51}$ ergs. We call this run 12m_hmin.

The supernovae energy values implemented in galaxy models, such as the simulations we use throughout, are fairly well constrained from light curves and spectral fitting from a number of observed supernovae. Evidence suggest that most SNeII and SNeIa modellers require between $1-2 \times 10^{51}$ ergs/SN (Nomoto & Umeda, 2002) to fit the light curves.

Observed light curves and spectra of nearby core-collapse supernovae have shown that there are extremely energetic supernovae, referred to as hypernovae (HNe), which eject more than ten times the amount of energy than in a supernova type II or Ia, i.e. $E_{HN} > 10 \times 10^{51}$ ergs (Paczynski, 1998; Nomoto et al., 2006). From empirical estimates, hypernovae rates are several orders of magnitude lower than for supernovae type II. Podsiadlowski et al. (2004) suggest that there is 1 hypernovae for every 700 supernovae. Therefore, at present, it is not clear that hypernovae are required as a central process in galaxy formation.

In the simulations used throughout the thesis we do not include energy from hypernovae but recent galactic-chemical evolution models such as those by Kobayashi et al. (2006) include stellar feedback from hypernovae, using values between $E_{HN} = 10-30 \times 10^{51}$ ergs and assume 50% hypernovae. However, from Podsiadlowski et al. (2004), the rates should be 1:700 and not 1:1 as they assume in their models. Furthermore, their models implement thermal feedback alone which has been shown to be highly inefficient at heating the surround gas (Katz et al., 1992). The simulations we analyse in this chapter use adiabatic feedback which is a much more efficient mechanism in coupling the input energy to the ISM (see Chapter 2 for details). Therefore, in the Kobayashi et al. (2006) models where high amounts of energy from hypernovae are input to the surrounding gas but thermal feedback is implemented, very little of the energy couples to the ISM. It

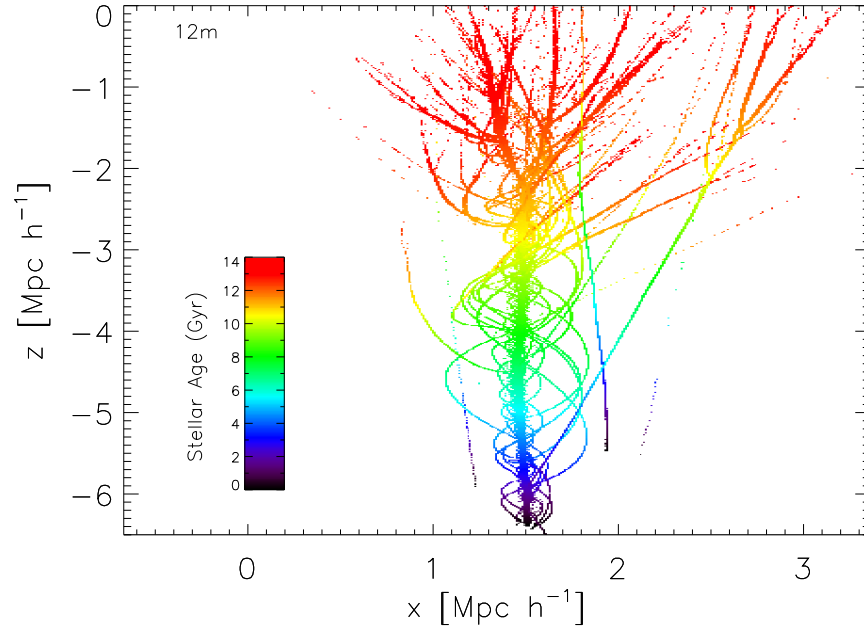
is therefore not clear that the amount of energy associated with hypernovae are actually required, because using more efficient coupling of supernovae energy, as is the case of adiabatic feedback, can produce the same results.

The coupling energy to the ISM in simulations remains the most difficult thing to constrain. What is clear is that large amounts of feedback energy are required to form disc galaxies, and hypernovae may contributor to that feedback energy. As we shall show in this chapter, increased feedback is necessary for improved disc galaxy simulations and therefore hypernovae may help somewhat, but they are not the main contributor.

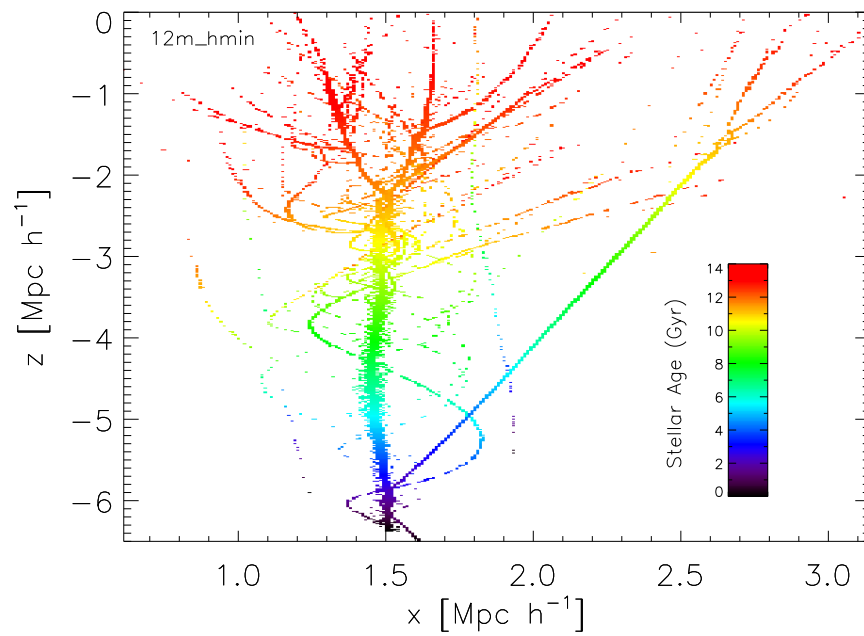
5.3 The Effects of Feedback

We plot in Figure 5.1 the positions of the stars at their time of birth in the simulation box and we colour code by stellar age for 12m, (a), and 12m_hmin, (b). The x and z axes in Figure 5.1 are in co-moving units, so what we are actually plotting is the stars in the main halo as it moves through the simulation box. We can interpret this as a stellar merger tree where the main track corresponds to the main halo of the galaxy and all the other smaller tracks are the accretion events merging into the main track as the galaxy evolves. You can see, for example, in Figure 5.1 the hierarchical structure formation process where a great number of small systems merge at early times to form larger and larger structures, as is predicted in Λ CDM cosmologies.

Both 12m and 12m_hmin have been run with the same parameters and at the same resolution, with the main difference being that 12m_hmin has a factor of 2.5 higher energy input from supernova feedback. From Figure 5.1 it is readily apparent that this results in different stellar merger trees. In Figure 5.2 we overplot both the merger trees, 12m in red and 12m_hmin in green, to highlight the differences in their star formation histories. By increasing the feedback by only



(a)



(b)

Figure 5.1: Stellar merger histories for each simulations colour coded with age.

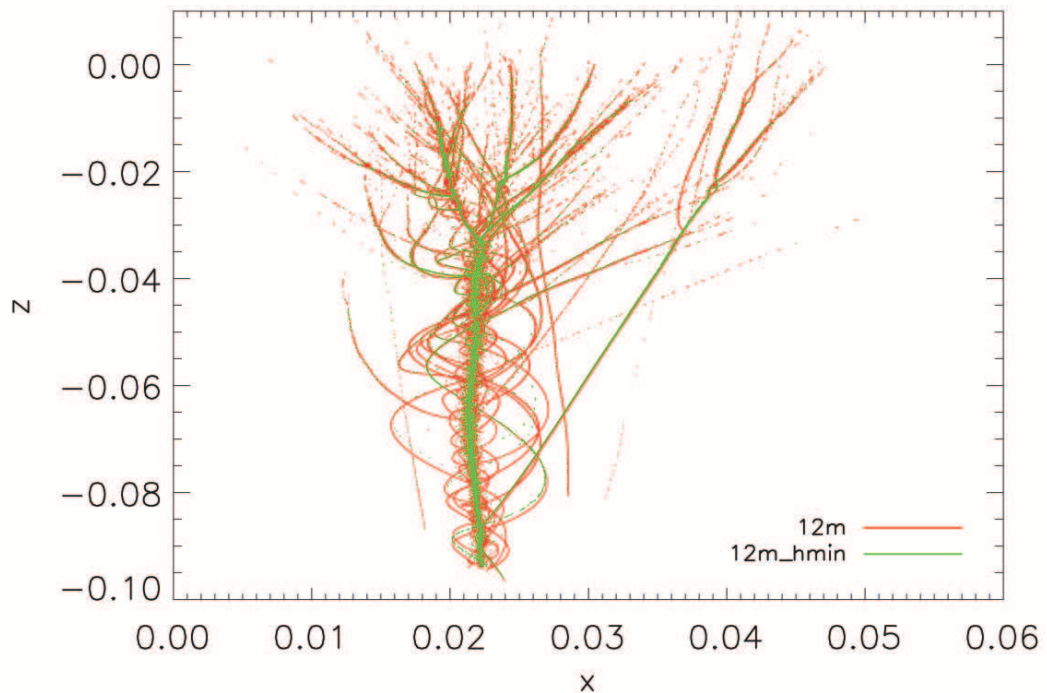


Figure 5.2: Merger histories of the stars in each simulation shown in cosmological units which are co-moving. We plot the position of the stars at birth time throughout the cosmological volume, i.e. we are seeing the galaxies fall through cosmological space.

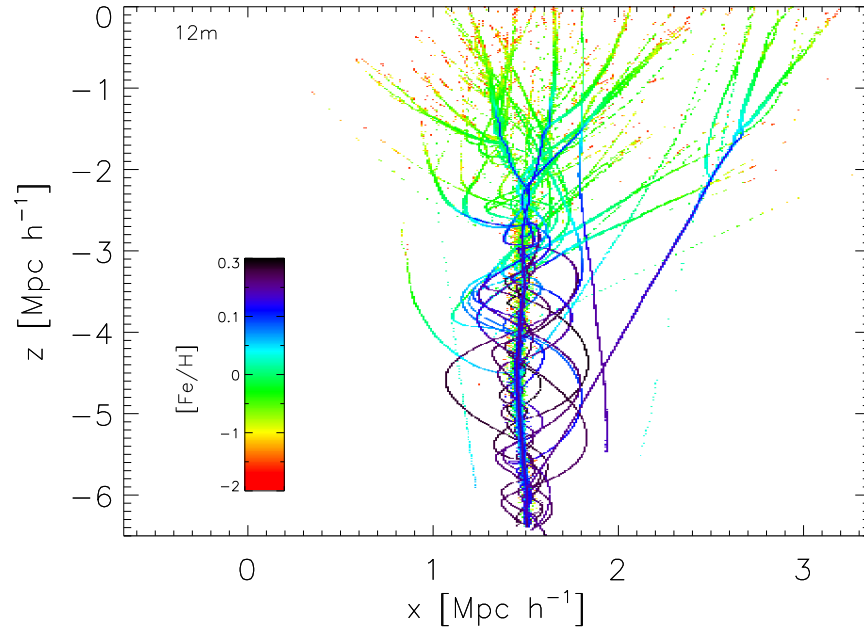
a factor of 2.5 we have reduced the stellar mass of the incoming satellites in the simulation 12m_hmin. You can see when over-plotting the two merger trees how 12m has more stellar accretion events compared to 12m_hmin and the accretion events in 12m_hmin typically have fewer stars. So, while these two galaxies have the same merger history (in dark matter), a change in feedback changes their stellar accretion histories. Stellar feedback regulates star formation in the galactic building blocks resulting in lower stellar mass in satellites being accreted in the case of 12m_hmin. We will see in this chapter that reducing the mass of the infalling satellites by increasing the stellar feedback will have implications on the chemistry of the resulting galaxy and the *accreted* and *in-situ* populations.

We plot in Figure 5.3 the stellar merger/accretion histories for 12m, (a), and

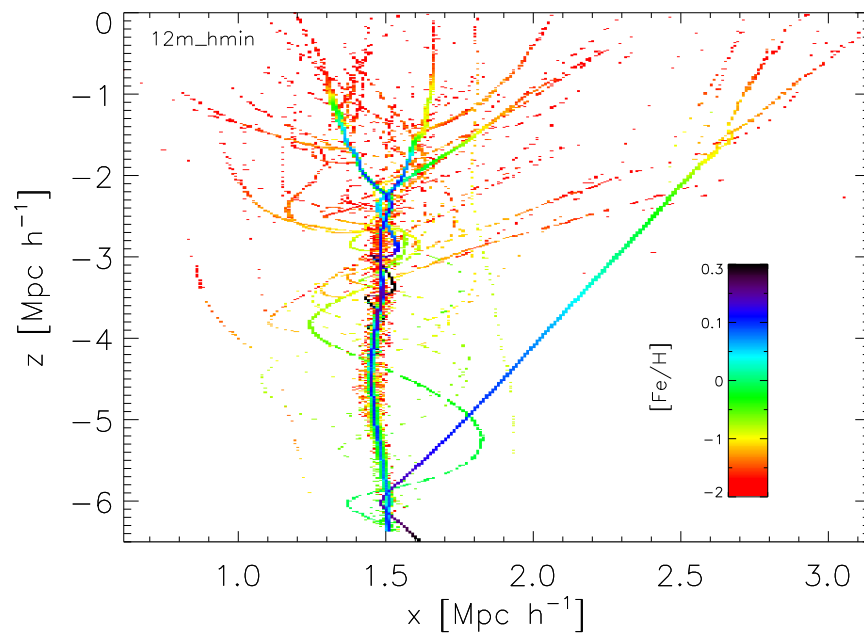
12m_hmin, (b), colour coded by the ratio of iron to hydrogen, normalised by the solar ratio on a log scale ($[\text{Fe}/\text{H}]$). The range in $[\text{Fe}/\text{H}]$ is shown in the colour bar, where black is high metallicity and red is low $[\text{Fe}/\text{H}]$. For the 12m simulation, shown in Figure 5.3 (a), you can see that old stars, see Figure 5.1 (a), are metal poor and as the galaxy evolves the new stars have increasingly higher values of $[\text{Fe}/\text{H}]$. This is a natural consequence of chemical evolution theory. As stars evolve and end their lives, they eject new elements into the interstellar medium (ISM) via stellar winds and supernova explosions. Since the returned material is enriched in metals (elements heavier than helium that have been synthesised in the stars) the next generation of stars formed from this gas will have higher metallicity.

As we mentioned in the introduction of this chapter, a known and persisting problem in cosmological disc simulations is the overcooling problem, which results in the gas collapsing to the centre of proto-galaxies, such as the ones merging in this simulation, prior to the merging process and forming too many stars. As a result of this rapid star formation these satellites or proto-galaxies attain metallicities which are much higher than low mass galaxies in the local Universe, and also compared with the accreted satellites which helped form the Milky Way's halo. In Figure 5.3 (a) you can see that the accreted stars have high metallicities as they spiral down into the main galaxy, and also that the satellites which survive have high metallicities.

If we look at the same stellar merger history but for 12m_hmin (Figure 5.3 (b)), the metallicity of the satellites are significantly lower. By increasing the stellar feedback in this simulation you are diminishing the over cooling problem by not allowing the gas to cool and rapidly form stars. High feedback can also eject metals and, furthermore, extended timescales of star formation when feedback is included can allow low metallicity gas to be accreted. The lower number of



(a)



(b)

Figure 5.3: Stellar merger histories for each simulations colour coded with Fe/H .

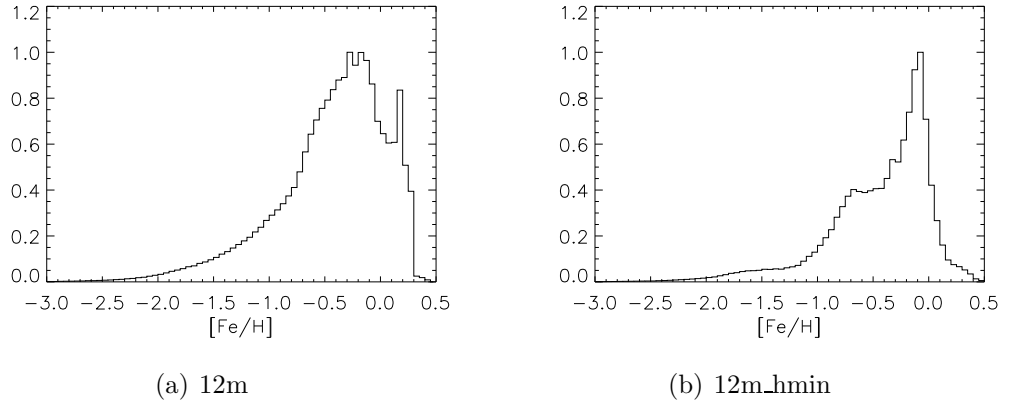


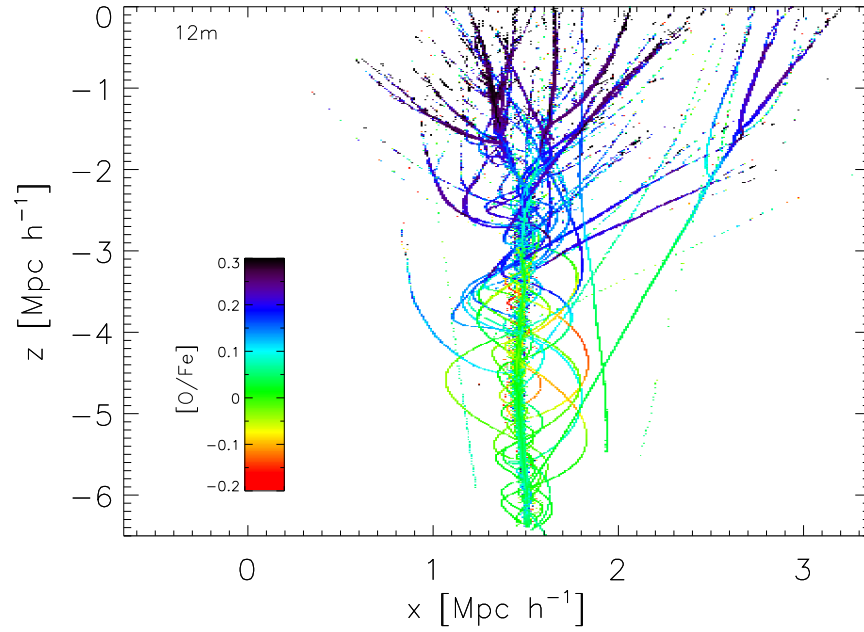
Figure 5.4: The $[\text{Fe}/\text{H}]$ distribution functions normalised to unity for 12m, (a), and 12m_hmin, (b).

stars in the proto-galaxies in the high feedback case therefore also have lower metallicity.

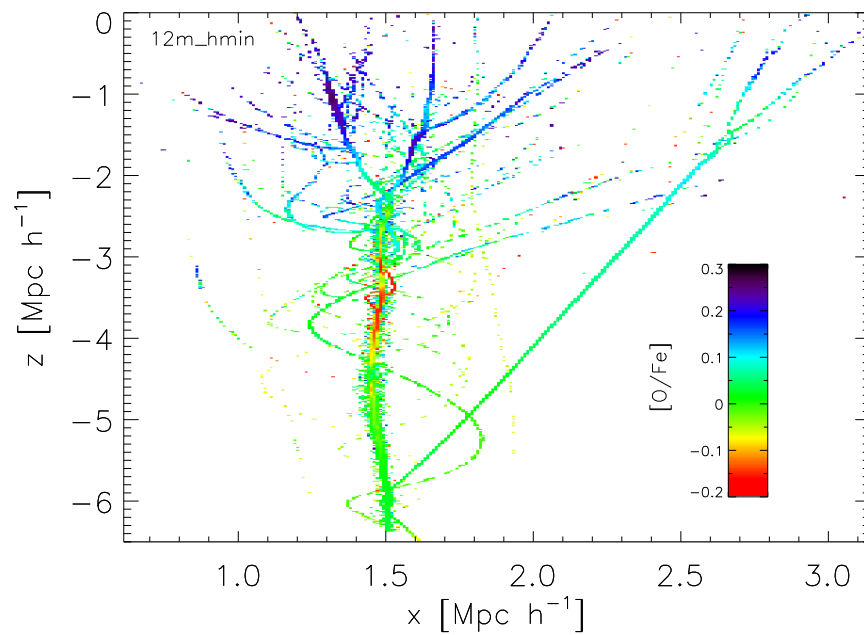
We plot the $[\text{Fe}/\text{H}]$ metallicity distribution functions, (MDF), for 12m, (a), and 12m_hmin, (b), in Figure 5.4. We normalise the distributions to one so that the shapes can be compared. The high metallicity peak in 12m’s MDF at ~ 0.2 dex is no longer there in 12m_hmin. The 12m MDF peaks at around -0.2 dex and then declines to about -2.0 dex, with a wider distribution than in 12m_hmin. 12m_hmin, on the other hand shows two peaks in its MDF, one at -0.1 dex and a second peak at lower metallicity, -0.6 dex. 12m still has more stars at the metal poor end between -0.5 and -1.0 dex than 12m_hmin.

As we mentioned in Chapter 1, an abundances ratio that holds clues into the formation history of a galaxy is its $[\alpha/\text{Fe}]$, in our case $[\text{O}/\text{Fe}]$ ratio. Alpha elements and Fe are produced in different supernova explosions and at different timescales, therefore studying their ratio will tell us about the formation and the timescales of different components and populations.

In Figure 5.5 we plot the same stellar merger tree only this time we colour code the stars by their $[\text{O}/\text{Fe}]$ ratio. The range is shown in the colour bar, where



(a)



(b)

Figure 5.5: Stellar merger histories for each simulations colour coded with O/Fe.

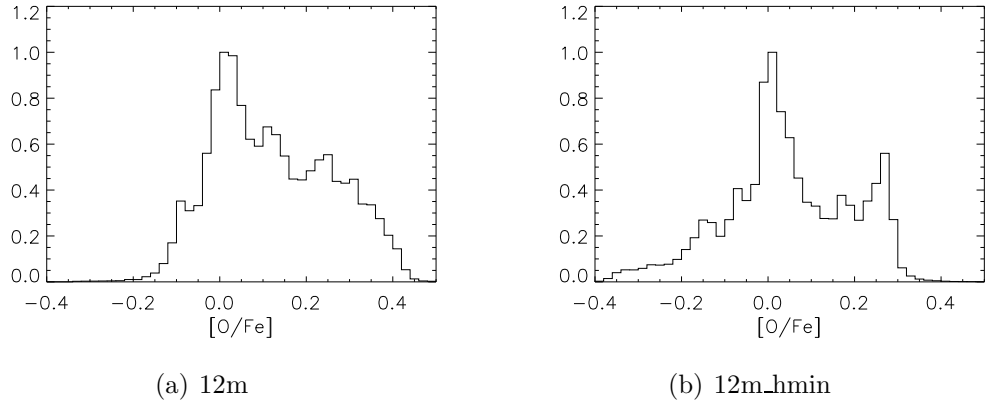


Figure 5.6: The $[\text{O}/\text{Fe}]$ distribution function normalised to unity for 12m, (a), and 12m_hmin, (b).

high $[\text{O}/\text{Fe}]$ ratios are black and low $[\text{O}/\text{Fe}]$ ratios are red. As one might expect, the older stars at the top of the merger tree have high $[\text{O}/\text{Fe}]$ ratios due to the pollution of the interstellar medium by SNeII. Whereas, as the galaxy evolves the stars that are born later on have lower and lower $[\text{O}/\text{Fe}]$ ratios as SNeIa begin to pollute the interstellar medium with Fe. If we compare 12m and 12m_hmin in Figure 5.5, older stars in 12m have higher $[\text{O}/\text{Fe}]$ ratios than those in 12m_hmin and 12m has high $[\text{O}/\text{Fe}]$ ratios for longer. Not only that, the accreted satellites also have higher $[\text{O}/\text{Fe}]$ ratios than the satellites in 12m_hmin. This is related to the different star formation timescales of 12m and 12m_hmin, with rapid early star formation in 12m resulting in the enrichment of α -elements by SNeII.

In Figure 5.6 we plot the $[\text{O}/\text{Fe}]$ distribution function for 12m, (a), and 12m_hmin, (b). The range of $[\text{O}/\text{Fe}]$ in 12m is between -0.2 to 0.4 dex, peaking at \sim solar. When compared with 12m_hmin, 12m has more α -enhanced stars between 0.2 and 0.4 dex than 12m_hmin, and less stars at -0.2 to -0.4 dex.

We can see that increased supernova feedback has affected the chemistry of the final galaxy. We now probe further by examining the effects of feedback on the chemistry of stars born in the central galaxy as well as those born in satellites

and subsequently accreted to the main halo.

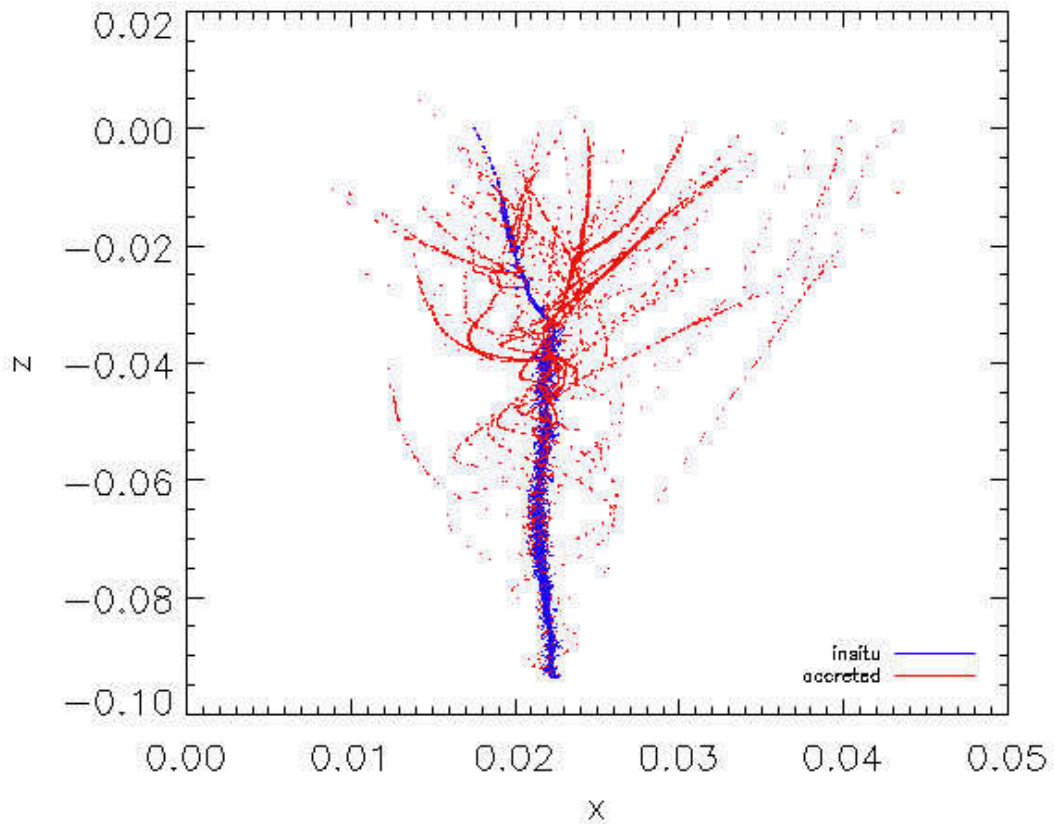


Figure 5.7: The *in-situ* stars in blue and the *accreted* stars in red for 12m_hmin using the stellar merger tree to determine these two populations. The x and y axis are in cosmological units which are co-moving.

5.4 The Effects of Feedback in *Accreted* and *In-situ* Populations

For these galaxy simulations it is possible to determine which stars formed *in-situ* and which ones were *accreted*. We do this in a very straight forward manner and we believe it is the most accurate way of determining these two populations. From Figure 5.1, where we plotted the positions of the stars within the cosmological box at their time of birth, we are able to determine which track corresponds to the main halo. All stars that trace this main track are those which are born *in-situ*. Stars born in all other tracks are those which are *accreted*. We demonstrate

Table 5.1: Mass of *accreted* versus *in-situ*

Name	M_{vir} (M_{\odot})	$M_{stellar}$ (M_{\odot})	M_{insitu} (M_{\odot})	$M_{accreted}$ (M_{\odot})
12m	1.4×10^{12}	1.3×10^{11}	8.8×10^{10}	4.3×10^{10}
12m_hmin	1.4×10^{12}	9×10^{10}	6.9×10^{10}	2×10^{10}

how we select these two populations in Figure 5.7, where the main halo with stars born *in-situ* are in blue and all the accreted stars are in red.

In Table 5.1 we show the resulting stellar masses of the *accreted* and *in-situ* populations in the final galaxy of 12m and 12m_hmin. The mass ratios of *accreted* to *in-situ* stars has gone from 0.48 in 12m to 0.29 in 12m_hmin demonstrating that feedback has changed the ratio of *accreted* to *in-situ* stars in the simulations.

In Figure 5.8 we plot the metallicity distribution functions (MDF) of the *accreted* and *in-situ* stars in 12m, (a), and 12m_hmin, (b). The MDFs are normalised so that the peak of each distribution is equal to one so that the shapes of their distributions can be readily compared. Recall that the total mass of each population is given in Table 5.1. The MDFs of the two populations in 12m are very similar, ranging between $0.3 \leq [\text{Fe}/\text{H}] \leq -1.5$, both peaking at ~ -0.1 dex. This is due to the high metallicity satellites that are accreted in this simulation as can be seen from Figure 5.3 (a). In 12m_hmin, on the contrary, we already see a separation in the MDF's for the *accreted* and *in-situ* stars. As a result of the higher implemented feedback, the accreted populations have lower metallicities, with a range $0.3 \leq [\text{Fe}/\text{H}] \leq -2.5$ dex and peaking at -0.4 dex. This demonstrates that the supernova feedback has more effect in the lower mass satellites than in the central galaxy.

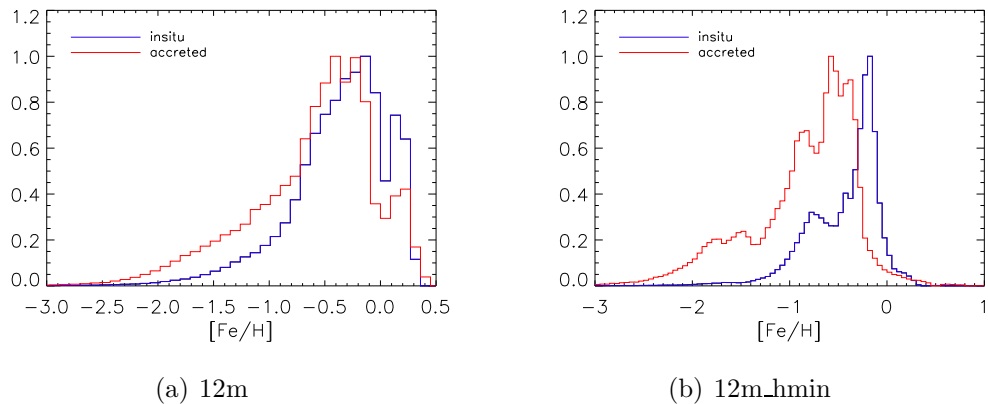


Figure 5.8: The metallicity, $[\text{Fe}/\text{H}]$, distribution functions, normalised to unity, of all stars for 12m and 12m_hmin simulations showing both the *in-situ* and *accreted* stellar populations.

5.5 Conclusions

This chapter has shown how supernova feedback affects galaxies. We have shown that the increase of supernova feedback in a simulation regulates star formation, especially at early times, resulting in the formation of less stars. Further, the regulation of star formation is more effective in the smaller building blocks. This results in a galaxy which has less accreted stars. Feedback is therefore responsible in altering the ratio of *accreted* to *in-situ* stars in a galaxy.

A consequence of supernova feedback is the effect it has on the chemistry of the galaxy and its building blocks. As a result of supernova feedback regulating star formation, the metallicity of accreted stars become lower, meaning that the galaxy has less accreted stars and they are of lower metallicity, and hence the stellar halo is less massive and has lower metallicity, more in line with observed disc galaxies. The stars accreted at early times retain a relatively high ratio of α to iron elements, regardless of supernova feedback, but the higher feedback run evolves towards lower α to iron ratios, meaning that the surviving satellites have lower α abundance ratios than those which were accreted at early times. This can

explain the observations of Venn et al. (2004), which show that the Milky Way halo stars have higher α to iron ratios than the local dwarf populations. Similar conclusions were found using semi-analytic methods in Robertson et al. (2005)

We have seen that feedback is more effective in regulating the star formation and lowering the abundances in satellite galaxies. This motivates us to better probe the different manner that our implementations of the baryonic physics of gas cooling, star formation and feedback are affected by the mass of the host halo. We would like to make more direct comparisons of simulated galaxies which differ only in their mass. In the next chapter we will compare simulations which have the same merger history and the same degree of isolation from nearby structures, and differ only in their mass.

Chapter 6

The Effects of Mass

6.1 Introduction

In classic theory of the formation of disc galaxies, tidal torques from surrounding large scale structures provides angular momentum for gas, which cools into a central galaxy, retaining its angular momentum to form a disc (Fall & Efstathiou, 1980). Yet, in the hierarchical build up of galaxies within the concordant cold dark matter cosmological paradigm, mergers result in the accretion of stars born in sub-dominant proto-galaxies (White & Rees 1978; Brooks et al. 2009). Such sub-halos also bring in gas with them, although most gas is accreted smoothly (Kereš et al., 2005). Merger events have tended to cloud the classical theories of disc formation. Indeed, mergers have long been associated with the formation of elliptical galaxies (Toomre 1977). Yet merger histories are essentially scale free in the dark matter, meaning that low mass halos in which discs reside have similar histories as high mass halos which predominantly host elliptical galaxies. Unless significant revision of cold dark matter theory is invoked, then baryonic processes must explain the mass-morphology relation, and the related tendency for low mass galaxies to preferentially lie on the blue sequence whilst high mass galaxies lie on the red sequence (see Figure 6.1).

In the previous Chapter we examined the effect that feedback has on the stellar merger tree of galaxies as well as its effect on the chemistry. The more effective regulation of star formation in lower mass systems motivated us to more closely study the effects of the baryonic physics on different mass scales. In order to isolate the effects of mass from the different effects of specific merger histories, we run simulations on galaxies at three different mass scales, using the same underlying dark matter halo. This means that the merger histories of the three simulations are identical, and hence any differences will be due to the way that star formation and feedback operate at different mass scales. We will look at the kinematic and chemical properties of the galaxies, and examine how the role of stellar accretion becomes more important in more massive galaxies. Note that we do not include AGN feedback in these simulations: as we examine mass ranges up to L_* (total luminosity of the Milky Way, $L_*=3\times 10^{10} L_\odot$), AGN feedback is believed to be not important (Magorrian et al. 1998; Silk 2011).

6.2 Simulations

Our most massive simulation used in this chapter is the same as the one in the previous Chapter 5, 12m. It is run in the fiducial 68 Mpc box, with particle masses of $M_{dm}=2.2\times 10^6 M_\odot$, $M_{stars}=6.3\times 10^4 M_\odot$, and $M_{gas}=3.8\times 10^4 M_\odot$ for dark matter, stars, and gas respectively. All the particles have a gravitational softening of ~ 300 pc. The final virial mass is $1.4\times 10^{12} M_\odot$ and it undergoes its last major merger (mass ratio 2:1) at $t_{LMM} = 1.95$ Gyr.

We then re-scale down to a 34 Mpc box, giving our intermediate mass galaxy with $1/8^{th}$ of the mass and $1/2$ the length scale, making a halo mass of $1.7\times 10^{11} M_\odot$. We call this medium mass simulation 11m. We then scale down again to a 17 Mpc box for our smallest mass halo, which now has $1/64^{th}$ the mass of the most massive halo, and $1/4$ its length scale, with final virial halo mass of $2.2\times 10^{10} M_\odot$.

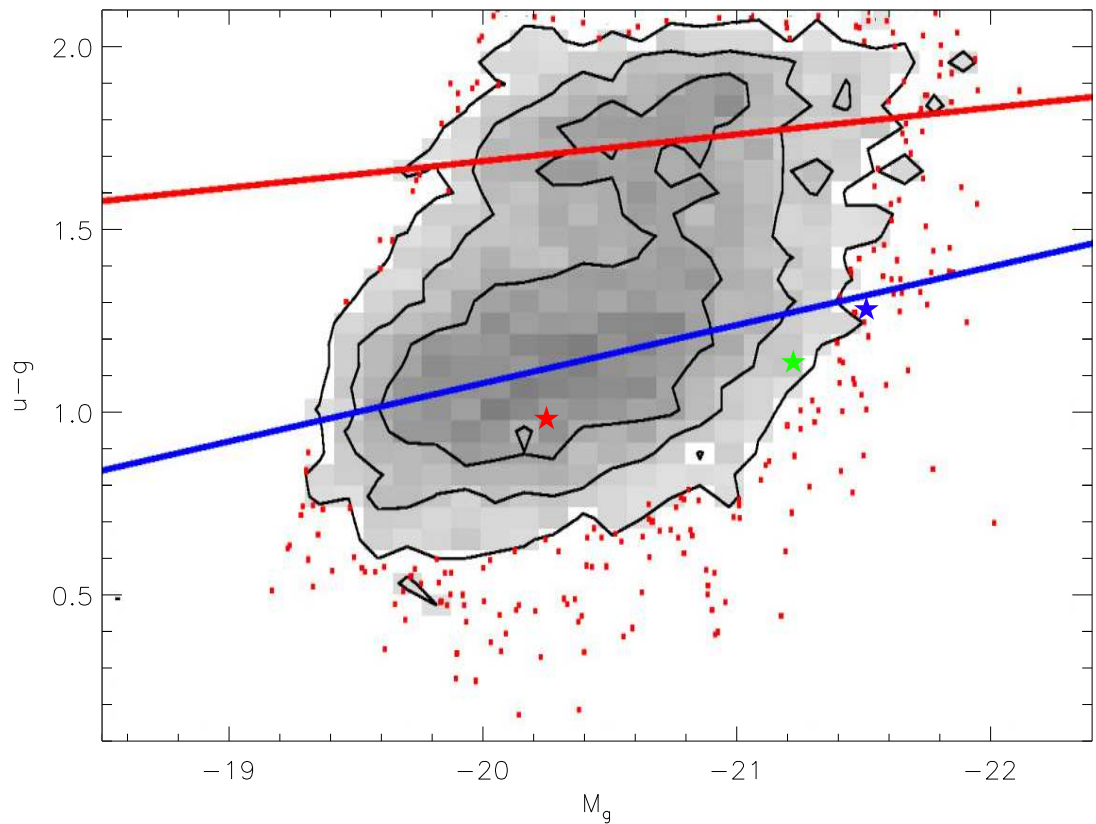


Figure 6.1: The SDSS-predicted distribution of colour and absolute magnitude. The upper solid red line corresponds to the locus of the red sequence as predicted by SDSS. The lower blue solid line is the locus of the blue sequence in the SDSS prediction. We overplot the different mass simulations as stars. The blue star is 12m, the green is 12m_hmin, and the red is 11m.

This corresponds to our lowest mass galaxy for this study and we refer to it as 10m. This means that we are able to use the same input physics over three mass scales on simulations which have the exact same merger history. The differences in their properties will be due to the differences in how the hydrodynamics, star formation, and feedback recipes operate depending on the mass of the host halo.

In Figure 6.1 we show the $u-g$ colour versus the absolute g magnitude, M_g , (CMD) of $\sim 3 \times 10^5$ galaxies from the SDSS data as the shaded region. We overplot the simulated galaxies as a blue star, 12m, green star, 12m_hmin (from Chapter

5), and red star, 11m. The CMD is known to be bimodal with two well-known features. The red sequence, which is highlighted in Figure 6.1 by the top red line, and the blue cloud, represented by the bottom blue line. The red sequence is fairly narrow and extends up to very bright galaxies. The blue sequence, or cloud, is broader. This simply reflects that galaxies come in two different classes: early-type galaxies containing relatively old red stellar populations, and late-type galaxies with on-going star formation that are blue. This colour-morphology relation is not always this straightforward, as disc galaxies may appear red due to dust extinction or elliptical galaxies might be bluer due to small amounts of recent star formation. Two trends are noteworthy in the observed CMD. The bright end of the CMD is dominated by the red sequence, whereas at the faint end the majority of galaxies are blue, late-type galaxies. The second trend is that, within each sequence brighter galaxies are redder. This reflects that brighter galaxies are both older (referred to as “down-sizing”) and more metal rich. There is a third feature in the CMD known as the green valley, which lies between the red sequence and the blue cloud. It is believed to be a transition region between the two morphological types of galaxies. A lot less galaxies are observed to lie in the green valley. It is natural to identify the red sequence with ellipticals and lenticulars (E,S0) and the blue sequence with spirals and irregulars.

The first thing we can observe from Figure 6.1 is that 12m, 12m_hmin, and 11m lie in observationally populated regions of the CMD. All three sit nicely on the blue sequence mainly populated by spiral galaxies. 10m is a dwarf irregular galaxy, and it is too dim to sit on the SDSS CMD and is therefore not shown in this figure. The difference in the two 12m galaxies in Figure 6.1 can be traced back to feedback effects. The simulated galaxy 12m, which we analysed in Chapter 5, lies on the red end of the blue sequence. Due to increased feedback in 12m_hmin, the galaxy has a lower magnitude and the galaxy is bluer. This is related to the

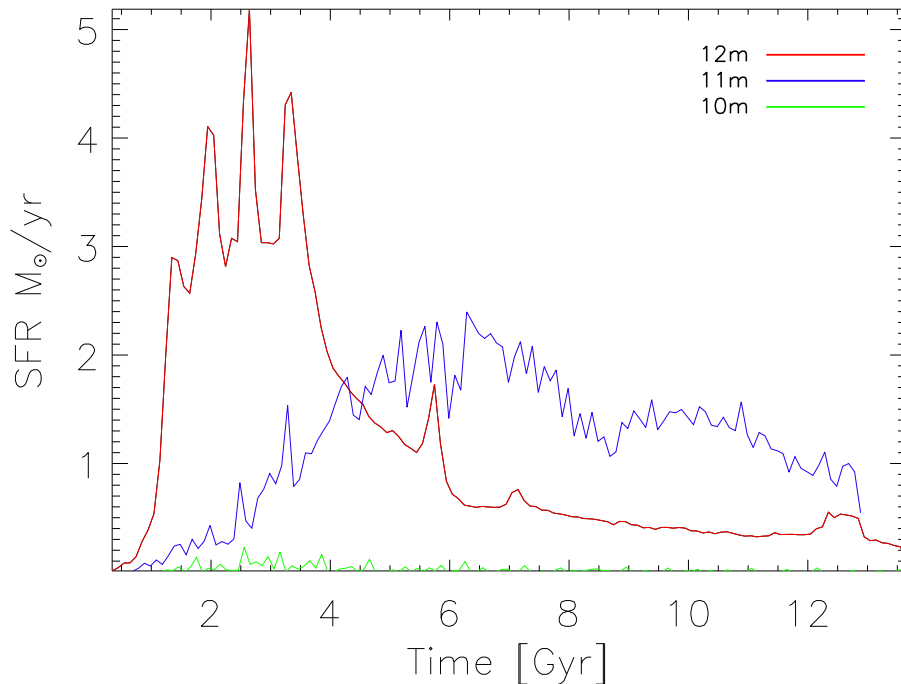


Figure 6.2: The star formation rate of the different mass galaxies. The high mass simulation, 12m, in red, the medium mass, 11m, in blue, and the low mass galaxy, 10, in green.

overcooling problem in 12m, where excess gas is driven to the centre of the galaxy where it cools rapidly and forms stars due to the high gas density. As we scale down the simulation, the lower mass galaxy, 11m, has lower magnitude and is bluer.

We plot the star formation rates of the three simulations in Figure 6.2. 12m, shown in red, has early star formation peaking at $t = 3$ Gyr. It rapidly declines at $t = 4$ Gyr with a later peak at ~ 6 Gyr. These peaks are related to mergers, as can be seen from the merger trees in, e.g. Fig 6.4 (a). Hereafter it has a fairly quiescent star formation activity with an average star formation rate of $\sim 0.5 M_{\odot}/\text{yr}$. 11m has a delayed star formation at early times in comparison to 12m. It peaks later at $t = 6$ Gyr and has prolonged star formation at later times,

with an average star formation rate of $1.5 M_{\odot}/\text{yr}$ in the last 4 Gyr. The delay in the star formation at early times in 11m shows that we have reproduced galaxy downsizing (Cowie et al., 1996), whereby massive galaxies form at higher redshift and as the Universe ages star formation in larger galaxies is reduced, whilst late star formation continues in smaller galaxies. The smallest of the simulations, 10m, has very little star formation. It is a dwarf irregular that is mainly comprised of gas.

6.3 The Effects of Mass

We plot in Figure 6.3 the stellar merger trees for the three different mass simulations, 12m (red), 11m (blue), and 10m (green). It is readily apparent that by scaling down the galaxy and hence decreasing its mass, less stars form in the building blocks at early times and therefore less satellites are accreted to the main halo of the galaxy. In fact, the simulation that has been scaled down the most, 10m, does not have any accreted stars and the resultant galaxy forms entirely of stars born *in-situ*, traced by the main track of the halo (see green track in Figure 6.3). The 11m simulation (see blue track in Figure 6.3) has significantly fewer tracks merging into the main halo, and hence few accreted stars. The lack of stars in the lowest mass progenitors is related to the UV background radiation. The gas photo-ionised by such radiation is unable to cool in halos less massive than $\sim 10^9 M_{\odot}$ (Bullock et al., 2001; Benson et al., 2002). Therefore, by rescaling down, even though the ratio of the mass of mergers stays the same in low and high mass systems, the absolute value of the halo mass of progenitors is important and a lower bound exists below which satellites do not have stars.

In Figure 6.4 we plot the stellar accretion history for each simulation individually colour coded with time. The 12m simulation, which was discussed in

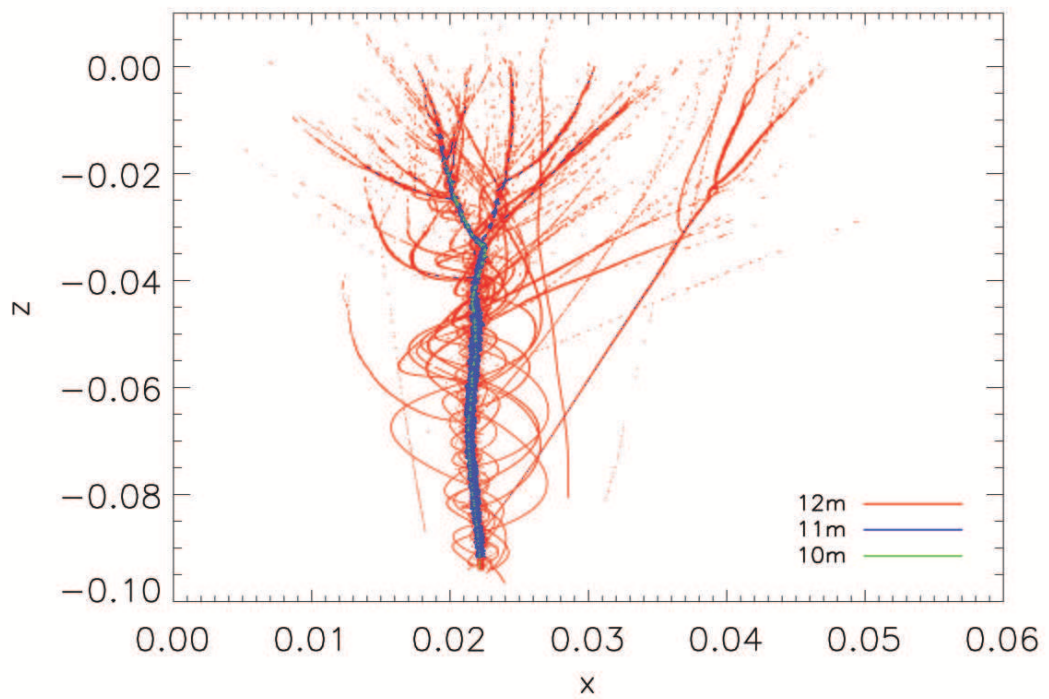
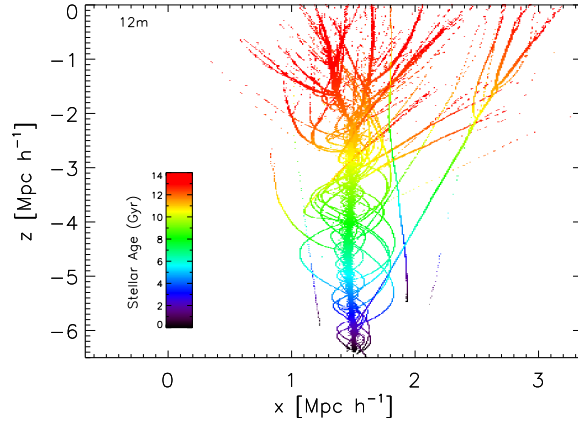
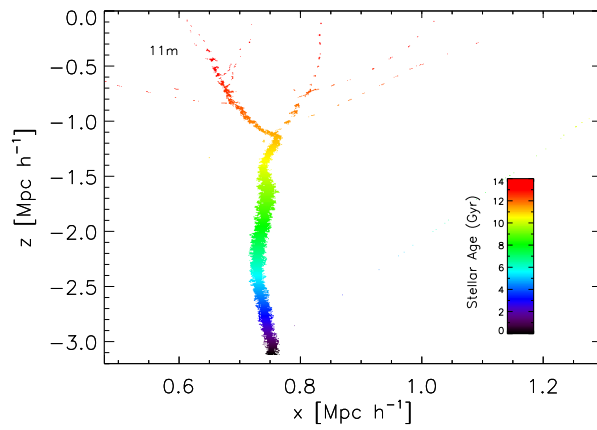


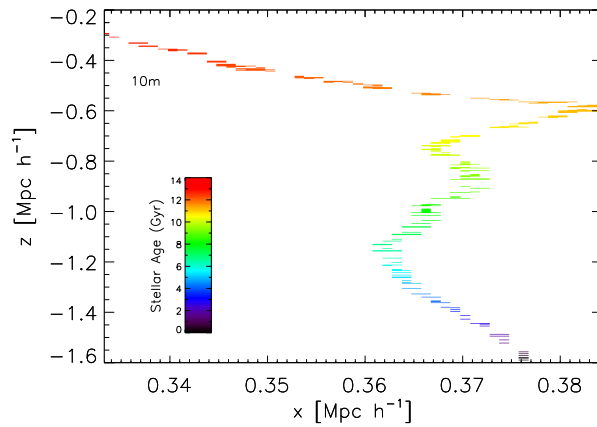
Figure 6.3: Merger histories of the stars in the three simulations shown in cosmological units which are co-moving. We plot the position of the stars at birth time throughout the cosmological volume for all three different mass simulations, 12m in red, 11m in blue, and 10m in green.



(a) 12m



(b) 11m



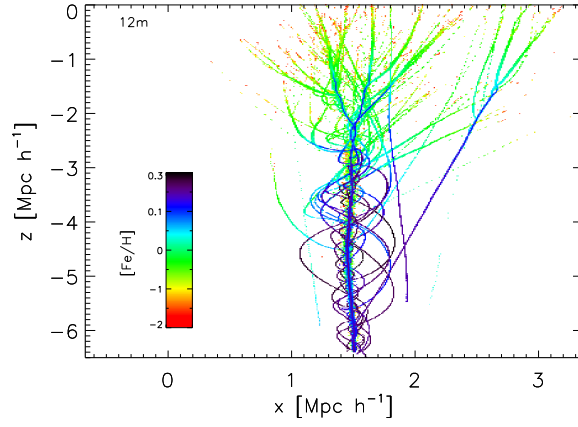
(c) 10m

Figure 6.4: Stellar merger histories for each simulations colour coded with age.

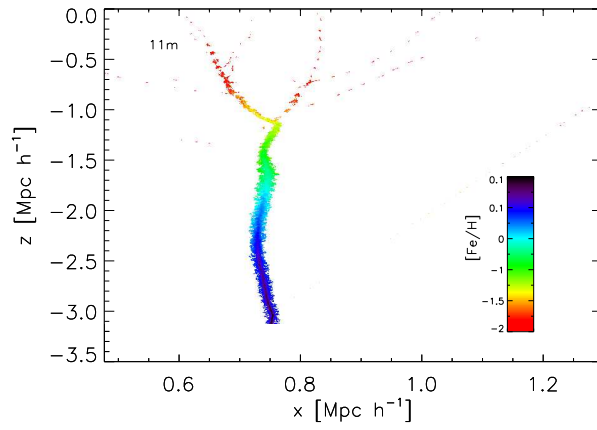
comparison with 12m_hmin in the previous chapter, shows early epochs of accretion at the top of the merger tree, with less and less accretion events happening as the galaxy evolves. We plot the 11m simulation, which has been scaled down by $1/8^{th}$ in mass, in Figure 6.4 (b) and we note significantly less accretion events. The last major merger is visible at ~ 9 Gyr ago, with only a small merger event that follows, then a long period where no stellar mergers occur. Note that dark matter only mergers are occurring during this late period. We plot the stellar merger tree for 10m, which has been scaled down by $1/64^{th}$ in mass from 12m, in Figure 6.4 (c). The result is a galaxy that is comprised entirely of stars born *in-situ* showing no accretion events. The dark matter halos that merge in the lowest mass simulation are too low in mass to host stars, due to the effects of photo-ionisation from the back-ground radiation. By scaling down the simulation we are preventing the formation of stars in the building blocks. We have seen a dramatic effect on the ratio of *accreted* to *in-situ* stars as we move to the lower mass galaxies.

In the previous chapter we showed that by increasing the feedback the star formation in building blocks was regulated more efficiently and this had an effect on the chemistry of low mass satellites and hence also on the chemistry of the final galaxy, as the accreted satellites had lower metallicity. To determine the effects of mass in the chemistry of these simulations, we plot in Figure 6.5 the stellar merger histories of our three different mass galaxies colour coded by $[Fe/H]$. The $[Fe/H]$ ratio range for each simulation is shown in the colour bar in each panel. Note that the ranges are different and therefore one must be careful when comparing. As we scale down the galaxy, the $[Fe/H]$ ratio decreases overall in the simulations (see the difference in range at high $[Fe/H]$ ratio in each panel).

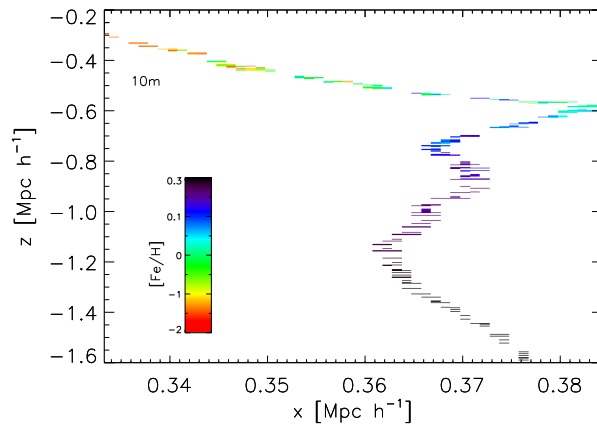
The observed trend that metallicity decreases with decreasing galaxy mass has been well established in the literature (Tremonti et al., 2004; Lee et al., 2006).



(a) 12m

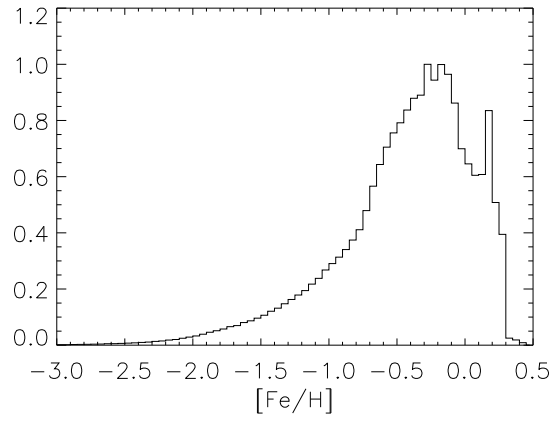


(b) 11m

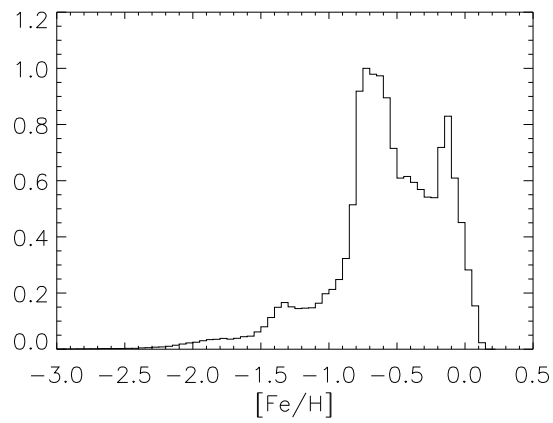


(c) 10m

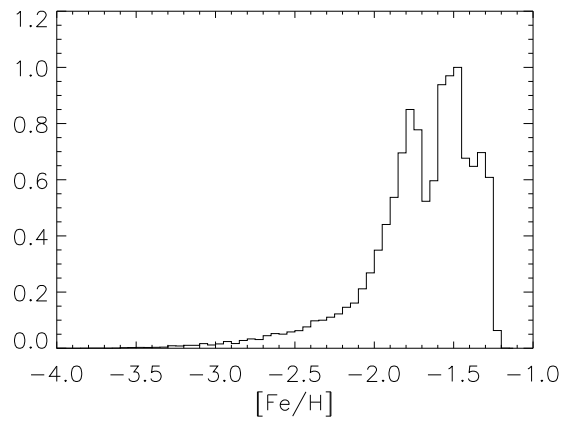
Figure 6.5: Stellar merger histories for each simulation colour coded by $[\text{Fe}/\text{H}]$.



(a) 12m



(b) 11m

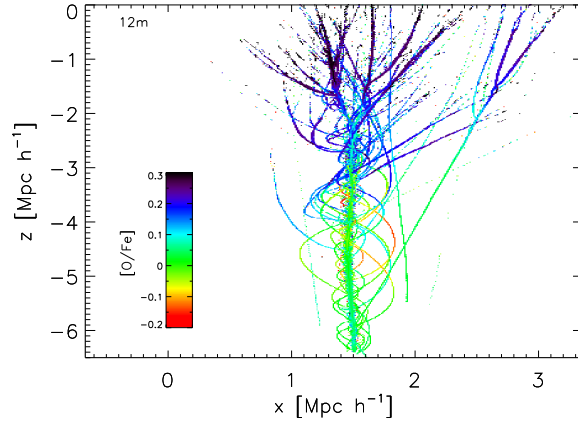


(c) 10m

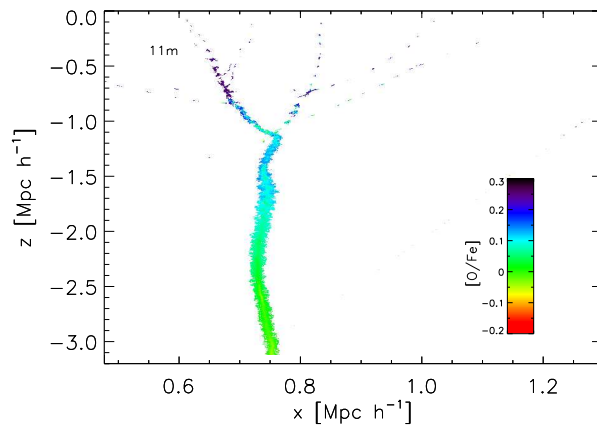
Figure 6.6: The $[\text{Fe}/\text{H}]$ metallicity distribution normalised to unity for all stars in 12m, (a), 11m, (b), and 10m, (c).

In general low-mass galaxies are observed to have higher gas fractions than high-mass galaxies (West et al., 2005; Geha et al., 2006). This observation may explain the observed mass-metallicity relation as low-mass galaxies are gas-rich due to their inefficiency to form stars because of their low surface densities (Kennicutt, 1998; Verde et al., 2002; Dalcanton et al., 2004). Supernova feedback, on the other hand, may also explain the relation. The supernovae expel gas via galactic winds and in this scenario, the loss of metals is more efficient in lower mass galaxies due to the shallower potential wells, resulting in the observed mass-metallicity relation (Veilleux et al., 2005). A mass-metallicity relation is apparent when we plot the $[\text{Fe}/\text{H}]$ distribution functions for the three different mass scale simulations, 12m, 11m, and 10m in Figure 6.6, where we have normalised the peaks to be equal to one so that the shapes of the distributions can be compared to one another (see Table 6.1 for the stellar mass of each simulation). The metal-rich end of the distribution function in 12m, (a), at $[\text{Fe}/\text{H}] \sim 0.5$ dex, disappears in the lower mass simulations, 11m and 10m. The $[\text{Fe}/\text{H}]$ distribution functions appear to be bimodal for all the simulations. 12m peaks at ~ -0.1 dex and again at the high end of the metallicity distribution, at ~ 0.2 dex. 11m peaks at ~ -0.1 dex, the same as the metal-poor peak in 12m, and again at lower metallicity, ~ -0.7 dex. It also shows a third peak at the metal-poor end of the distribution, ~ -1.3 dex. The lower-mass simulation, 10m again shows a bimodal distribution. The metal-rich peak is at similar metallicity as the metal-poor peak in the 11m simulation, at ~ -1.5 dex. The second peak in 10m is at a lower metallicity than the higher mass galaxies, 12m and 11m, peaking at ~ -1.7 dex.

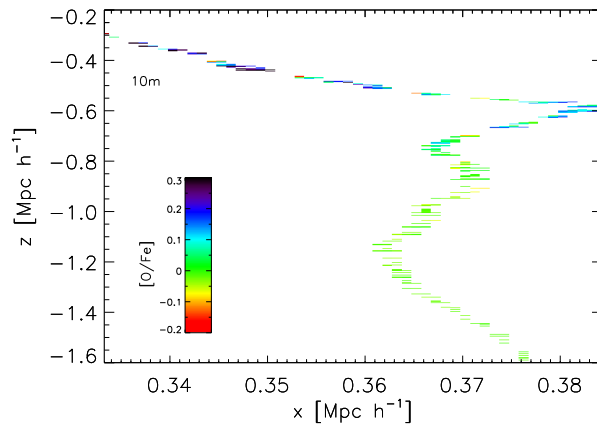
In Figure 6.7 we plot the stellar accretion histories colour coded by $[\text{O}/\text{Fe}]$. Comparing 12m with the scaled down version, 11m, the first observation is that the $[\text{O}/\text{Fe}]$ ratio are higher for longer in the higher mass galaxy 12m. In 11m, less gas which is enriched by the earliest star formation, and is hence enriched by SNe



(a) 12m

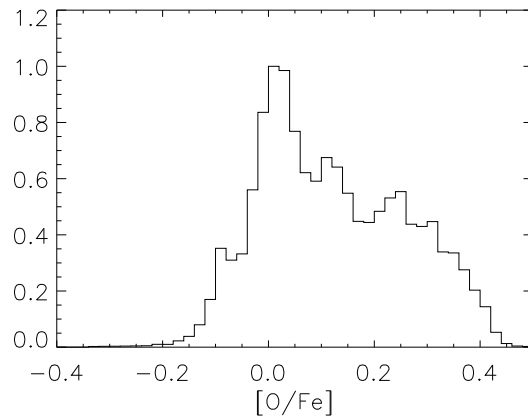


(b) 11m

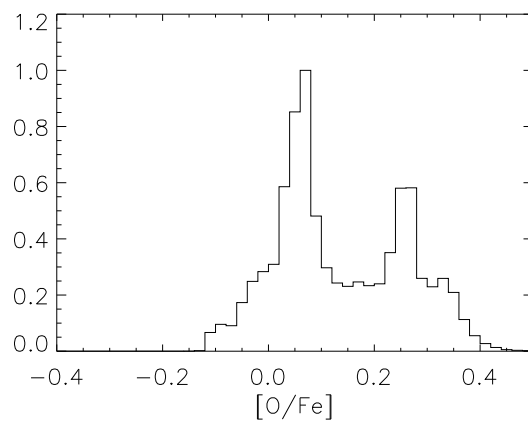


(c) 10m

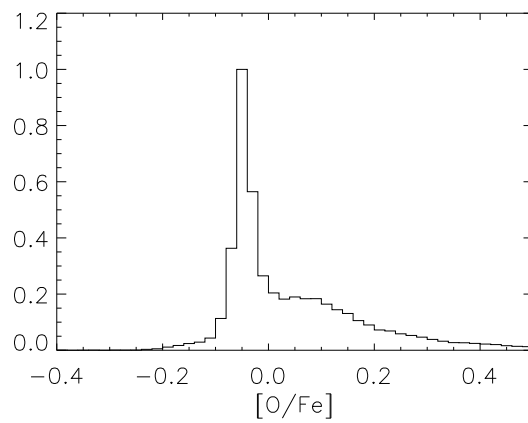
Figure 6.7: Stellar merger histories for each simulations colour coded with $[O/Fe]$.



(a) 12m



(b) 11m



(c) 10m

Figure 6.8: The $[O/Fe]$ metallicity distribution normalised to unity for all stars for 12m, (a), 11m, (b), and 10m, (c).

II, forms stars prior the onset of supernova type Ia, which enriches the ISM with Fe. Thus, the earlier progression to lower $[\text{O}/\text{Fe}]$ ratios in our lower-mass simulations is related to their lower star formation rates. Figure 6.7 therefore reflects the different star formation timescales in different mass galaxies (see Figure 6.2).

We plot in Figure 6.8 the $[\text{O}/\text{Fe}]$ distribution functions for all stars normalised to unity for comparison (see Table 6.1 for the stellar mass of each simulation). In 12m the $[\text{O}/\text{Fe}]$ has a fairly large spread, ranging from -0.2 to 0.4 dex. It is bimodal, peaking at $[\text{O}/\text{Fe}]\sim 0$ and then again at 0.25 dex. Comparing the high $[\alpha/\text{Fe}]$ end of the distribution in 12m, between 0.3 and 0.4 dex, with the lower mass simulations, there are more α -elements in the metals of 12m. 11m also has two peaks, one at ~ 0.07 and a second at ~ 0.3 dex. The lowest mass simulation 10m, shows slight bimodality, with a clear peak at ~ -0.05 dex and a slight peak at 0.1 dex. The low mass simulation, 10m, is particularly interesting as it has few stars with high $[\alpha/\text{Fe}]$ ratios. This trend is in agreement with observed dwarf galaxies (Venn et al., 2004).

The mass of a galaxy plays an important role in determining its final properties, such as, for example, its chemistry. We have shown how three simulated galaxies with the same merger histories at three different mass scales, have dramatically different properties. In the next section we will focus on the properties of individual populations in this context. We will try to understand whether the different populations within the simulations can be related to their hierarchical formation, and how this varies according to the mass of the galaxy, by examining the properties of the *accreted* and *in-situ* populations of the three simulated galaxies.

Table 6.1: The *Accreted* and *In-situ* Populations

Name	M_{vir} (M_{\odot})	$M_{stellar}$ (M_{\odot})	$M_{in-situ}$ (M_{\odot})	$M_{accreted}$ (M_{\odot})
12m	1.4×10^{12}	1.3×10^{11}	8.8×10^{10}	4.3×10^{10}
11m	1.9×10^{11}	1.4×10^{10}	1.4×10^{10}	9.6×10^7
10m	2.2×10^{10}	4.7×10^7	4.7×10^7	NA

6.4 The *Accreted* and *In-situ* Populations

We determine the *accreted* and *in-situ* populations in 12m, 11m, and 10m using the methods outlined in Chapter 5. The total stellar, *in-situ*, and *accreted* mass for each simulation is summarised in Table 6.1. The mass ratio of *accreted* to *in-situ* stars has gone from 0.48 in 12m to 0.0068 in 11m and in the lowest mass simulation, 10m, there are no accreted stars making this galaxy entirely of stars born *in-situ*. So by decreasing the mass of the galaxy we have dramatically decreased the amount of *accreted* stars.

In Figure 6.9 we plot the rotational velocity distributions for 12m, (a), 11m, (b), and 10m, (c) for stars in the solar neighbourhood, defined as $2.5 < R_{xy} < 3.5$ scalelengths and $|z| < 1$ scaleheights. We normalised the distributions to unity so that a direct comparison of the shapes between the different populations and different simulations can be made. We show both the *accreted*, in red, and *in-situ*, in blue, stellar populations in each galaxy in the plot. The high mass galaxy, 12m, has an *in-situ* and an *accreted* population which are rotating. The *accreted* population in this simulation lags the *in-situ* stars by only $\sim 50 \text{ kms}^{-1}$. Our medium mass galaxy, 11m, has a more clear separation between its two populations. The *in-situ* stars are nicely rotating, peaking at $\sim 120 \text{ kms}^{-1}$. The *accreted* stars, on the other hand, peak at $\sim 20 \text{ kms}^{-1}$, with a few accreted stars rotating with the *in-situ* population. The *in-situ* stars in both 12m and 11m would be consistent with a rotating disc, showing that these two galaxy have a

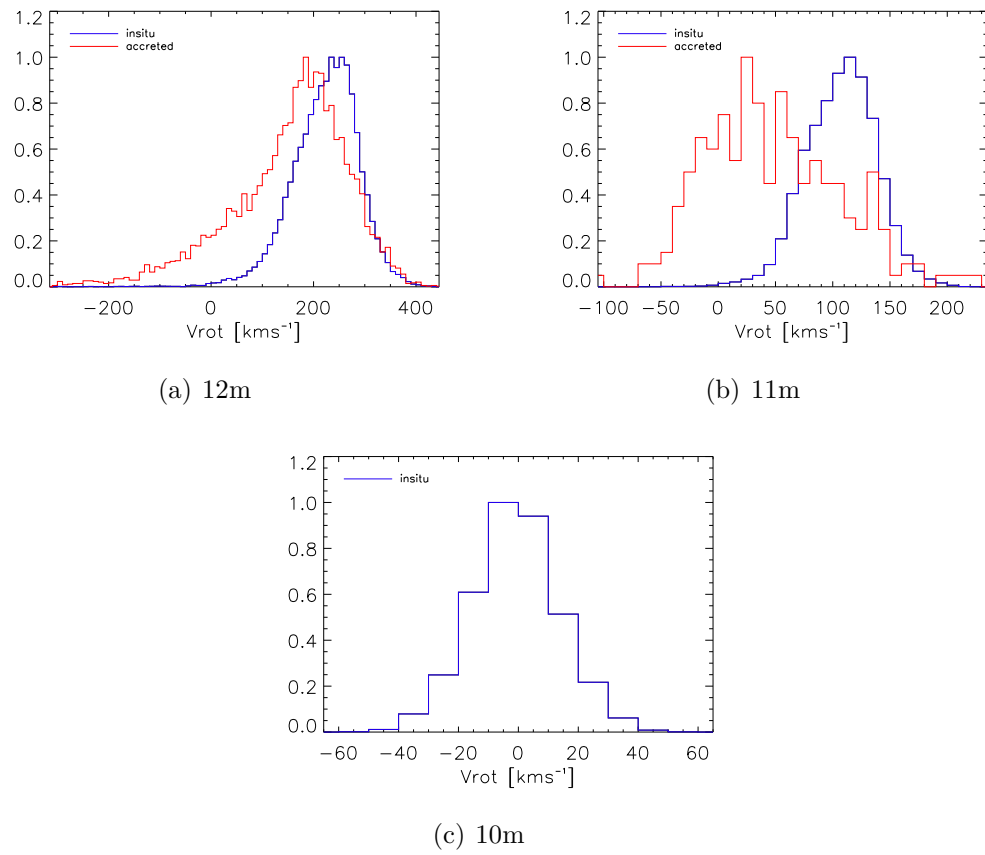
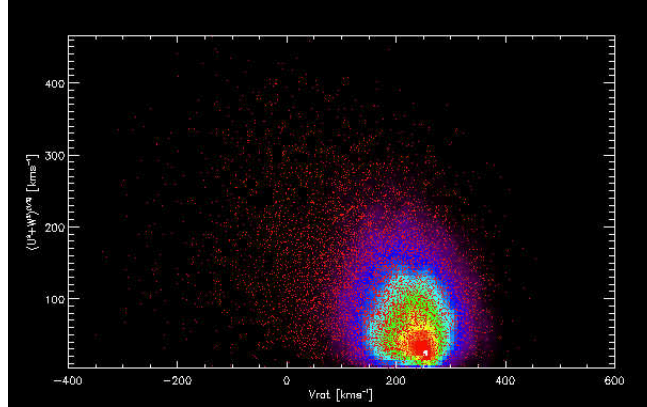
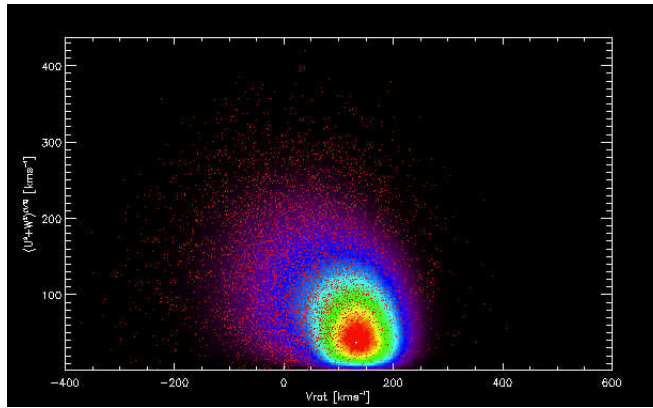


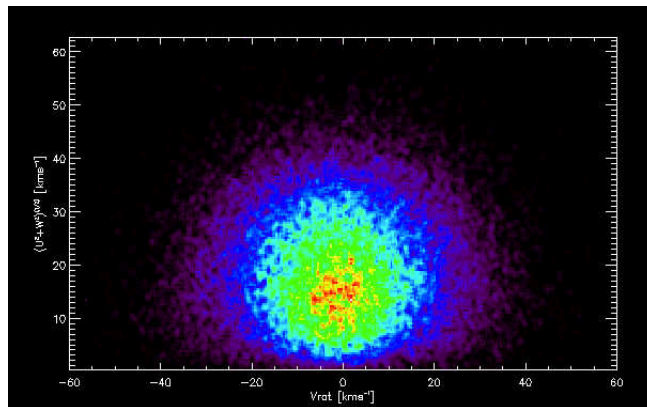
Figure 6.9: The rotational velocity distributions, normalised to unity, of all stars for 12, 11m, and 10m simulations showing both the *in-situ* (blue) and *accreted* (red) stellar populations.



(a) 12m



(b) 11m



(c) 10m

Figure 6.10: The Toomre diagrams ($T \equiv (U^2 + W^2)^{1/2}$ on the y-axis and V_{rot} on the x-axis) for stars in the disc for 12, 11m, and 10m simulations showing the *in-situ* distribution and *accreted* stars over-plotted.

component supported by rotation, characteristic of spiral galaxies.

To determine the nature of the *accreted* populations would require deeper investigation. For the moment we point out that in the case of 12m there are a large number of *accreted* stars which predominantly come from the last major merger. The significant rotational velocity of these stars is due to the angular momentum of this interaction. This gaining of angular momentum during the last major merger will be explored further in the next chapter. By contrast, in 11m there are fewer stars involved in the last major merger and the *accreted* stars end in a non rotating configuration. The 10m galaxy is comprised entirely of *in-situ* stars which are non-rotating. We plot their rotation velocity distribution in Figure 6.9 and shows that they have little or no net rotation. This lowest mass galaxy is not a typical spiral galaxy but rather its properties indicate it is a dwarf irregular galaxy.

In Figure 6.10 we plot the Toomre diagrams (Bensby & Feltzing, 2010) for each population, *accreted* and *in-situ*, in the solar neighbourhood in each simulation. The Toomre diagram plot rotational velocity, V , versus Toomre parameter $T \equiv (U^2 + W^2)^{1/2}$, where U is the radial and W is the vertical velocity. The *in-situ* stars are shown as a density plot, where the *accreted* stars are over-plotted as red dots. Toomre diagrams are often used to kinematically decompose galactic components. In our case we are distinguishing between the stars that are *in-situ* and those that are *accreted* and what their position is in velocity space. To confirm the results from the velocity distribution diagrams, the *in-situ* population in 12m and 11m show disc-like kinematics. The *in-situ* population in 10m show kinematics that better match non-rotating galactic halo stars, confirming the irregular nature of this galaxy. The *accreted* stars in 12m have similar kinematics to the *in-situ* stars, as well as a population that is kinematically distinct, with some *accreted* stars having extreme retrograde orbits ($V < -200 \text{ km s}^{-1}$) and others

having an extreme $T > 340 \text{ km s}^{-1}$. However, in both 12m and 11m there exist a significant overlap between the *in-situ* and *accreted* populations. Therefore the Toomre diagram is not a clean way to distinguish between these two populations.

6.4.1 Chemical Gradients

Above we looked at the global chemical properties at the three different mass scales and we showed that the final galaxies are chemically distinct. In this section we shall look at the chemical properties of the *in-situ* and *accreted* populations in each simulation and determine the effects that mass has on the properties of the populations.

In Figure 6.11 we show the $[\text{Fe}/\text{H}]$ metallicity distribution functions, this time decomposing it into *in-situ* stars (blue) and *accreted* stars (red). 12m shows some distinction between the *accreted* and *in-situ* stars. The peaks in the populations in this galaxy peak differ by ~ 0.1 dex, but have similar shapes. There is a low-metallicity tail in the *accreted* population between -1 and -2.5 dex, and a high metallicity population in the *in-situ* stars, peaking at ~ 0.1 dex.

The intermediate mass galaxy, 11m, shows significantly greater differences between its two populations than the two populations in 12m. The *in-situ* and *accreted* stars have clearly separate $[\text{Fe}/\text{H}]$ distributions, where the *in-situ* stellar population is more metal-rich than its *accreted* counterpart. The *in-situ* stars range between $-1.7 < [\text{Fe}/\text{H}] < 0.2$ dex, peaking at -0.4 dex. The *accreted* stars, which are much more metal-poor, range between $-3.3 < [\text{Fe}/\text{H}] < -1.5$ dex, peaking at ~ -2 dex. The *in-situ* stars show two peaks, one at high metallicity ~ -0.1 dex, and another with slightly lower $[\text{Fe}/\text{H}]$, at ~ -0.5 dex, that could indicate two components. The 10m $[\text{Fe}/\text{H}]$ was discussed above, as it only has one population, *in-situ*, of stars. Here we mention that it is a much more metal-poor *in-situ* population compared to the medium and high mass galaxies, 11m and 12m.

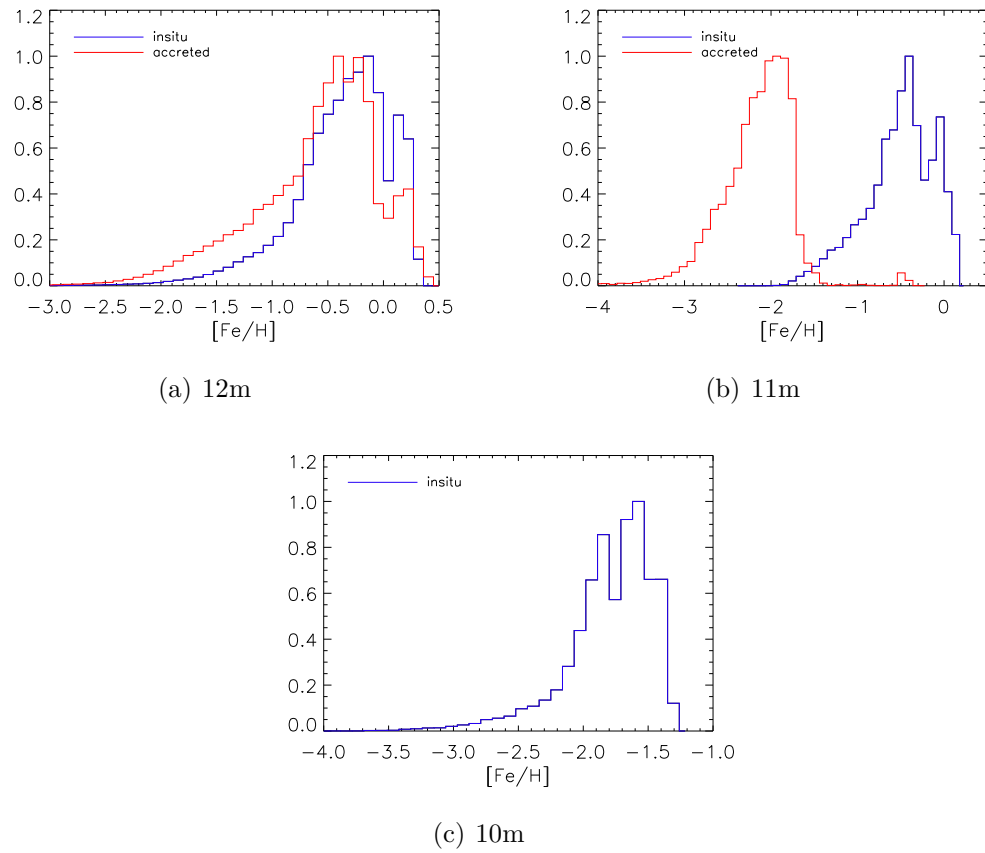


Figure 6.11: The metallicity distributions, normalised to unity, of all stars for 12m, 11m and 10m simulations showing both the *in-situ*, blue, and *accreted*, red, stellar populations.

However, it is not as metal-poor as the *accreted* stars in 11m.

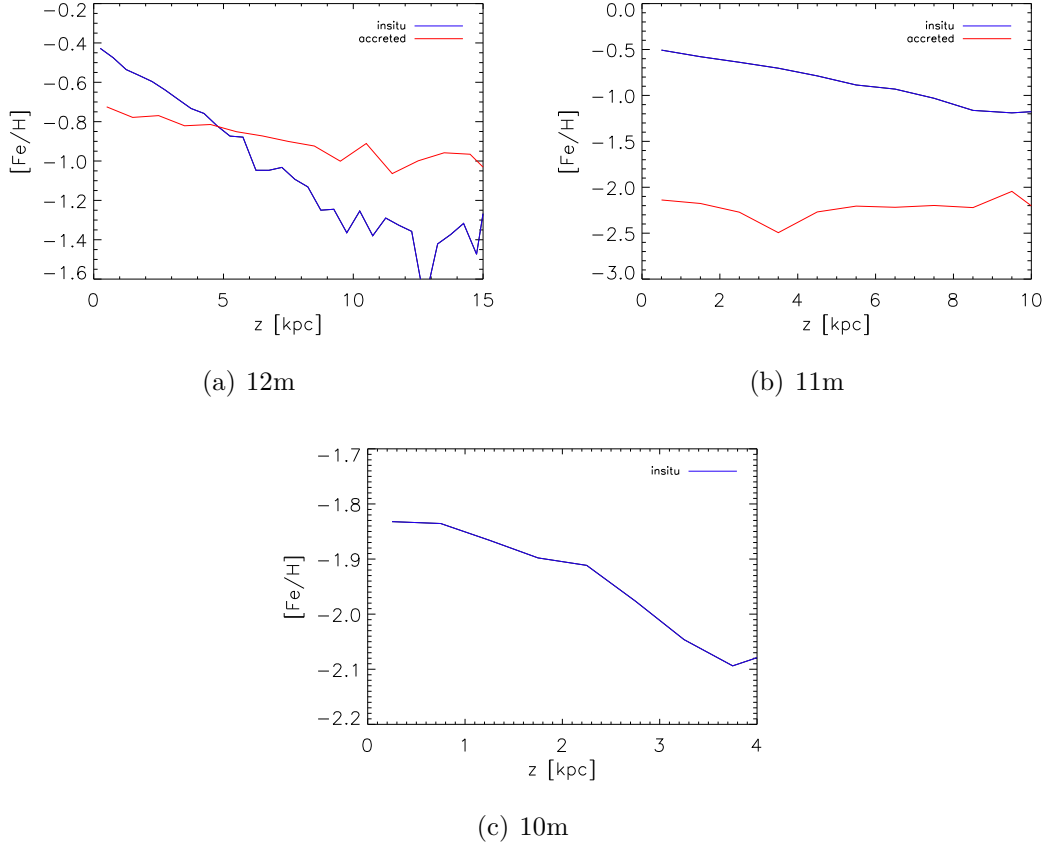


Figure 6.12: The average $[\text{Fe}/\text{H}]$ versus height (z) in the disc for 12m, 11m, and 10m simulations showing both the *in-situ* in blue and *accreted* in red, stellar populations.

In Figure 6.12 we plot the average $[\text{Fe}/\text{H}]$ as a function of height, z (kpc), above the plane to determine the vertical metallicity gradients in each population. The *in-situ* stars in 12m, Figures 6.12 (a), show declining $[\text{Fe}/\text{H}]$ with height, starting with an average $[\text{Fe}/\text{H}] \sim -0.4$ in the inner regions and dropping to ~ -1.4 dex in the outer parts. The *accreted* stars in 12m have lower metallicities in the inner regions, where they have, on average, $[\text{Fe}/\text{H}] \sim -0.7$ dex, but have a significantly shallower gradient, dropping to $[\text{Fe}/\text{H}] \sim -1.1$ dex in the outer regions. In 11m the *in-situ* stars also show a negative vertical gradient, although less pronounced

than in 12m, with an average $[\text{Fe}/\text{H}]$ in the inner regions of ~ -0.5 dex, decreasing to ~ -1.2 dex at 5 kpc above the disc plane of the galaxy. The *accreted* stars have fairly constant $[\text{Fe}/\text{H}]$, ~ -2.1 dex at all heights above the plane. In agreement with the other two simulations, the *in-situ* stars in 10m also have a significant vertical metallicity gradient. Starting at ~ -1.8 dex at the centre, the $[\text{Fe}/\text{H}]$ ratios drop to ~ -2.1 dex in the outer parts of the galaxy.

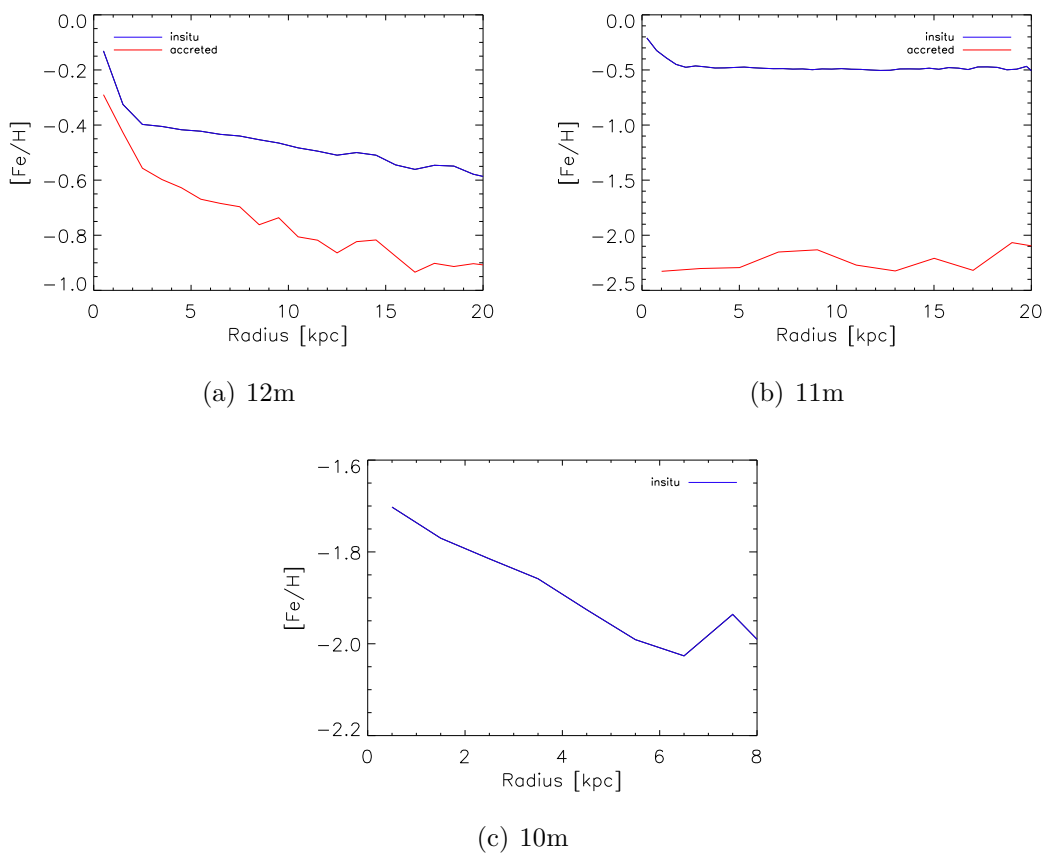


Figure 6.13: The average $[\text{Fe}/\text{H}]$ versus radius for 12m, 11m, and 10m simulations showing both the *in-situ* and *accreted* stellar populations.

Figure 6.13 plots the average $[\text{Fe}/\text{H}]$ as a function of radius for both the *in-situ* and *accreted* populations in 12m, (a), 11m, (b), and 10m (c). Both the *in-situ* and *accreted* populations in 12m show decreasing $[\text{Fe}/\text{H}]$ ratios with radius. The

in-situ populations in the inner regions have average $[\text{Fe}/\text{H}] \sim -0.3$ dex and decline to $[\text{Fe}/\text{H}] \sim -0.6$ dex at large radii. The *accreted* stars show a similar trend, where they start with $[\text{Fe}/\text{H}] \sim -0.5$ dex at the centre and decline to -0.9 dex at large radii. In 11m, both the *in-situ* and *accreted* stars, though distinct from one another, show relatively little radial gradients. The average $[\text{Fe}/\text{H}]$ for *in-situ* with radius is ~ -0.5 dex, although they do show a gradient in the inner regions, they are remarkably flat throughout the disc. The *accreted* stars have $[\text{Fe}/\text{H}] \sim -2.3$ dex at all radii on average. The stars in 10m have a steep radial gradient, going from -1.7 to -2.1 dex.

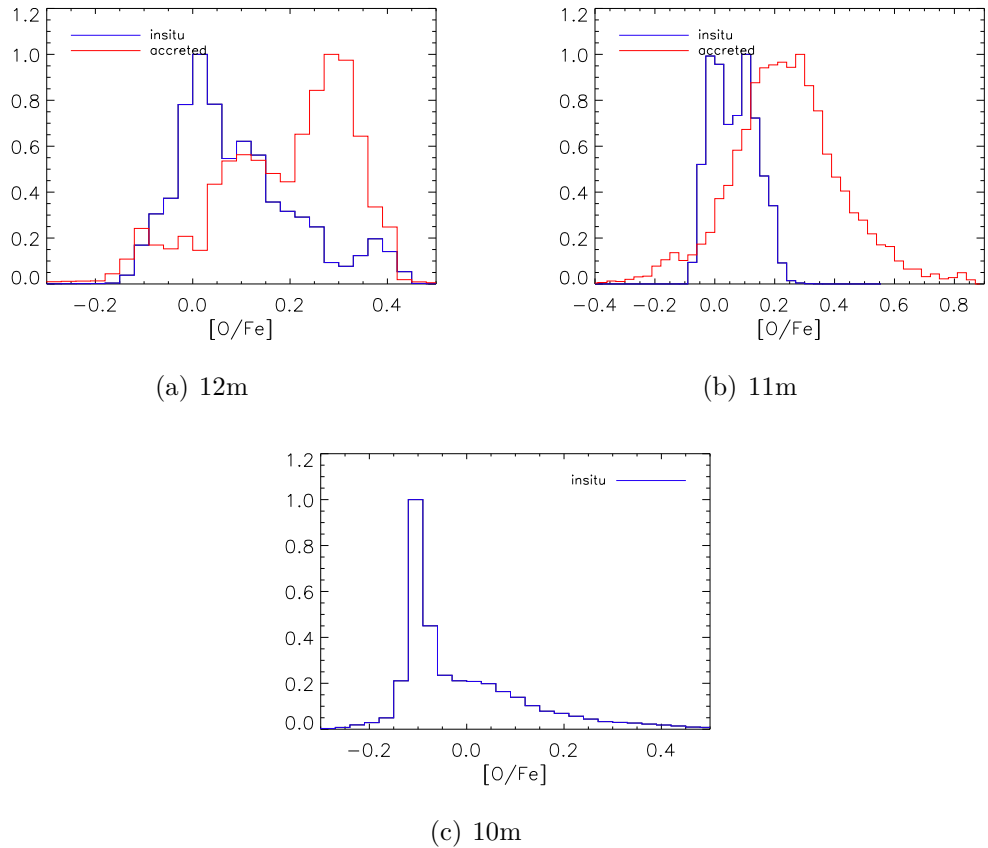


Figure 6.14: The $[\text{O}/\text{Fe}]$ metallicity distributions, normalised to unity, of all stars for 12m, 11m and 10m simulations showing both the *in-situ*, blue, and *accreted*, red, stellar populations.

In Figure 6.14 we plot the $[\text{O}/\text{Fe}]$ distribution functions for the two populations, *in-situ* in blue and *accreted* in red. In the $[\text{O}/\text{Fe}]$ distribution there is a clear distinction between the *accreted* and *in-situ* stars in 12m. The *accreted* stars peak at higher $[\text{O}/\text{Fe}]$ ratios, at ~ 0.3 dex. The *in-situ* stars have lower $[\text{O}/\text{Fe}]$ abundances, peaking at ~ 0 dex. Both the populations span the same range in $[\text{O}/\text{Fe}]$, between -0.3 to 0.4 dex. In 11m we again see a difference between the values of $[\text{O}/\text{Fe}]$ for the two populations. In this case, the *accreted* stars span a wider range than the *in-situ* stars, $-0.2 < [\text{O}/\text{Fe}] < 0.6$ dex, reaching higher values, and peak at ~ 0.3 dex. The *in-situ* population in $[\text{O}/\text{Fe}]$ has changed significantly at the two mass scales. In 12m they span the same $[\text{O}/\text{Fe}]$ range as their *accreted* counterparts only peaking at low $[\text{O}/\text{Fe}]$ and differ in the amount of high α -element stars, between 0.1 and 0.4 dex, where the *accreted* stars dominate the distribution at this end. The *in-situ* stars in 11m have a narrower distribution than the *in-situ* stars in 12m, ranging from -0.1 to 0.2 dex. By decreasing the mass, we have decreased the amount of high α -elements in the stars born in the main galaxy. The 10m simulation is dominated by stars with low $[\text{O}/\text{Fe}]$. What is notable is that the *accreted* population in 12m does not resemble either 11m nor 10m, i.e. the chemistry of the building blocks of 12m differ from the properties of the lower mass galaxies.

We plot the vertical gradients of $[\text{O}/\text{Fe}]$ for the *in-situ* and *accreted* stars in Figure 6.15. All the *in-situ* populations in the three mass galaxies have vertical gradients of $[\text{O}/\text{Fe}]$, going from low $[\alpha/\text{Fe}]$ ratios in the centre to high $[\alpha/\text{Fe}]$ at greater distances above the plane. The *accreted* stars in 12m and 11m show no vertical gradients.

The radial gradients of $[\text{O}/\text{Fe}]$ are shown in Figure 6.16. The radial gradient in $[\text{O}/\text{Fe}]$ are fairly flat in both 12m and 11m. Both the *in-situ* and *accreted* stars in 11m and 12m have more or less constant $[\text{O}/\text{Fe}]$ with radius. The *in-situ*

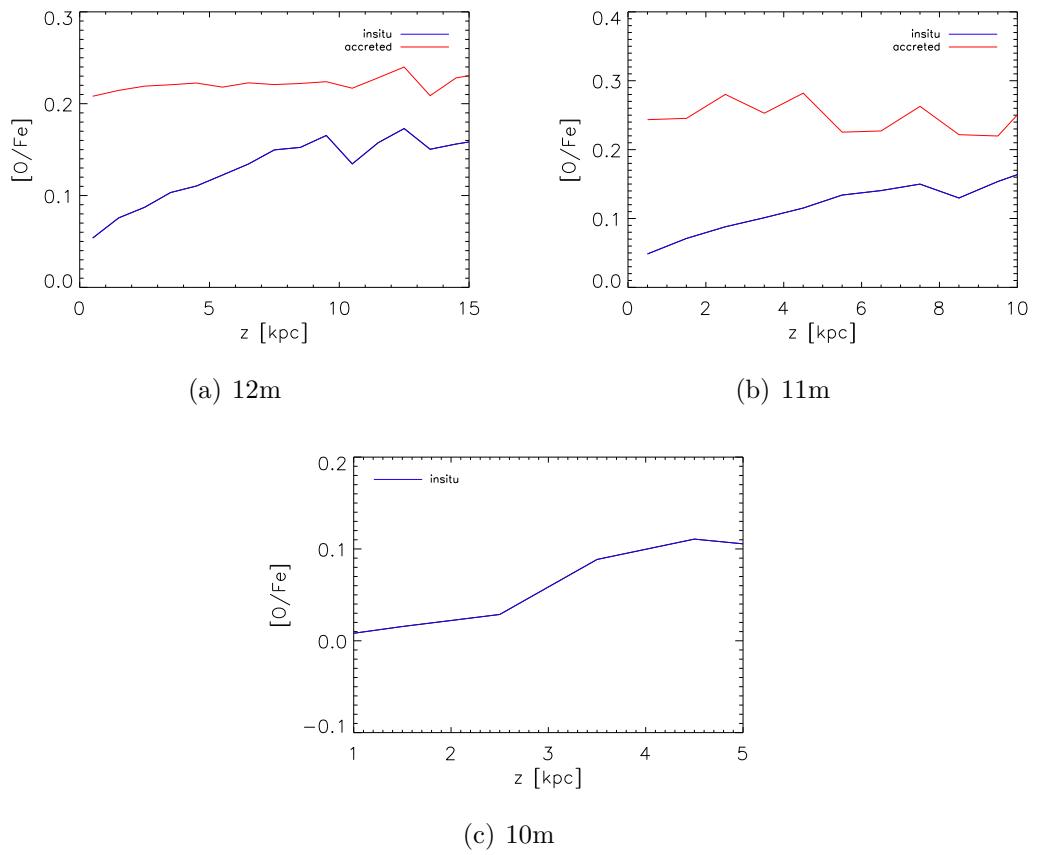


Figure 6.15: The average [O/Fe] versus height (z) for 12m, 11m, and 10m simulations showing both the *in-situ* (blue) and *accreted* (red) stellar populations.

and *accreted* stars in 12m have average $[O/Fe]$ of ~ 0.05 and ~ 0.2 , respectively. In 11m, the average $[O/Fe]$ in the *accreted* population is ~ 0.27 dex and average $[O/Fe]$ for the *in-situ* stars is ~ 0.15 dex. The stellar population in 10m have an increasing gradient with radius.

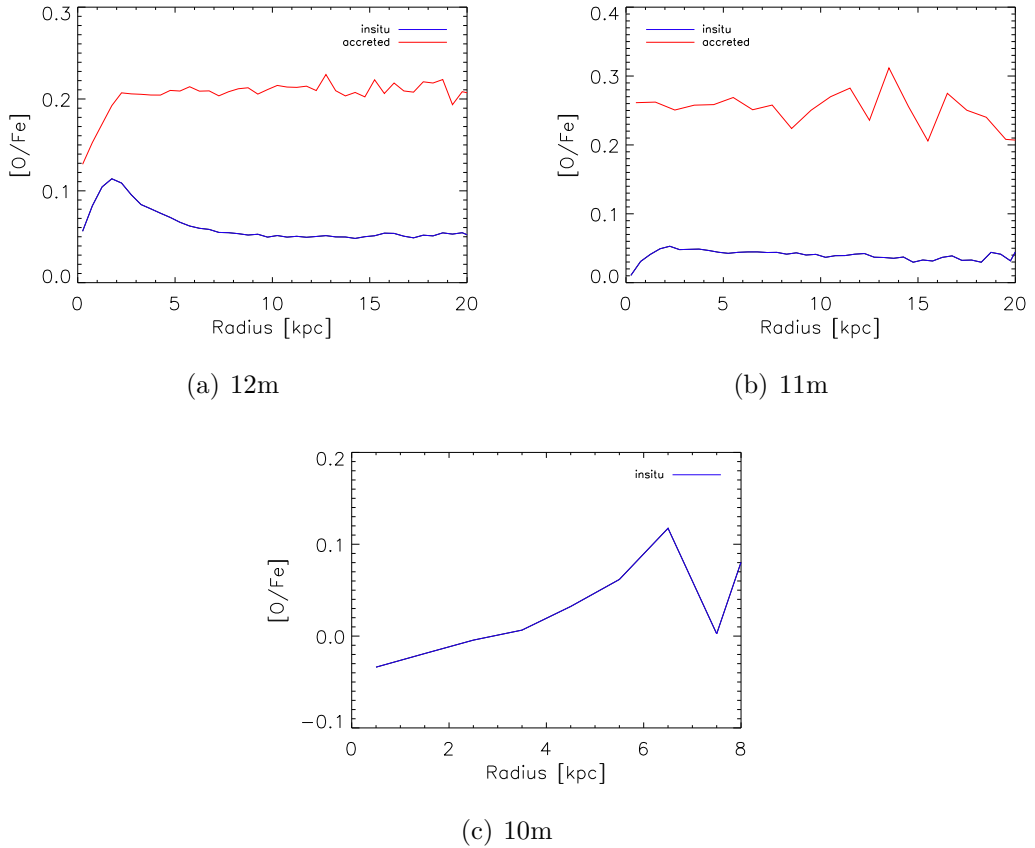


Figure 6.16: The average $[O/Fe]$ versus radius for 12m, 11m, and 10m simulations showing both the *in-situ* (blue) and *accreted* (red) stellar populations.

6.5 Conclusions

In this Chapter we have looked at a set of cosmological simulations run with the same initial conditions, only scaled down to obtain three different mass scales. We compared the stellar merger trees and the global chemical properties and

found that they differ significantly. Even though their dark matter merger trees are the same, the stellar accretion histories differ at each mass scale due to the fact that less stars are forming in the low mass building blocks of the lower mass simulations. We study how the different star formation rates affect their global chemical properties.

We found that as we go to lower and lower mass, we accrete less and less stars. In fact, our lowest mass simulation, 10m, is comprised entirely of *in-situ* stars. This is due to the fact that the lowest mass progenitors are unable to form stars as the gas ionised by the UV background radiation does not cool sufficiently. We analysed the kinematics, chemical properties and gradients of the *in-situ* and *accreted* populations in each simulation and found that although kinematically there may be overlap between the two populations, chemically they are quite distinct. There is a clear distinction between [O/Fe] ratios of *accreted* and *in-situ* stars in both 11m and 12m, indicating that metallicities can be used to distinguish these populations, more so than the kinematics. This can have important implications for the Milky Way's thick disc and stellar halo in determining their formation and evolution.

We found strong vertical gradients in [Fe/H] and [O/Fe] for *in-situ* stars for all masses but no clear gradients for the *accreted* stellar population. The trend with radius are less clear, with the intermediate mass galaxy, 11m, showing rather shallow gradients.

The *in-situ* slow contraction of a galaxy undergoing star formation and chemical enrichment during its formation will have an abundance gradient in the stellar component. In this context, stars in galaxies that form *in-situ* will exhibit abundance gradients where, for example, the mean metallicity will decrease with increasing galactocentric distance (Searle & Zinn, 1978). This is indeed what we observe in the *in-situ* stellar population in 12m, 11m and 10m, shown in

Figures 6.12 and 6.13.

Searle & Zinn (1978) measured the abundances of halo clusters in the outer halo of the Milky Way against galactocentric distance and showed that there was no evidence at all that the mean abundance decreased with increasing distance. They proposed that the globular clusters in the outer halo (>8 kpc) originate in protogalactic fragments that are *accreted* into dynamical equilibrium with the Galaxy. This is therefore in agreement with the lack of any clear abundance gradients for the *accreted* stars in our simulations.

An interesting overall result from this study is that the chemistry of the *accreted* stars in 12m do not look like the overall 11m nor 10m population, and the *accreted* stars in 11m also differ from the chemical properties of the lowest mass galaxy, 10m. This has important implications for the theory of hierarchical clustering in which it has been proposed that low mass galaxies are the building blocks of massive galaxies. This study shows that the building blocks of higher mass galaxies, such as 12m, differ from the properties of $z=0$ low mass systems, such as 11m and 10m. This can explain the differences between abundances of local dwarf galaxies and the abundances of stellar halos stars as shown in Shetrone et al. (2001); Tolstoy et al. (2003); Venn et al. (2004); Geisler et al. (2005) and which we will discuss in depth in the following chapter.

Chapter 7

Hierarchical Formation in Dwarf Galaxies

7.1 Introduction

As small mass structures are believed to merge to form larger structures in a hierarchical cosmology, it has been hypothesised that dwarf spheroidal galaxies may be the building blocks of more massive galaxies such as the Milky Way. If this were true, then the chemical signatures in these building blocks should resemble those in the Galactic components, e.g. halo, thick disc. It now seems that this is not the case as dwarf spheroidal galaxies in the Local group have distinct and unique chemical patterns when compared with the Milky Way components, therefore ruling them out as analogous to accretion fragments which build up the Galaxy (Shetrone et al. 2001; Tolstoy et al. 2003; Venn et al. 2004; Geisler et al. 2005). These studies found that no population of stars in the Galaxy is representative of stars in the low-mass dwarf galaxies. In Figure 7.1 it is shown that dSph stars are well separated from the majority of Galactic disc + halo stars. This was first found in Tolstoy et al. (2003).

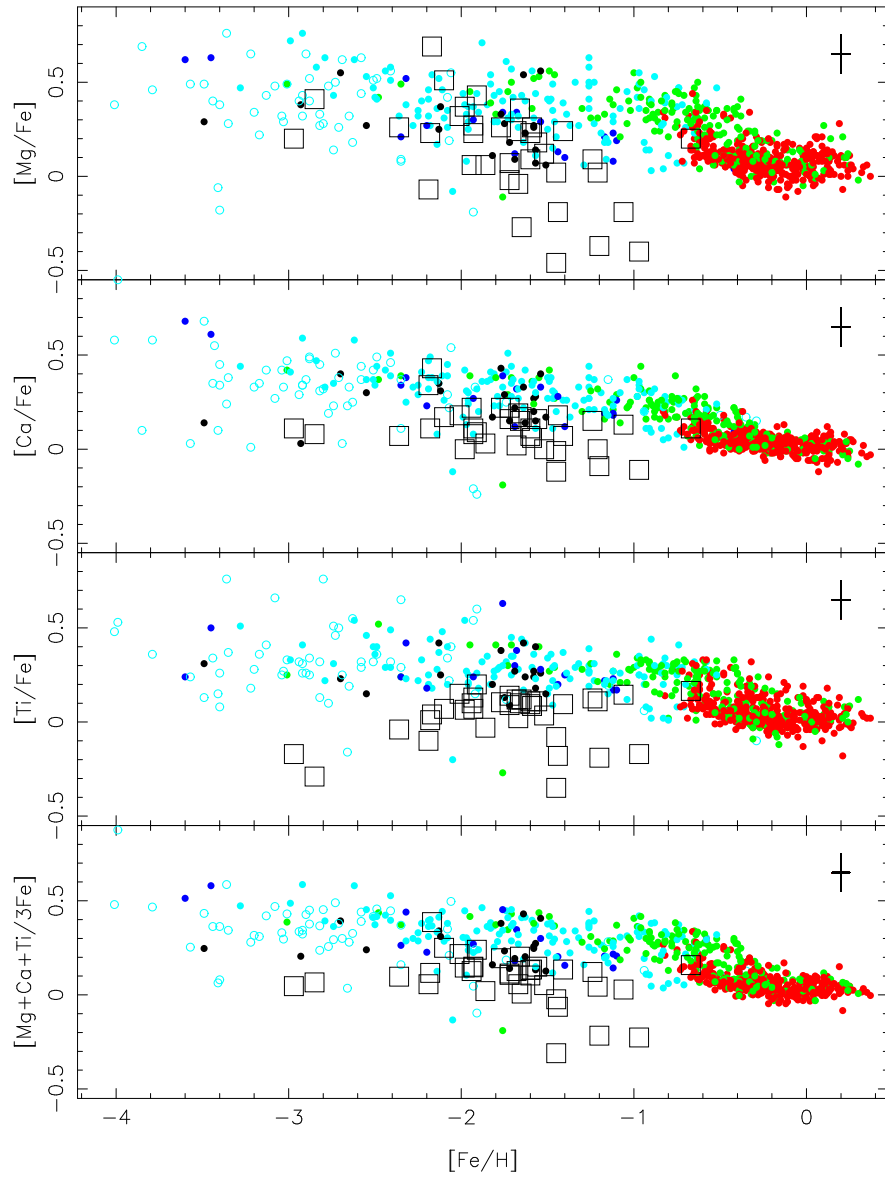


Figure 7.1: The $[\alpha/\text{Fe}]$ ratios as a function of metallicity, $[\text{Fe}/\text{H}]$, for the individual alpha components Ca, Ti, and Mg and the mean of the three (bottom panel), showing the Galactic thin disc stars (red), thick disc stars (green), and halo stars (blue). Over-plotted are data from Local Group dSph stars from Shetrone et al. (2001) and Geisler et al. (2005) (black squares). Open circles are stars without kinematics, taken from Venn et al. (2004).

Clearly the chemical signatures of stars in dSph galaxies are different from Galactic stars of similar metallicity. The dSph also seem to have broadly similar chemical signatures to one another. This strongly implies that no component of the Milky Way could have formed from the merger of galaxies similar to the low-mass dwarf spheroidal galaxies we see in the Local Group today as some Λ CDM models predict (Abadi et al. 2003a). However, it is still possible that merging at early epochs of dwarf galaxies could play a role in the formation of Galactic components. Some of the oldest stars in the dSph with low metallicity, $[\text{Fe}/\text{H}] \sim -2$, in Figure 7.1 have similar chemical signatures to Galactic halo stars. Therefore it is still possible that dwarf galaxies of this kind could have merged early on before significant star formation occurred.

Another possibility that cannot be ruled out is significant merging of higher-mass dwarf galaxies. It has been proposed that dwarf irregular galaxies, like the Large Magellanic Cloud (LMC), could instead represent the proto-galaxies responsible for the build up of Milky Way-type galaxies (Bekki & Chiba 2005; Robertson et al. 2005). Detailed studies of the LMC, however, have found that it has a different chemical pattern when compared to Galactic components (Pompéia et al. 2008). It should be noted that the stars probed in studies of the LMC, like those shown in Figure 7.2, are of intermediate ages and would therefore not have merged with the Milky Way halo or disc, if the accretion of LMC-like proto-galaxies occurred early on, at high redshift ($z > 1$), as is believed to be the case. So, in order to completely rule out this scenario of galaxy formation, detailed studies of the chemical abundances of older populations in dwarf irregular galaxies need to be undertaken and will be an interesting program for the next generation of telescopes.

Dwarf galaxies have been observed to have different stellar populations, which have been related to different components. Observations by Smecker-Hane et al.

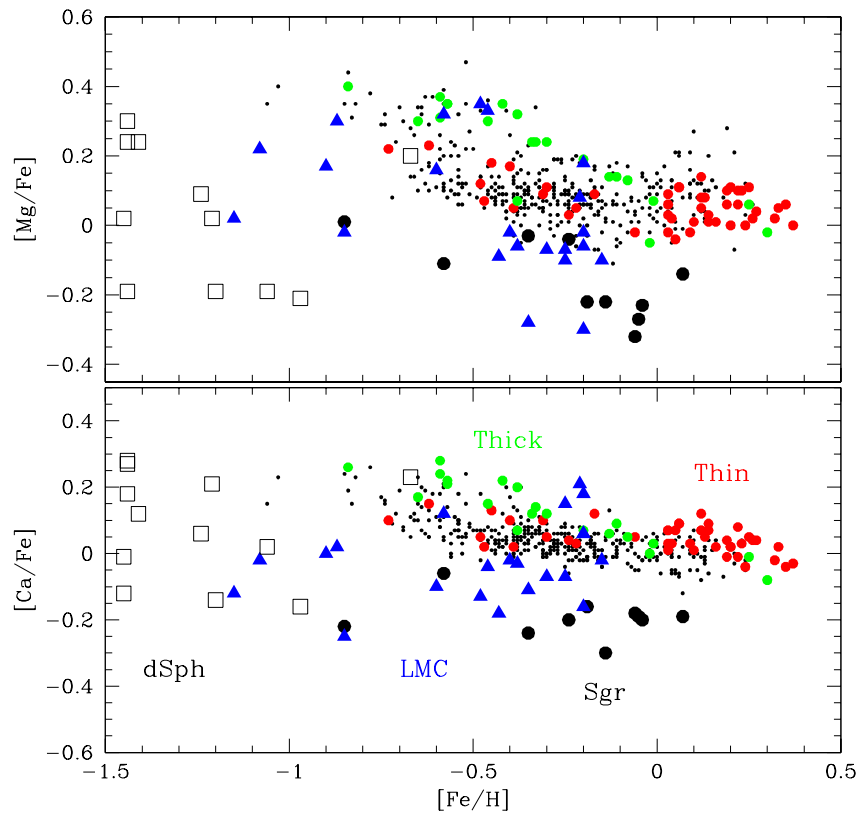


Figure 7.2: The $[\alpha/Fe]$ ratios as a function of metallicity, $[Fe/H]$, for the individual alpha components Mg and Ca, showing the Galactic thin disc stars (red), thick disc stars (green), and halo stars (black). Over-plotted are data from LMC stars (blue triangles) and Sagittarius Dwarf (black circles), taken from Venn et al. (2004).

(2002) found kinematically and chemically distinct components in the Large Magellanic Cloud (LMC), the closest dwarf irregular to the Milky Way. In this study they separate the two populations as two distinct components, a thin disc and a flattened stellar halo. Observations of isolated dwarf galaxies by Leaman et al. (2007) have also identified two components, defined as a rotationally supported disc and a more spheroidal component of older stars. Yoachim & Dalcanton (2006) found that dwarf galaxies also have thick as well as thin discs, in the sense that their vertical profiles are better fit by two disc components. Further, they found that thick discs tend to be thicker in dwarf galaxies than thick discs in higher mass galaxies, such as the Milky Way.

In the context of hierarchical formation, mass assembly is expected to be scale free. Yet as discussed in Chapter 6, baryonic physics has different effects at different mass scales. In this chapter, we ask whether hierarchical structure formation plays a role in forming the different stellar populations that are observed in dwarf galaxies. In observed dwarfs, the different populations are often associated with being standard components such as thin and thick disc, bulges and halos, even though it is not really clear that such galaxies have components of the same nature as more massive disc galaxies. Thus, the relation between these populations and galactic components will also be examined.

We will in particular examine the role of mergers and accretion in low mass galaxies. We analyse the surface brightness maps of *accreted* and *in-situ* populations, highlighting their morphologies as well as analysing their dynamical and chemical properties and how they reflect their different formation pathways. We examine the relationship between these two manners in which the dwarf galaxies get their stars, and galactic components (thin disc, thick disc, and stellar halo).

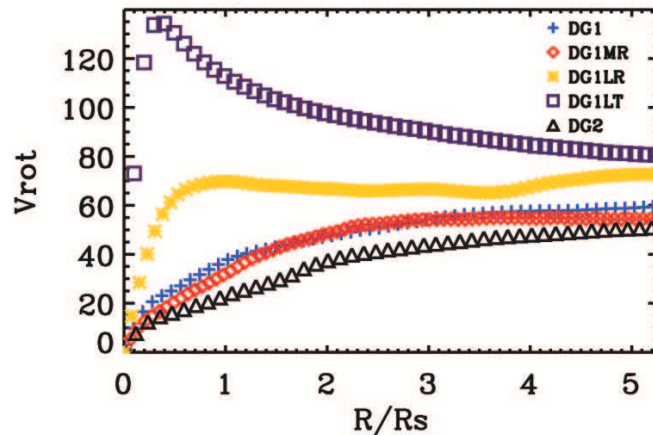


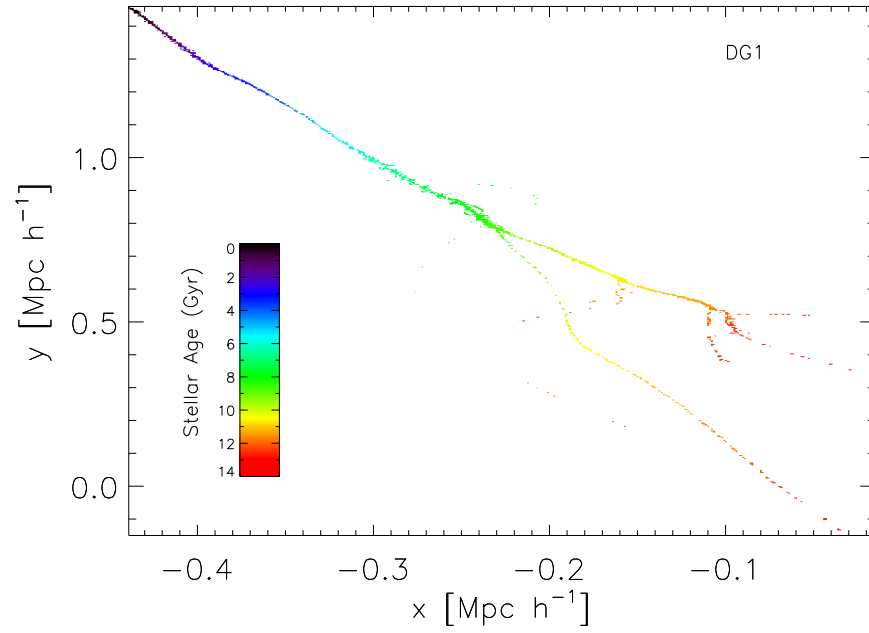
Figure 7.3: The rotation curve of the simulated dwarfs, DG1 (blue plus signs) and DG2 (black triangles), taken from Governato et al. (2010).

7.2 Dwarf Galaxy Simulations

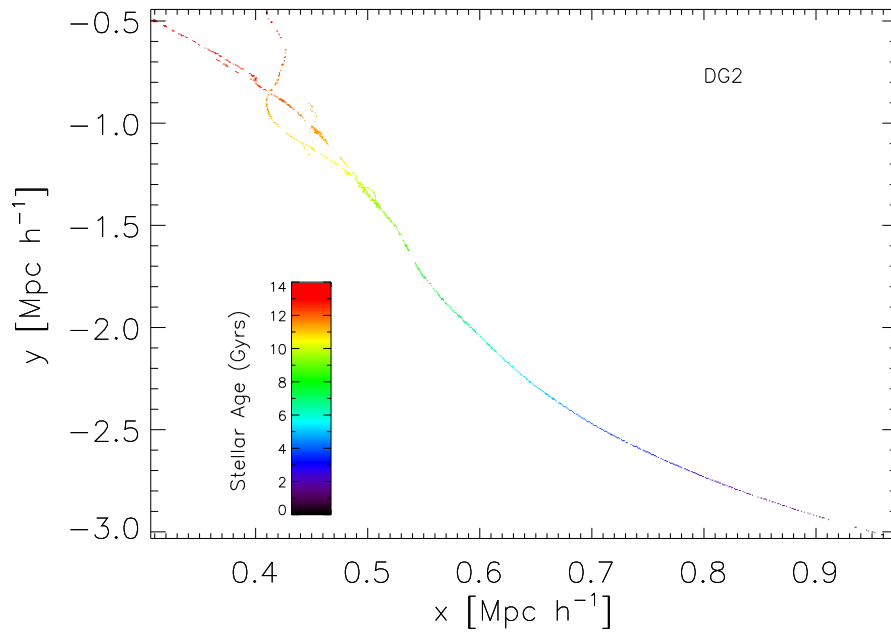
We analyse two dwarf galaxies both run with the fully parallel, N-body+smoothed particle hydrodynamics (SPH) code `GASOLINE`. These simulations can be found in Governato et al. (2010) and we shall refer to them as DG1 and DG2 throughout. For these dwarf simulations, star formation occurs when cold gas reached a given threshold density which is more typical of actual star forming regions. A threshold density of 100 amu/cm^3 is used as opposed to the more traditional value of 0.1 amu/cm^3 used in cosmological simulations.

At $z = 0$ the virial mass of the halos are $3.5 \times 10^{10} M_{\odot}$ and $2.0 \times 10^{10} M_{\odot}$, with $V_{rot} \sim 60 \text{ km s}^{-1}$ and $\sim 50 \text{ km s}^{-1}$ for DG1 and DG2 respectively (see Figure 7.3). Neither of the dwarf galaxies have a bulge component, and they match a multitude of properties of observed dwarf galaxies (Governato et al., 2010; Oh et al., 2010). This makes them a good test bed for analysing the formation history of dwarf galaxies.

The two dwarf simulations analysed in this chapter have different merger histories. DG1 assembled at $z \sim 3$ from three proto-galaxies, which have similar



(a)



(b)

Figure 7.4: The stellar merger histories colour coded with stellar age for DG1 (top panel) and DG2 (bottom panel).

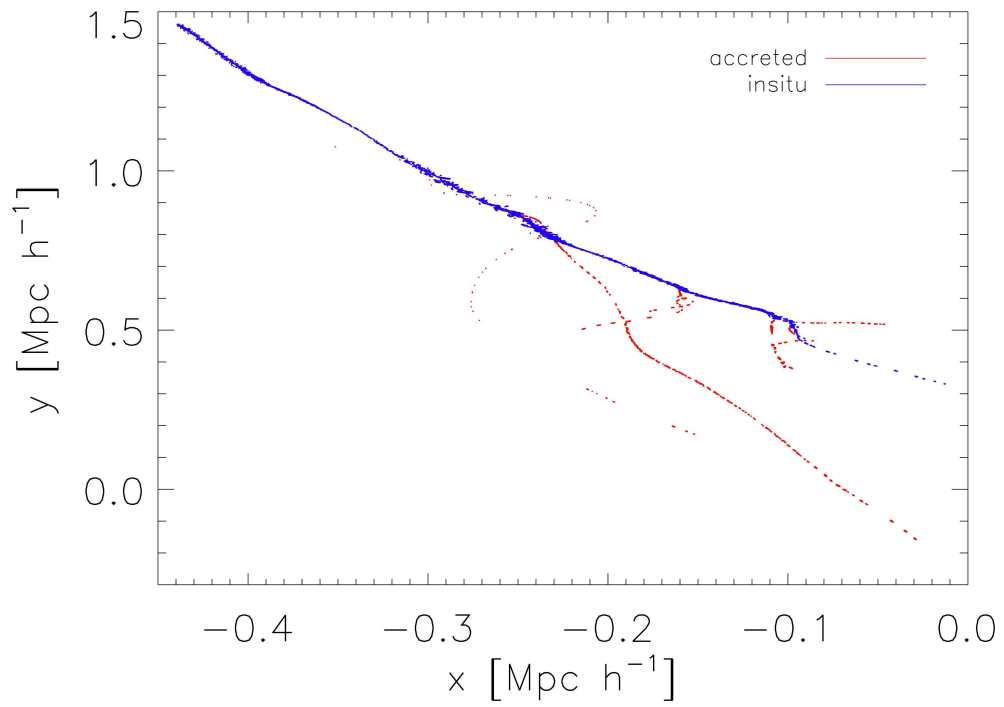
masses but themselves also have different merger histories. At $z \sim 1.2$, DG1 undergoes its last major merger (LMM) with a mass ratio of 3:1. This merger does not finally coalesce until $z \sim 0.9$. Due to this late LMM, we described DG1 as having a fairly rich merger history. DG2, on the other hand, has a much quieter formation history. Although its LMM has a higher mass ratio (1:1), it occurs much earlier in the galaxy's assembly, at $z \sim 2$. After this LMM, there are no more merger events, resulting in a quiet evolution for this galaxy hereafter. The LMM in both simulations can be seen clearly in Figure 7.5 where one can see the early merger in DG2 between ~ 11 and 10 Gyr ago and the later major merger in DG1 between ~ 9 and 7 Gyr ago. In both cases the accreted satellites are extremely gas rich with gas fractions of 90% for the satellite accreted in DG1 and 98% for the satellite accreted in DG2.

7.3 The *Accreted* and *In-situ* Populations

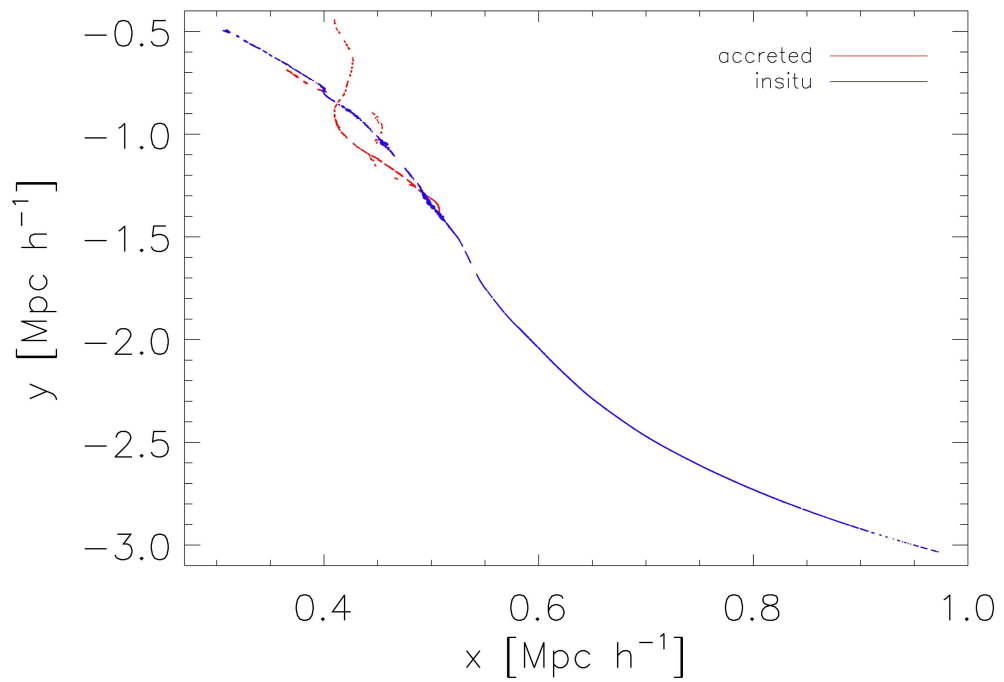
We have determined the *in-situ* and *accreted* populations for DG1 and DG2 using the methods outlined in section 5.3 from Chapter 5. We show the *in-situ* stars (blue) and *accreted* stars (red) for DG1 and DG2 in Figure 7.5. DG1 has total stellar masses of $M_{TOTAL}=4.3 \times 10^8 M_{\odot}$, $M_{INSITU}=3.9 \times 10^8 M_{\odot}$, and $M_{ACCRETED}=3.9 \times 10^7 M_{\odot}$. DG2 has total stellar masses of $M_{TOTAL}=1.7 \times 10^8 M_{\odot}$, $M_{INSITU}=1.2 \times 10^8 M_{\odot}$, and $M_{ACCRETED}=4.2 \times 10^7 M_{\odot}$.

7.3.1 Morphology and Profiles

We show mock surface brightness profiles in the *i*-band for the *accreted* and *in-situ* populations of our dwarf simulations in Figure 7.6 and Figure 7.7. The *in-situ* populations in both the simulations clearly show similar disc morphologies. The *accreted* stars are on the other hand quite different. DG2's *accreted* stars are far



(a)



(b)

Figure 7.5: The stellar merger histories for the *accreted* (red lines) and *in-situ* (blue lines) populations for DG1 (top panel) and DG2 (bottom panel).

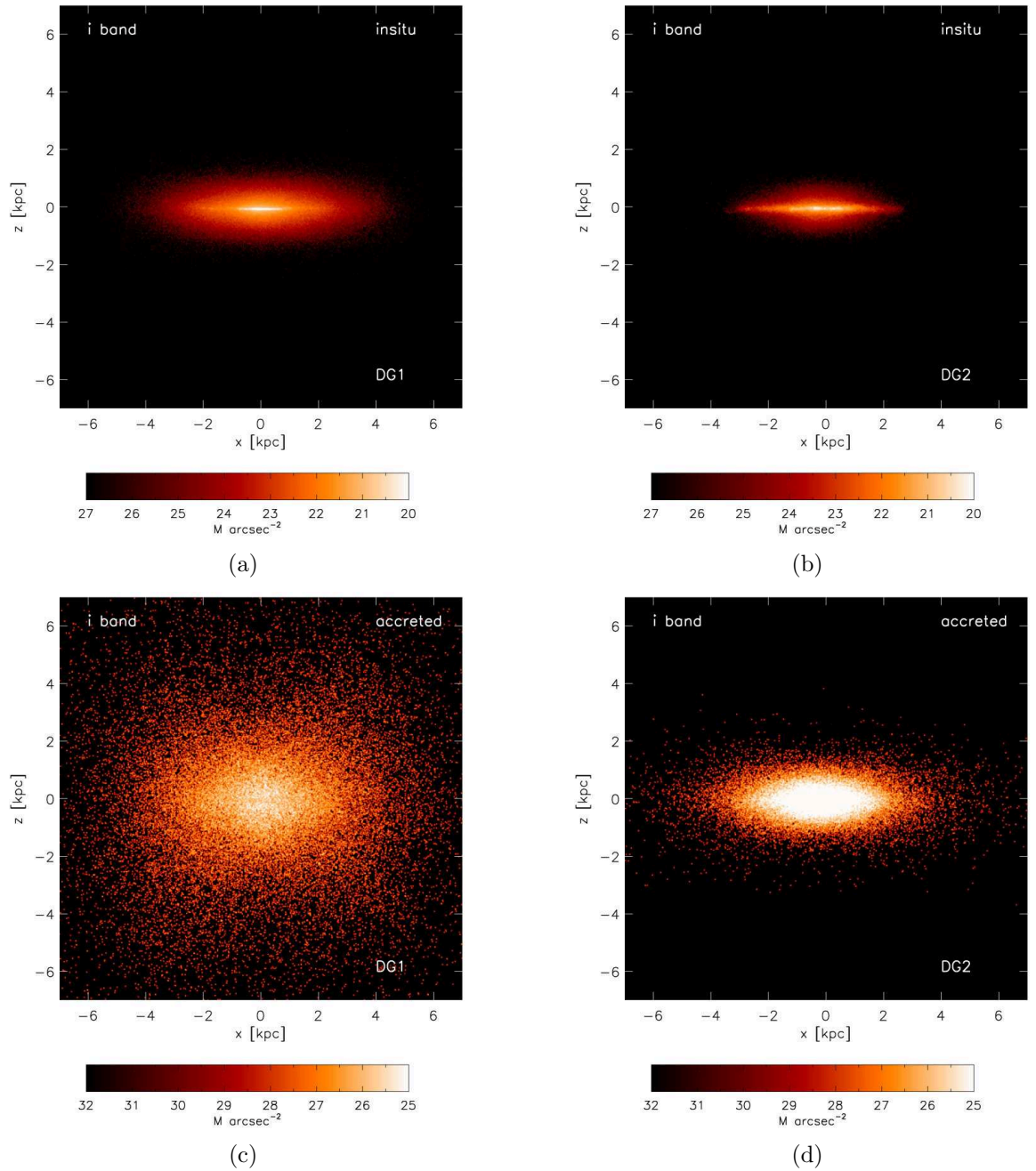


Figure 7.6: The dust reddened i -band surface brightness maps of DG1 (left panels) and DG2 (right panels) edge-on for the *in-situ* (top panels) and *accreted* (bottom panels) populations.

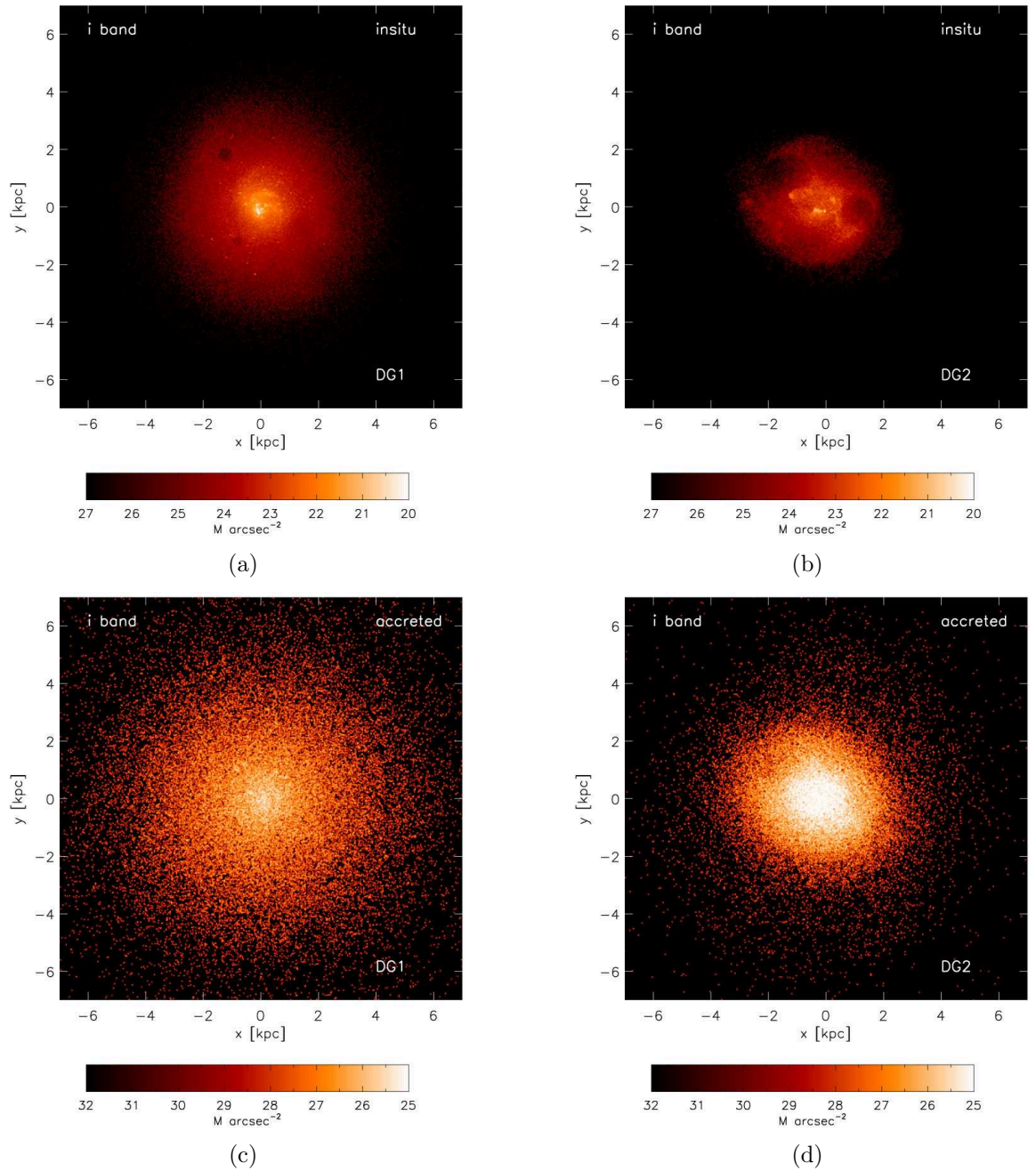


Figure 7.7: The dust reddened *i*-band surface brightness maps of DG1 (left panels) and DG2 (right panels) face-on for the *in-situ* (top panels) and *accreted* (bottom panels) populations.

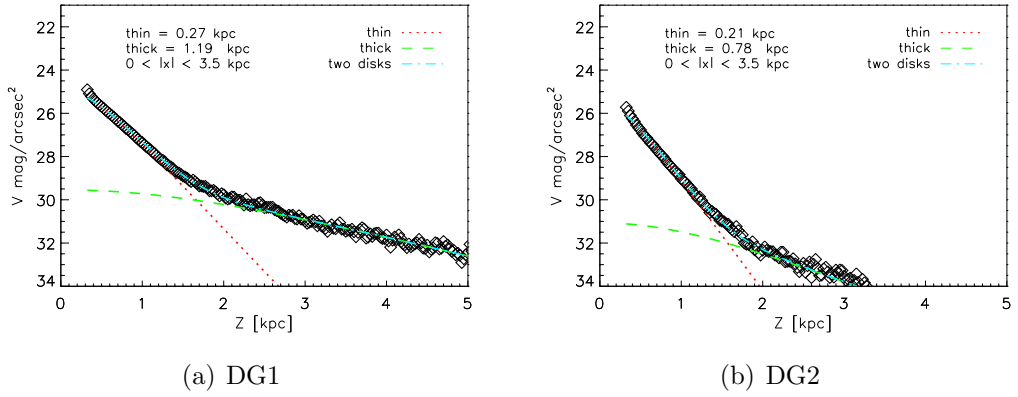


Figure 7.8: The vertical surface brightness profile for DG1 (left panel) and DG2 (right panel). Each profile is plotted along a broad vertical slit reported on the third line of each panel. A two-component sech^2 -function is fitted, turquoise dash-dotted line to the data points beyond 300 pc (the central region). The two separate fits are shown as the dotted red line and the dashed green line and are identified as the thin and thick components. The scale heights resulting from the two component fit are reported in the top of each panel.

more flattened in nature, whereas DG1's have a spheroidal distribution.

Figure 7.8 shows the vertical i -band surface brightness profiles for both the simulated dwarfs, DG1 (left panel) and DG2 (right panel). The vertical profiles are calculated along a broad slit, with position along the radius of the galaxy from 0 - 3.5 kpc. All the data points along this slit, excluding the inner 300 pc, are fitted with a two-component sech^2 function defined by:

$$F(z) = F_0 \text{sech}^2(z/h_z) \quad (7.1)$$

where F_0 is the central surface brightness and h_z is the scale height. The reason we exclude the inner regions in the fit is due to the effects gravitational softening may have on the shapes of the profiles in these central regions. We also fitted each component individually in the inner and outer regions with a single sech^2 function, and got similar scaleheights. The resulting scaleheights for each component are 0.27, 0.21, 1.19, and 0.78 kpc for DG1 and DG2's thin and

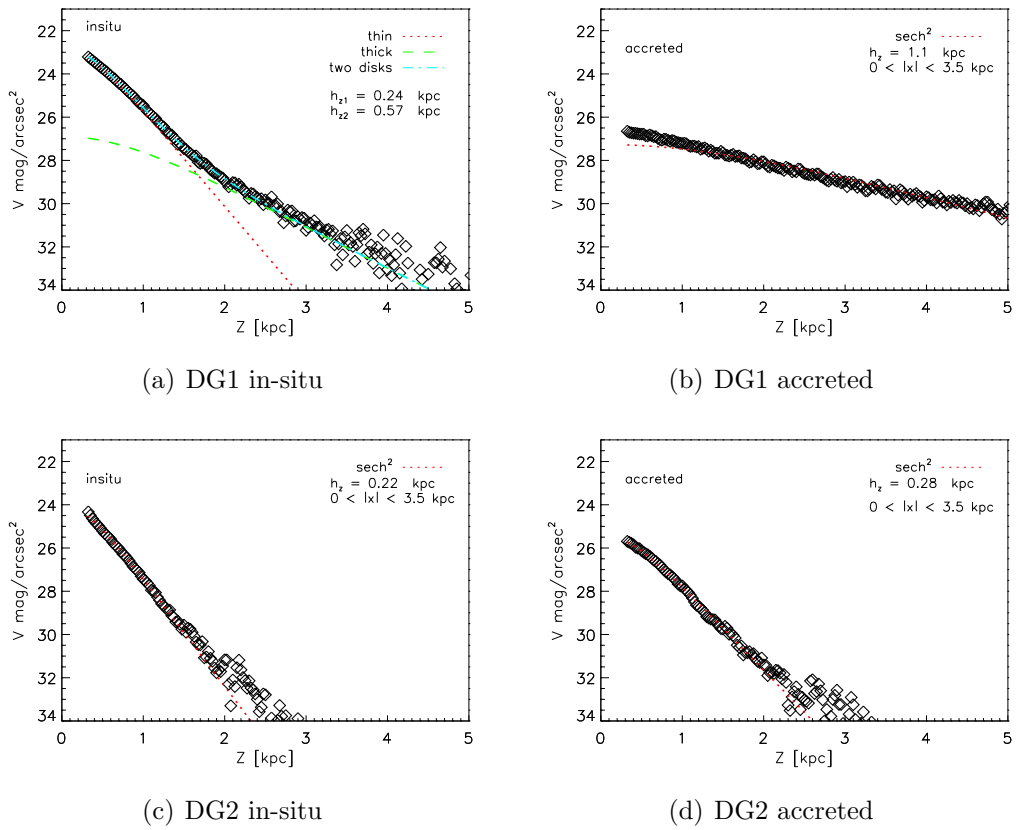


Figure 7.9: The vertical surface brightness profile for accreted and *in-situ* populations for DG1 (top) and DG2 (bottom).

thick components respectively. Measuring the vertical surface brightness and the scaleheights of the thin and thick components in each simulation already gives us a lot of information on the differences between these two galaxies. DG1 has a much more extended component up to at least 5 kpc above the plane than DG2, which drops off rapidly by 3 kpc. This extended component in DG1 is related to the spheroidal component seen in the mock images in Figures 7.6 and 7.7 and is dominated by *accreted* stars. DG2 has a far flatter nature confirmed by the smaller scaleheights calculated for both components.

The differences in the two galaxies' morphologies is reflected in the vertical surface brightness profiles for the *accreted* and *in-situ* populations for DG1 and DG2, which are plotted in Figure 7.9. The *in-situ* population in DG1 can be fit by a two component $sech^2$, indicating that there is a thin and a thick disc both formed *in-situ*, in the sense that the *in-situ* population in DG1 is better described as a two component structure. The *accreted* stars in DG1 are then fit with a separate $sech^2$ function as seen in Figure 7.9(b). An interesting observation in this figure is that the *accreted* stars in DG1 are not as well fit by a $sech^2$ function (see inner region in Figure 7.9(b)). This reflects the fact that this population has formed an extended stellar halo as opposed to a thick disc.

In DG2 both the *in-situ* and *accreted* stellar populations are well fit with a $sech^2$ function as shown in Figure 7.9 (c) and (d), emphasising the more flattened nature of this galaxy. The *accreted* stars in DG2 are well fit by a $sech^2$ function, unlike in the case of DG1, meaning that the accreted stars could be describing a thick disc component in this simulation.

The Accreted Population of DG2

There are several different ways one can distinguish between a galactic halo and a thick disc. In the Milky Way, we have detailed spatial, chemical and kinematic

Table 7.1: Properties from the $sech^2$ vertical profile fits for DG1 and DG2

Name	h_r kpc	h_z^{thin} kpc	h_z^{thick} kpc	h_z^{halo} kpc	μ_0^{thin} mag/arcsec ²	μ_0^{thick} mag/arcsec ²	μ_0^{halo} mag/arcsec ²
DG1	0.9	0.24	0.57	1.1	22.8	26.9	27.2
DG2	0.7	0.21	0.28	NA	24.0	25.4	NA

information of large numbers of stars which are used to determine components. For external galaxies, one often has to rely on measuring the *flatness* of the surface brightness map. By definition, we know that a thick disc must be a highly flattened component. We have measured the axial ratios of the *accreted* stars in DG1 and DG2 to determine their flatness, defined by the ratio of their scalelengths to scaleheights. The *accreted* stars in DG1 have a scalelength $h_R = 1.0$ kpc and a scaleheight $h_Z = 1.1$ kpc giving an axial ratio of $h_R/h_Z = 0.9$. Contrastingly, the *accreted* population in DG2 has a scalelength of $h_R = 0.75$ kpc and a scaleheight of $h_Z = 0.28$ kpc resulting in an axial ratio of $h_R/h_Z = 2.7$, meaning that DG2 is more flattened than DG1.

We plot in Figure 7.10 the axial ratios of the *accreted* population of DG1, plotted as a blue circle, and DG2, plotted as a red circle, along with axial ratios for the thick disc in external galaxies taken from Yoachim & Dalcanton (2006) Figure 16.

Observations of a large sample of disc galaxies by Yoachim & Dalcanton (2006) show that the axial ratio of thick discs tends to be larger than 2 (Figure 7.10). The *accreted* stars in DG2 are much more flattened than the *accreted* stars in DG1, with an axial ratio larger than 2, in agreement with thick disc as found in Yoachim & Dalcanton (2006). DG1, on the other hand does not fit well with measurements of thick discs with a less flattened nature. Therefore, the *accreted* population in DG1 does not form a disc component, but rather an extended stellar

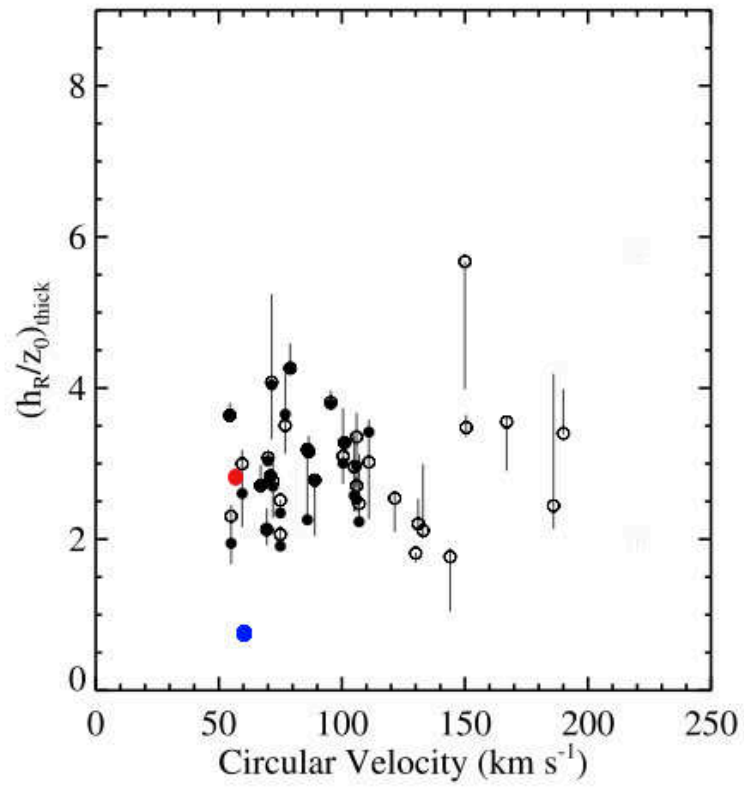


Figure 7.10: The axial ratios, h_R/h_Z , versus circular velocity of thick discs in external galaxies from Yoachim & Dalcanton (2006). We have over-plotted the accreted population of DG1 in blue and DG2 in red.

halo.

Zibetti et al. (2004), by stacking images over 1000 edge-on spirals from SDSS data, found that most of the stellar halos are slightly flattened, with an average axial ratio, $b/a \sim 0.6$ (where b and a are the minor and major axis when fitting an ellipse, as opposed to the scalelength, h_R , and scaleheight, z_0 , in Figure 7.10). However, a large statistical sample as well as measurements from more distant galaxies of stellar halos is extremely challenging and highly uncertain due to their faintness and the difficulty to observe deeper than $28 \text{ mag arcsec}^{-2}$ in the R -band.

Early-type galaxies are observed to have different properties and can be separated into two groups based on these differences into fast rotating, flattened ellipticals or S0 lenticulars, and slow rotating, spheroidal-type ellipticals (Cappellari et al. 2007; Emsellem et al. 2011). Theoretically they are usually associated with violent processes mainly driven by mergers and interactions in a hierarchical Universe. Simulations run by Burkert et al. (2008) show that the morphology of these two different early-type galaxies may be the result of differences in the mass ratio of the progenitors from which they formed as well as the amount of gas they contained.

Mergers at early times, when the stellar populations in elliptical galaxies were being born, were gas rich: the amount of gas involved in mergers will affect their end result. A number of numerical simulations have shown that fast rotating, flattened ellipticals result from mergers of stellar disc galaxies with mass ratios of 3:1 and 4:1 (Barnes & Hernquist 1998; Naab et al. 1999; Burkert & Naab 2003; Bournaud et al. 2005), and by including gas in these mergers they can form from 1:1 and 2:1 disc mergers, where the gas smoothly collapses to form a flattened stellar component, as shown by several studies (Barnes & Hernquist, 1996; Khochfar & Burkert, 2005; Springel & Hernquist, 2005). All these studies agree that gaseous dissipation leads to enhanced discyness or flattening in the

remnant. In Khochfar & Burkert (2005), they showed that gas rich mergers that produced discy ellipticals often lead to a secondary disc component.

Semi-analytic simulations by Khochfar & Burkert (2003) showed that there exists a tight correlation between the luminosity of ellipticals and the morphology of their progenitors. The most luminous, massive elliptical galaxies have suffered a last major merger between two elliptical progenitors, whereas low-luminosity galaxies formed from the merger of pure gas-rich spiral proto-galaxies. This would be the case for our simulated dwarf galaxy, DG2, as it is a low-luminosity system which experiences an early last major merger between two gas-rich spirals of similar mass. This is also in agreement with low-luminosity systems having their last major mergers earlier than high luminosity ellipticals and therefore also having enough time to grow a secondary secular disc.

These different formation scenarios for boxy and discy ellipticals will leave signatures in their structural properties. Observations of the surface brightness profiles of early-type galaxies (Lauer et al. 1995; Gebhardt et al. 1996; Faber et al. 1997) have shown that ellipticals can be divided into cored or power-law galaxies. High luminosity elliptical galaxies, formed from major mergers of spheroidal progenitors, show shallow inner profiles called cores. Low luminosity ellipticals, on the other hand, show much steeper inner profiles, fit with a power law. Moreover, Rest et al. (2001) found that it is very rare to find cores in discy-type ellipticals.

All the above studies and findings can be related to our simulated dwarf, DG2, and its *accreted* and *in-situ* populations. Instead of interpreting the *accreted* stars as the signature of a thick disc, it could be possible that this simulation is an example of a low-luminosity early-type galaxy that could be a discy elliptical and that perhaps the *accreted* population of DG2 is analogous to flattened fast rotating ellipticals. In addition, it has a second stellar disc component that formed secularly, as the simulations above produce, which in DG2 is the *in-situ* disc.

The *in-situ* population of DG1

The *in-situ* population in DG1 was found to be better fit with a 2 component $sech^2$ function, the first with a scaleheight $h_z = 0.24$ kpc and the second with a scaleheight $h_z = 0.57$ kpc. This indicates that DG1 seems to have a thin and a thick disc comprised of the *in-situ* stars (see Figure 7.9 (a)).

We look at whether the *in-situ* population in DG1 show signs of flaring by measuring the scaleheight at different radial slits. The measured scaleheight for the thick disc increases with radius. The thick disc scaleheight goes from 1.19 kpc in the inner most regions to 1.42 kpc in outer part. These signs of flaring in DG1 suggest that the thick disc could have formed from a merger induced scenario, where the previously existing *in-situ* disc is puffed up due to the interactions forming a thick disc. Observationally, signs of flaring in external spiral galaxies is difficult to measure due to the extremely low surface brightnesses levels required and surface photometry has not yet achieved this.

Morphology Summary

We propose that the *accreted* stars in DG2 do not form a thick disc like structure due to being dragged into a pre-existing thin disc by dynamical friction, as proposed by Abadi et al. (2003a). Instead, these *accreted* stars gain their angular momentum (see section 7.3.2), and also their flattened nature, from the early gas-rich major merger. We also suggest that this formation scenario may explain some, but not all, thick discs seen in external galaxies (Dalcanton & Bernstein, 2002; Yoachim & Dalcanton, 2006). The *accreted* stars in DG1 most likely form an extended stellar halo. The *in-situ* populations in DG2 forms a disc and we have found that the *in-situ* population in DG1 forms a thin and a thick disc, in the sense that this population is better fit by a two component $sech^2$ function. We will explore these components further when we examine the kinematics and

chemistry of the populations in the rest of the chapter.

7.3.2 Kinematics

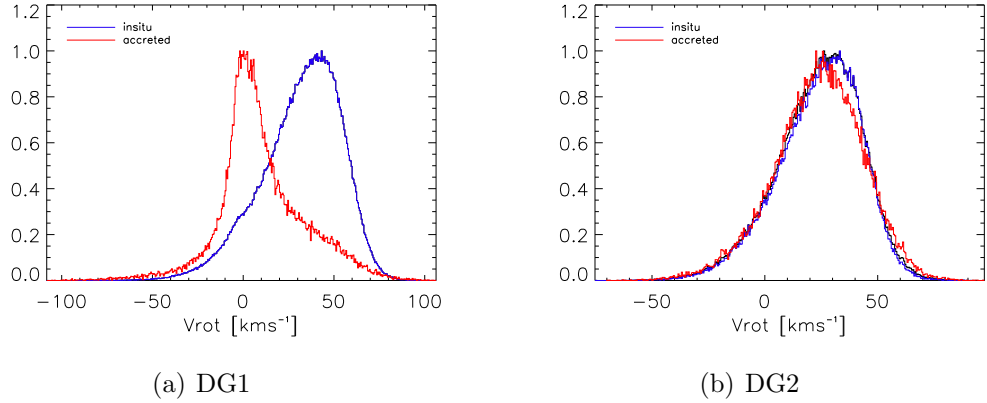


Figure 7.11: The rotational velocity histograms for DG1 (left panel) and DG2 (right panel) showing the accreted (red) and *in-situ* (blue) populations.

In Figure 7.11 we plot the histograms of the rotational velocities for *accreted* (red) and *in-situ* (blue) stars for DG1 (left panel) and DG2 (right panel). The *accreted* population in DG1 has little or no net rotation, while the *in-situ* population is rotating on average at $\sim 40 \text{ km s}^{-1}$. In DG2 the *accreted* population is quite different. From Figure 7.11 (b) it is apparent that it is rotating with an average rotation of $\sim 25 \text{ km s}^{-1}$, which is only 5 km s^{-1} slower than the *in-situ* population. We can relate this behaviour to the distinct merger histories of DG1 and DG2. DG2's LMM at $z = 2$ had a mass ratio of 1:1, and the merger was prograde. The angular momentum of the system today was gained from the LMM of two galaxies of similar mass. The *in-situ* and *accreted* population have merged and adopted similar velocities and formed the more flattened structure of DG2. DG1, on the other hand, had its LMM later on with a lower mass ratio (3:1) and a higher angle of inclination with respect to the plane of the central

disk than occurred in DG1. This results in an *accreted* population that does not resemble that of its *in-situ* partner and also assembles with a larger scaleheight. We can therefore determine that the *accreted* population in DG1 forms part of an extended spheroid and the *accreted* population of DG2 forms part of a generally more flattened, rotating object, perhaps an analogue to fast rotating elliptical galaxies, which also have relatively high ellipticities. The details of the mergers that take place to build up galaxies, like the mass ratio, time, orbits, and density, are therefore an important factor to determine the different nature of components in galaxies.

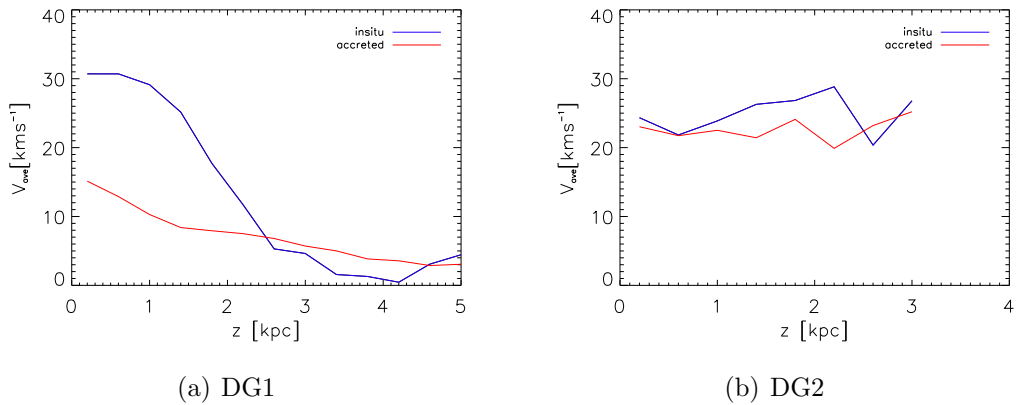


Figure 7.12: The average rotational velocity as a function of height (z) for DG1 (left panel) and DG2 (right panel) for both *in-situ* (blue) and *accreted* (red) stellar populations.

In Figure 7.12 we plot the average rotational velocity as a function of height, z , above the plane of the galaxy for the *in-situ* (blue line) and *accreted* (red line) for both DG1 (left panels) and DG2 (right panels). The average rotational velocity for the *in-situ* stars in both the simulations is between 20 and 30 km s^{-1} . You can also see in both galaxies that the *in-situ* population does not extend past ~ 2.5 kpc above the disc plane emphasising the disc like nature of this population. This has been previously shown in the spatial distribution of *in-situ* stars in Figure 7.6 (a)

and (b). The *in-situ* stars in DG1 have a velocity gradient with height above the plane, where the rotational velocities go from $\sim 30 \text{ km s}^{-1}$ in the central regions to $\sim 5 \text{ km s}^{-1}$ at a distance of 2.5 kpc above the plane. The *in-situ* population in DG2, on the contrary, does not show a rotational velocity gradient with height, where the average rotational velocity for the *in-situ* stars in DG2 is $\sim 25 \text{ km s}^{-1}$ both in the inner regions and out to 2.5 kpc.

The *accreted* stars in DG1 extend further out, beyond 5 kpc above the plane (see Figure 7.6 (c)). They also show a gradient with height with an average rotational velocity of $\sim 15 \text{ km s}^{-1}$ in the inner regions, going down to about $\sim 3 \text{ km s}^{-1}$ in the outskirts of the galaxy, at about 5 kpc above the plane. The *accreted* stars in DG2, however, do not have vertical velocity gradients and have large average rotations, $\sim 25 \text{ km s}^{-1}$, in the inner and outer parts. These *accreted* stars do not extend past $\sim 2.5 \text{ kpc}$, reflecting their flattened nature.

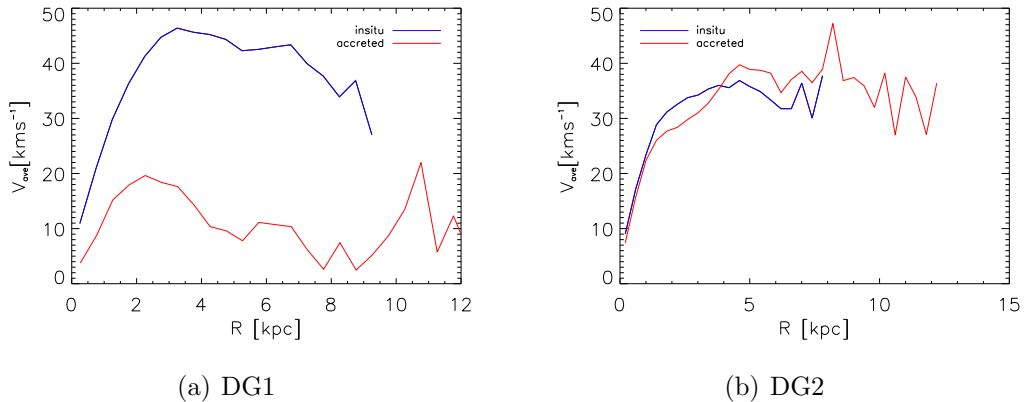


Figure 7.13: The rotational velocity as a function of radius for DG1 (left panel) and DG2 (right panel) for both *in-situ* and *accreted* populations.

Figure 7.13 shows the rotational velocities as a function of radius for DG1 and DG2. Again, these plots describe the rotating nature of both the *in-situ* populations as well as the non-rotating *accreted* population in DG1 and the fast rotating second component formed from *accreted* stars in DG2.

The *in-situ* population of DG1

The *in-situ* population of DG1 is comprised of a thin and thick disc as we have shown in section 7.3.1. We want to determine which process, i.e. kinematic heating via mergers or gas rich building blocks, is forming the thick disc of *in-situ* stars in DG1. We make use of our previous analysis in section 3.2.1 where we can establish whether disc stars are being heated, as the merger induced heating scenario proposes, or whether they are born hot through gas rich mergers.

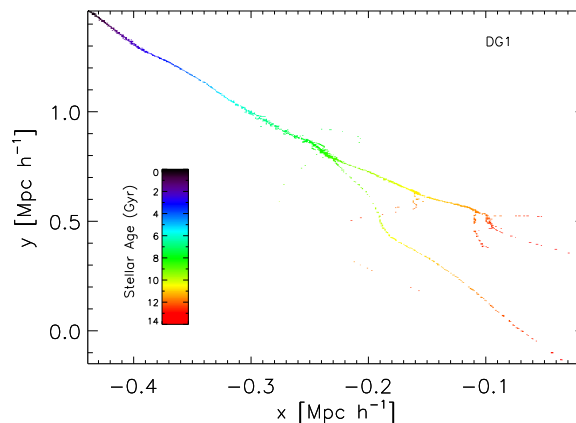


Figure 7.14: The stellar merger tree for DG1 colour coded with stellar age.

In Figure 7.14 we plot the stellar merger history for DG1 and we colour code it by star formation time. The last major merger (LMM) for the simulation is clearly visible in this plot at ~ 8.4 Gyr ago. There is a minor merger before the LMM also visible in the merger plot at ~ 10.3 Gyr ago.

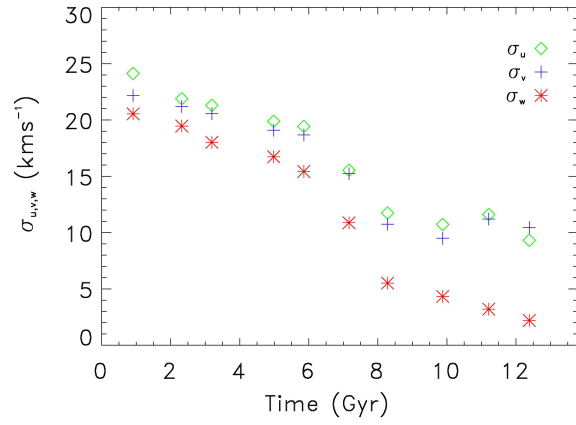
The age-velocity dispersion can be used to determine whether there is gradual heating in the disc, for example the continual rise of the velocity dispersion with age as seen in Holmberg et al. (2008). We measured the radial (σ_u), tangential (σ_v) and vertical (σ_w) velocity dispersions as a function of age in DG1 for our *in-situ* population shown in Figure 7.15 (a). There is clearly an abrupt increase

in the distribution for older stars (left hand side of the plot). There is a clear distinction between the old hot thick disc stars and the young cold thin disc stars in Figure 7.15.

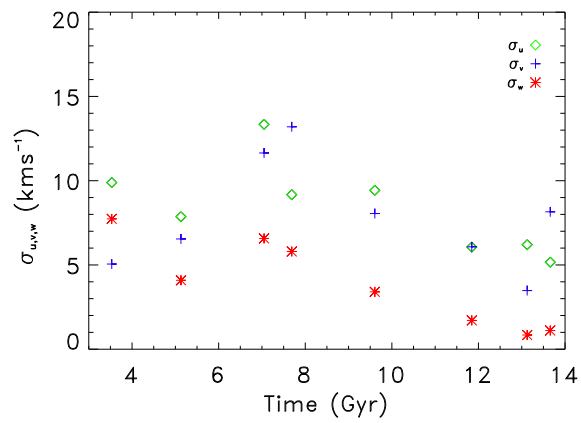
We plot the velocity dispersion of *in-situ* stars at birth in a disc region we have defined by $1 < R_{xy} < 4$ kpc and $|z| < 0.5$ kpc (middle panel of Figure 7.15). Because this simulation is bulgeless (see Governato et al. (2010) and Figure 7.3), choosing a radial cut in an inner region will not contaminate our disc sample. In Figure 7.15 (b), where we plot the velocity dispersion of stars at birthtime, old stars are born with higher dispersions than younger stars, again showing a clear distinction between old hot thick disc stars and cold young thin disc stars. This means that the thick disc in DG1 is formed hot. The mergers at these early times, when the thick disc is forming, have large gas fractions (see Brook et al. 2011 for details).

Finally we want to determine whether the stars remain with the same velocity dispersion as when they were born or if they are being heated subsequently. In Figure 7.15 (c) we measure the amount of heating that the *in-situ* stars in DG1 undergo. The thick disc stars at early times are heated dramatically, whereas the younger stars show very little heating. Both the minor and major mergers in DG1 (see Figure 7.14) heat up the stars in the disc substantially, increasing their dispersion by a factor of three.

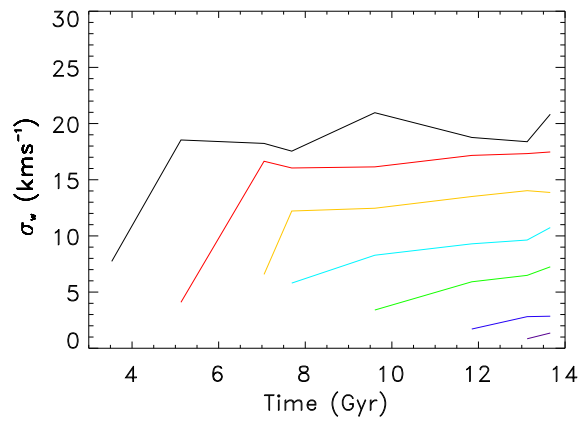
The stars in the disc region in DG1 at early times are not only born hot, compared to stars born later on, but are also being kinematically heated through mergers typical at early stages of galaxy formation in a Λ CDM cosmology. We therefore conclude that the thick disc in DG1 formed *in-situ* from a mixture of formation scenarios. The thick disc was born thick, i.e. “hot” kinematically speaking, from gas rich mergers as proposed by Brook et al. (2004) and was then subsequently heated via merger events, as proposed by Quinn et al. (1993).



(a) DG1



(b) DG1



(c) DG1

Figure 7.15: The age-velocity dispersion relation for *in-situ* stars in DG1 (a), the dispersion of the stars at birth at different epochs of formation (b), and their subsequent heating (c).

Kinematics Summary

Thus, the *accreted* population in DG1 and DG2 are quite different in kinematics as well as morphological properties. The *accreted* population of DG1 forms a non rotating spheroidal component, which has a slight gradient with height. The *accreted* population of DG2 shows completely different properties. In Figure 7.11 we saw that the *accreted* population lags rotationally by only $\sim 5 \text{ kms}^{-1}$, where the *in-situ* stars peak at $V_{rot} = 30 \text{ kms}^{-1}$ and the *accreted* at $V_{rot} = 25 \text{ kms}^{-1}$. The fact that the *accreted* population in DG2 is rotating enhances our conclusion of it forming a flattened rotating elliptical, rather than it forming a stellar halo like the case of the *accreted* stars in DG1.

We have determined from the kinematics that the second *in-situ* thick component in DG1 was formed from gas-rich mergers at early times that formed a thick disc, which was born kinematically hot. The stars in the thick disc were also heated due to minor and major merger events typical at early times in the formation process. The thin disc forms *in-situ* subsequently from newly in-falling gas during the remainder more quiescent period of the galaxy's evolution.

7.3.3 Chemistry

The abundances in stars provide a snapshot of the gas from which stars are born, and hence provide a window into the evolutionary history of a galaxy. Here we focus on studying the chemical properties of the *in-situ* and *accreted* stellar populations in DG1 and DG2 in order to provide greater detail on how the different evolutionary modes are imprinted in the properties of stars at redshift $z = 0$. We study the metallicity, $[\text{Fe}/\text{H}]$, for the *in-situ* and *accreted* stellar populations in DG1 and DG2 to look at metallicity gradients with height, radius and age, and make comparisons with metallicities of observed dwarf galaxies.

In Figure 7.16 we show the metallicity ($[\text{Fe}/\text{H}]$) distribution, normalised to

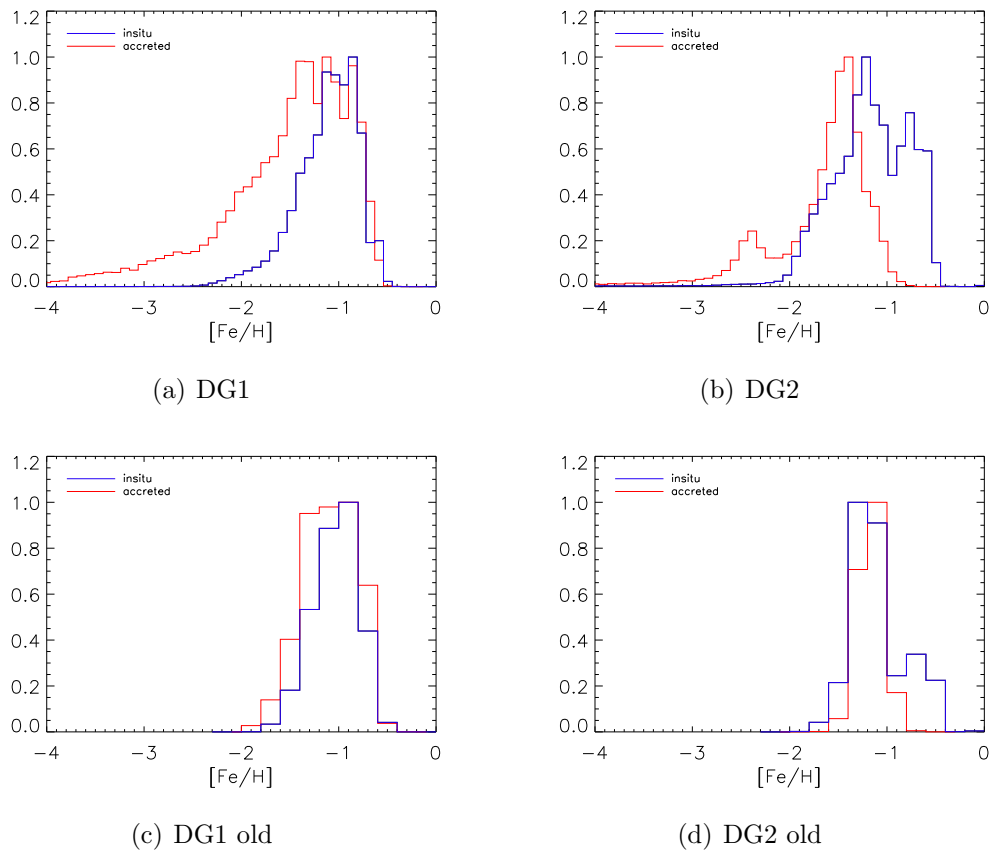


Figure 7.16: The $[\text{Fe}/\text{H}]$ distribution, normalised to unity for DG1 and DG2 to allow the shape of the distributions to be directly compared, for all stars (top panel) and for old stars (bottom panel) selected as stars with $4 < \text{age} < 10$ Gyr for *accreted* (red) and *in-situ* (blue) stars.

unity, for all *accreted* (in red) and *in-situ* (blue) stars. For DG1 the *in-situ* stars have a peak metallicity at $[\text{Fe}/\text{H}] = -0.9$ and the *accreted* stars peak at $[\text{Fe}/\text{H}] = -1.1$. In DG2 the *in-situ* stellar component peaks at $[\text{Fe}/\text{H}] = -1.2$ and the *accreted* stars peak at $[\text{Fe}/\text{H}] = -1.4$.

We plot the metallicity distribution for old stellar populations defined as having ages $4 < \text{age} < 10$ Gyr, mimicking the age selection for old RGB stars in Seth et al. (2005). We find that both the *in-situ* and *accreted* stars in both simulations have peaks around $[\text{Fe}/\text{H}] \sim -1$ agreeing well with observations of low-mass galaxies by Seth et al. (2005) (see Figure 7.16 (c) and (d)).

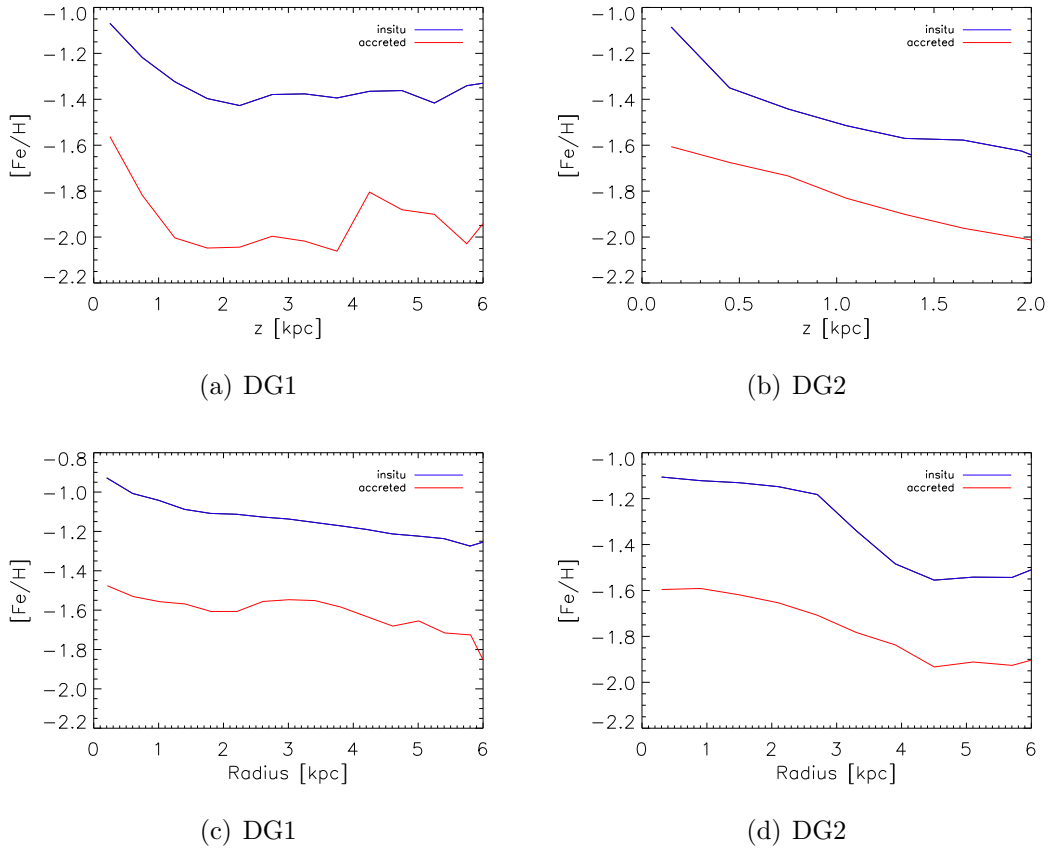


Figure 7.17: The average $[\text{Fe}/\text{H}]$ versus height (z) above the plane (top panels) and the average $[\text{Fe}/\text{H}]$ versus radius (bottom panels) stars (top panels) and disc stars (bottom panels) for the two simulated dwarf galaxies, DG1 and DG2.

In Figure 7.17 we plot the metallicity gradients in DG1 and DG2. The top panels show the average metallicity as a function of height above the plane for the region $0 < R_{xy} < 3.5$ kpc. The metallicity as a function of height for DG1, shown in the top left panel, shows gradients in the lower regions ($|z| < 2$ kpc) for both *in-situ* and *accreted* stars where the $[\text{Fe}/\text{H}]$ drops from -1.0 dex to -1.4 dex and from -1.5 dex to -2.0 dex respectively. In the higher parts of DG1 ($|z| > 2$ kpc) there are no metallicity gradients with the *in-situ* stars having an average $[\text{Fe}/\text{H}] = -1.4$ dex and the *accreted* stars having average $[\text{Fe}/\text{H}] = -2.0$ dex. DG2 also shows metallicity gradients with height. The *in-situ* population starts with a metallicity of $[\text{Fe}/\text{H}] = -1.0$ dex in the inner most regions and decreases to $[\text{Fe}/\text{H}] = -1.6$ dex at $|z| = 2$ kpc. The *accreted* stars have $[\text{Fe}/\text{H}] = -1.6$ dex in the central regions of the galaxy and drops to -2.0 dex in the outer regions.

The bottom panels of Figure 7.17 show the metallicity gradients with radius. The *in-situ* stars in DG1 have a $[\text{Fe}/\text{H}] = -0.9$ dex in the inner regions and gradually decreases to -1.25 dex in the outer most regions of the galaxy. The *accreted* stars show a similar trend where in the central parts of the galaxy they have average $[\text{Fe}/\text{H}] = -1.5$ dex and drop to -1.85 dex at larger radii. DG2 also has radial metallicity gradients for both populations, however, the gradient seems to be more pronounced in the outer regions of the galaxy, at $R_{xy} > 3$ kpc. The *in-situ* population has $[\text{Fe}/\text{H}] = -1.1$ dex in the central regions and decrease to -1.5 dex at large radii. The *accreted* stars have, at small radii, $[\text{Fe}/\text{H}] = -1.6$ dex and drop to -1.9 dex in the outskirts of the galaxy.

The lack of metallicity gradients in the *in-situ* population of DG1 reflects the fact that the thick disc was formed hot. Such a gradient would be expected if gradual heating through internal processes occurred. In Figure 7.17 (a) the gradient of $[\text{Fe}/\text{H}]$ flattens out for heights larger than $z > 2$ kpc. The gradient in $[\text{O}/\text{Fe}]$ also flattens at these distances above the mid-plane of the galaxy as we

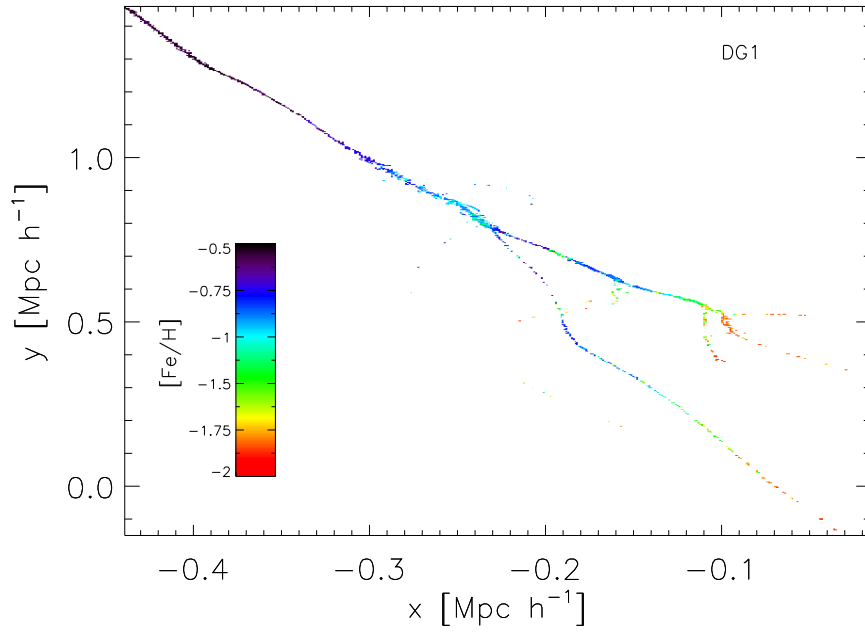
shall demonstrate below.

Age-Metallicity

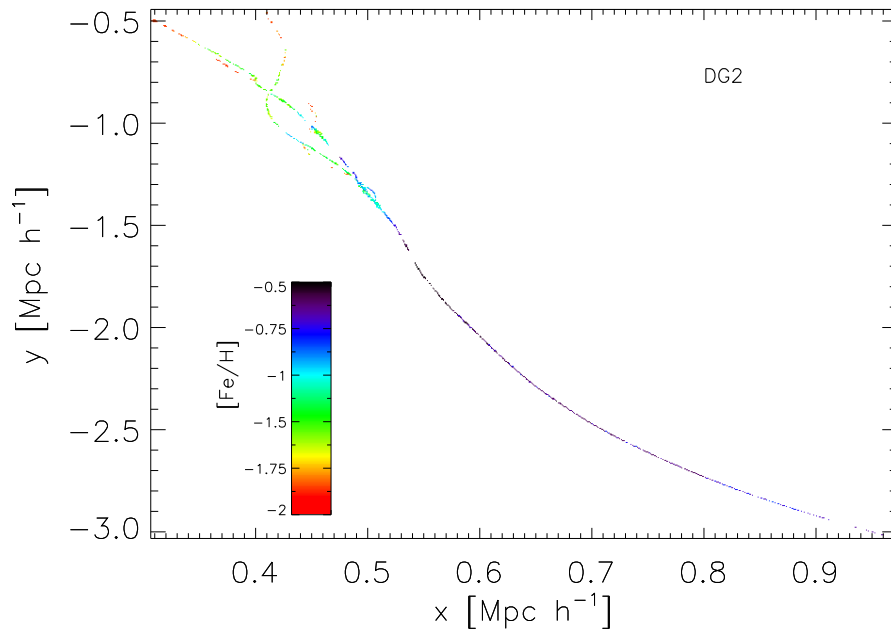
One of the consequences of chemical evolution theory is that, in the absence of inflowing primordial gas, a gradual increase in the metal content of the interstellar medium will result in the enrichment of the subsequent stellar generations formed from this gas. This would become imprinted in the age-metallicity relation, which therefore holds clues to the evolutionary history of a galaxy. The accretion of stars from lower mass systems will further complicate interpretation of this relation, as low mass galaxies have low metallicity (Tremonti et al. 2004; Lee et al. 2006; Savaglio et al. 2005; Erb et al. 2006).

In Figure 7.18 we plot the stellar merger trees, as shown previously in Figure 7.5, only we have colour coded it by $[\text{Fe}/\text{H}]$. This plot shows the evolution of the metal enrichment of stellar populations, where early stellar populations are metal poor and younger stars are metal enhanced. The more metal poor *accreted* stars can also be seen in this plot.

We plot in Figure 7.19 the age-metallicity ($[\text{Fe}/\text{H}]$ on the y-axis and time (Gyr) on x-axis) relation for each population in DG1 and DG2. The age-metallicity relation shows how metallicity increases with time, with older stars (left hand side of panels in Figure 7.19) being more metal-poor than younger stars (right hand side of panels in Figure 7.19). You can also see in this plot that the *accreted* satellite in DG2 is more metal-poor due to its earlier accretion. An interesting observation in these plots is that you can see the effect that accretion events have on the metallicity of *in-situ* stars. Regard the satellite in DG1 that is accreted at ~ 6 Gyr, and the satellite accreted at ~ 4 Gyr in DG2. These events leave a signature in the age-metallicity relation for the *in-situ* stars in both simulations at these ages. When these accretion events happen the value of $[\text{Fe}/\text{H}]$ actually



(a)



(b)

Figure 7.18: The stellar merger histories for DG1 (top panel) and DG2 (bottom panel) colour coded by metallicity $[\text{Fe}/\text{H}]$.

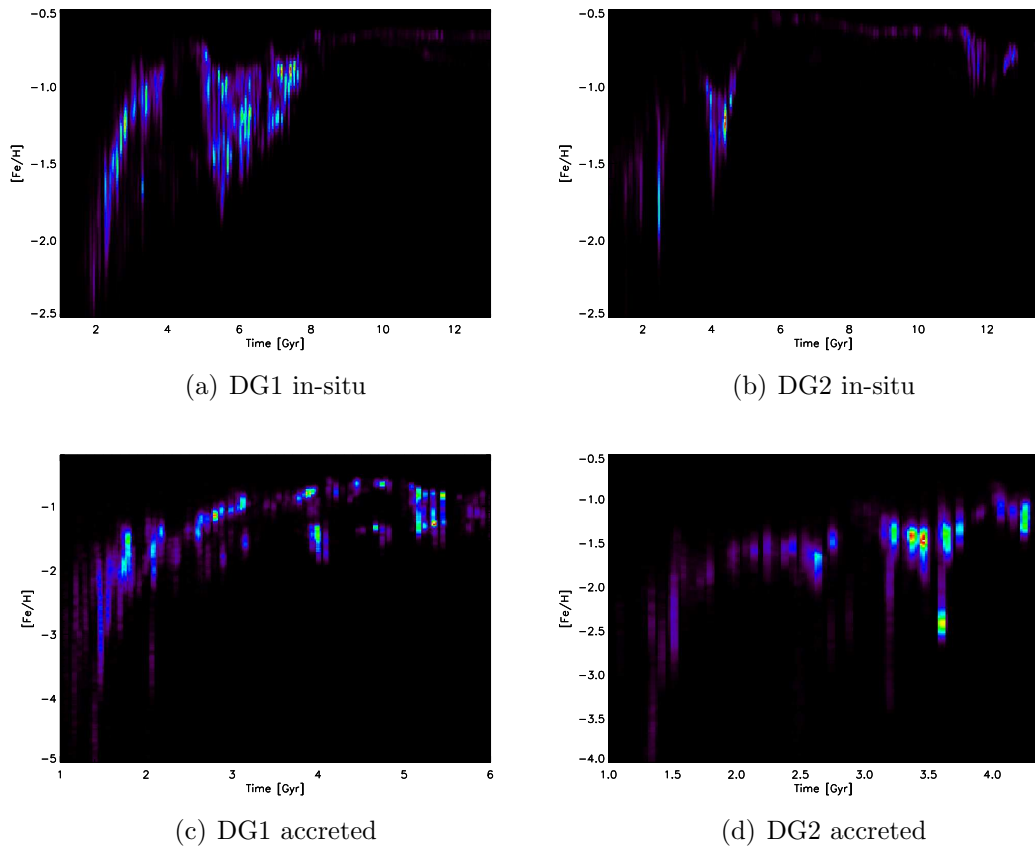


Figure 7.19: $[\text{Fe}/\text{H}]$ as a function of time (Gyr) for *in-situ* stars (top panels) and *accreted* stars (bottom panels) for the two simulated dwarf galaxies, DG1 and DG2.

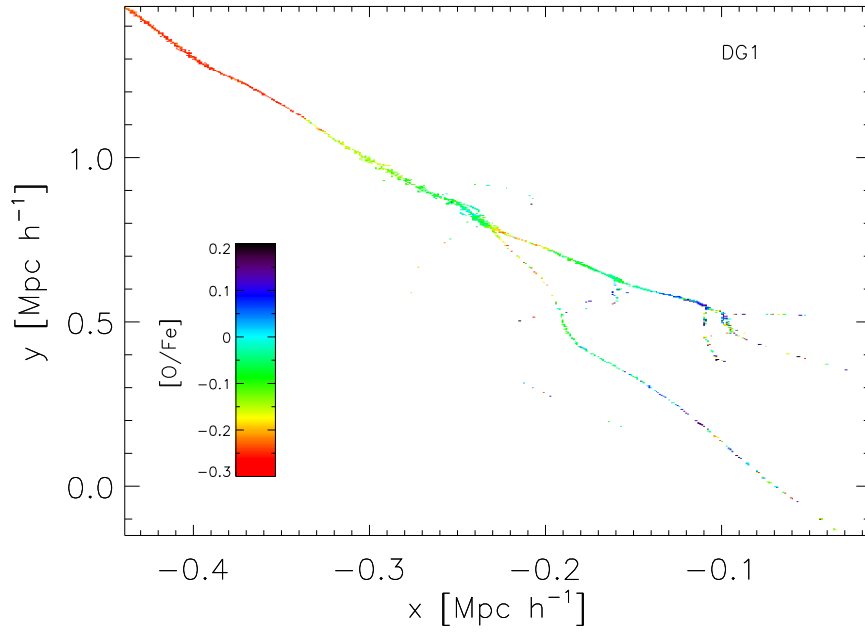
drops due to the rapid accretion of new low metallicity gas from the satellite.

Alpha-Elements

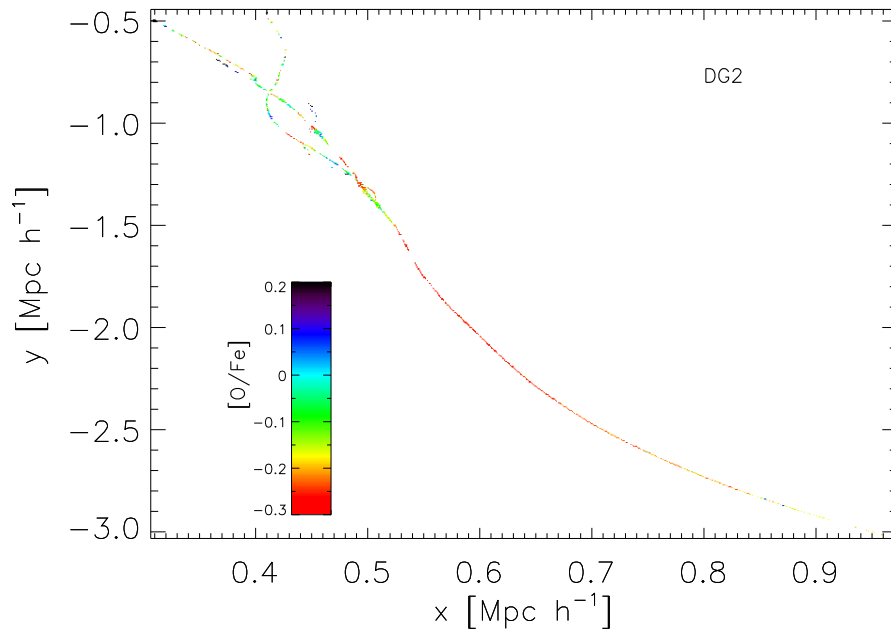
A ratio of particular interest when studying the chemical evolution of a galaxy is its $[\alpha/\text{Fe}]$ ratio. Massive stars with masses $M > 8 M_{\odot}$ explode as core-collapsed supernovae, called supernovae type II (SNeII). These types of explosions enrich the interstellar medium (ISM) with mainly α -elements, such as O, Si, Mg, Ca or Ti. They also produce but in lesser amounts Fe (Woosley & Weaver (1995)). Massive stars such as the ones that explode in SNeII are short lived and therefore enrich the ISM at the early stages of chemical evolution. Due to this they have large $[\alpha/\text{Fe}]$ ratios. On the contrary supernovae type Ia (SNeIa) introduce large amounts of Fe into the ISM and very few α -elements. They have longer lived progenitors than SNeII and therefore one sees a delay in the production of Fe compared to the α -elements. When SNeIa start to contribute to the enrichment of the ISM a decrease in the $[\alpha/\text{Fe}]$ ratios occurs. This is often referred to as the knee in the $[\alpha/\text{Fe}]$ vs $[\text{Fe}/\text{H}]$ distribution. Studying the $[\alpha/\text{Fe}]$ ratios, in our case $[\text{O}/\text{Fe}]$, tells us about the formation and timescales of the different components of galaxies. We analyse the $[\text{O}/\text{Fe}]$ abundance ratios and study their gradients in *in-situ* and *accreted* stellar populations in our simulated dwarfs.

In Figure 7.20 we plot the stellar merger histories for DG1 and DG2 colour coded by $[\text{O}/\text{Fe}]$. As the galaxy evolves the $[\text{O}/\text{Fe}]$ ratios decrease. The $[\text{O}/\text{Fe}]$ ratios do increase, however, when there is a merger, as can be seen clearly in Figure 7.20. This interesting feature is related to the merger induced star burst, which results in a generation of SN Type II, which pollute the ISM.

We plot the $[\text{O}/\text{Fe}]$ ratios as a function of time (Gyr) in Figure 7.21, where $[\text{O}/\text{Fe}]$ clearly decreases with time. Older stars (right hand side of the panels) have higher $[\text{O}/\text{Fe}]$ ratios. This means that older stars formed from gas that was



(a) DG1



(b) DG2

Figure 7.20: The stellar merger histories for DG1 (top panel) and DG2 (bottom panel) colour coded by metallicity $[\text{O}/\text{Fe}]$.

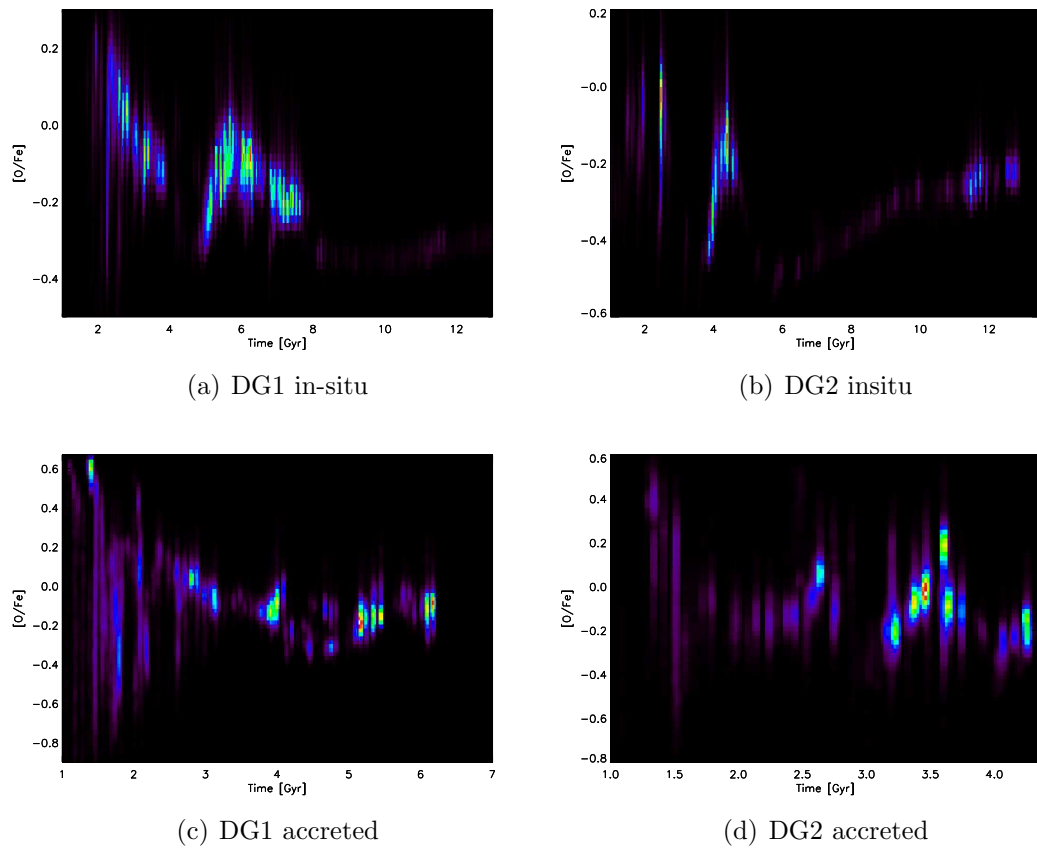


Figure 7.21: $[O/Fe]$ as a function of time (Gyr) for *in-situ* stars (top panels) and *accreted* stars (bottom panels) stars (top panels) for the two simulated dwarf galaxies, DG1 and DG2.

rich in materials synthesised in massive stars and then ejected through SNeII over short timescales. An interesting effect of the accreted satellite again arises in the *in-situ* plots (top panels of Figure 7.21). At each merger time, 6 Gyr for DG1 and 4 Gyr for DG2, the $[\text{O}/\text{Fe}]$ ratio increases for *in-situ* stars. This can be related to the starburst during this merging period which trigger short-lived SNeII explosion, enriching the galaxy alpha-elements. As we mentioned above, this effect can be seen neatly in Figure 7.20: when the merger happens there is an increase in the $[\alpha/\text{Fe}]$ ratios of the *in-situ* population.

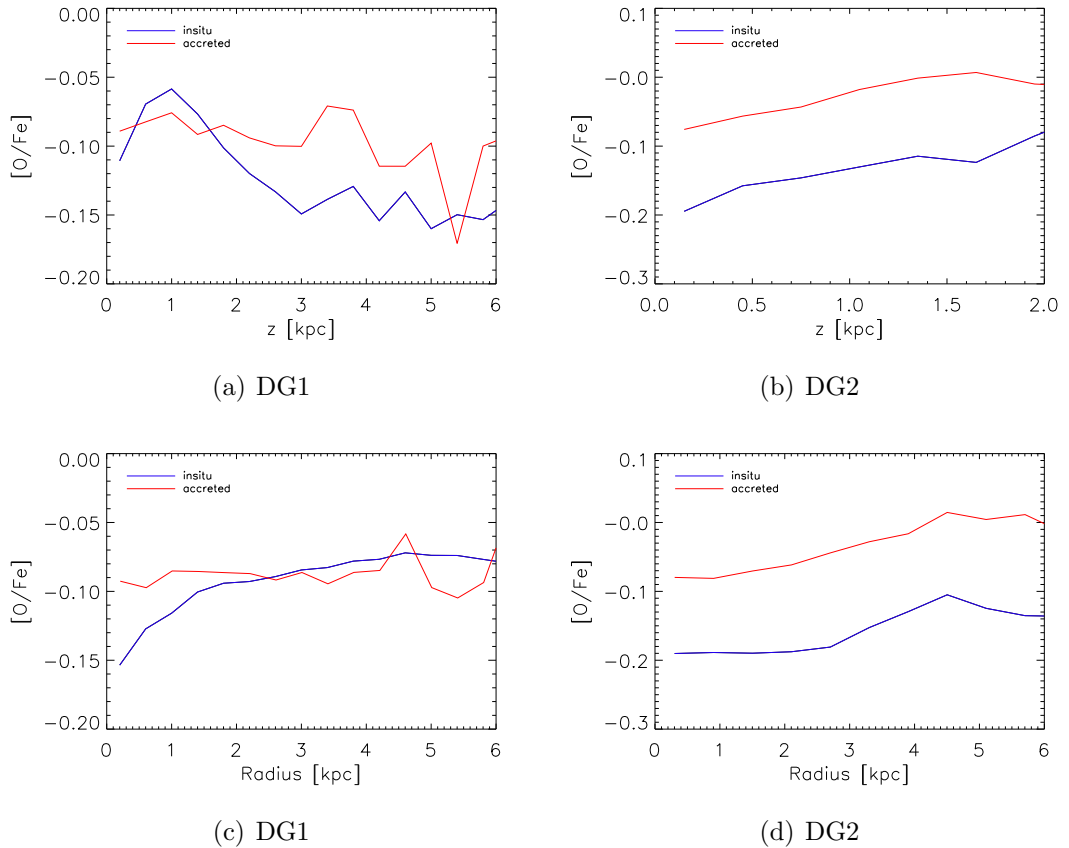


Figure 7.22: The average $[\text{O}/\text{Fe}]$ versus height (z) above the plane (top panels) and the average $[\text{O}/\text{Fe}]$ versus radius (bottom panels) stars (top panels) and disc stars (bottom panels) for the two simulated dwarf galaxies, DG1 and DG2.

We plot the gradients in $[\text{O}/\text{Fe}]$ for the *in-situ* and *accreted* stars in DG1 and

DG2 in Figure 7.22. The top panels show $[O/Fe]$ as a function of distance from the mid-plane, i.e. z (kpc), and the bottom panel shows $[O/Fe]$ as a function of radius. In DG1 the *in-situ* stars have a gradient with height above the mid-plane (top left panel of Figure 7.22), where stars close to the plane ($z < 3$ kpc) go from $[O/Fe] \sim -0.05$ in the inner most regions to -0.13 at $z = 3$ kpc. The gradient flattens out at large scaleheights, where they have an average $[O/Fe] \sim -0.15$. The *accreted* stars in DG2 show no gradient with height having, on average, $[O/Fe] \sim -0.09$. The *accreted* stars do have higher $[O/Fe]$ ratios, which is due to the fact that these stars formed earlier on prior to the enrichment of the interstellar medium (ISM) by SNeIa. The *in-situ* stars show a gradient with radius (bottom left panel of Figure 7.22) as well, only this time the $[O/Fe]$ abundances increase with stellar radii going from -0.15 in the inner regions to -0.08 at large radii ($R = 6$ kpc). The *accreted* stars once again show no radial gradient, with a more or less constant $[O/Fe] \sim -0.1$. At larger radii ($R > 2$ kpc) both *accreted* and *in-situ* stars show similar $[O/Fe]$ ratios.

DG2 has an increasing $[O/Fe]$ gradient for *in-situ* and *accreted* stars with height above the mid-plane (top right panel in Figure 7.22) and with radii (bottom right panel in Figure 7.22). The *in-situ* stars have $[O/Fe] \sim -0.2$ in the inner regions at $z = 0.2$ kpc and this ratio increases to ~ -0.1 at larger scaleheights ($z = 2$ kpc). A similar gradient applies to $[O/Fe]$ as a function of radius where the ratios go from -0.15 in the inner regions to -0.08 at $R \sim 6$ kpc. The *accreted* stars have higher $[O/Fe]$ ratios but show similar trend with height and with radius as the *in-situ* stars do, with increasing $[O/Fe]$ ratios further out in the galaxy.

In Figure 7.23 we plot the $[\alpha/Fe]$ versus $[Fe/H]$ for each population in both the simulations. For the *accreted* stars in DG1 (bottom left panel of Figure 7.23) there are clearly two separate satellites represented by the two distinct $[Fe/H]$ populations at -1.0 and -0.5 . In Figure 7.18 you can see the two different satellites

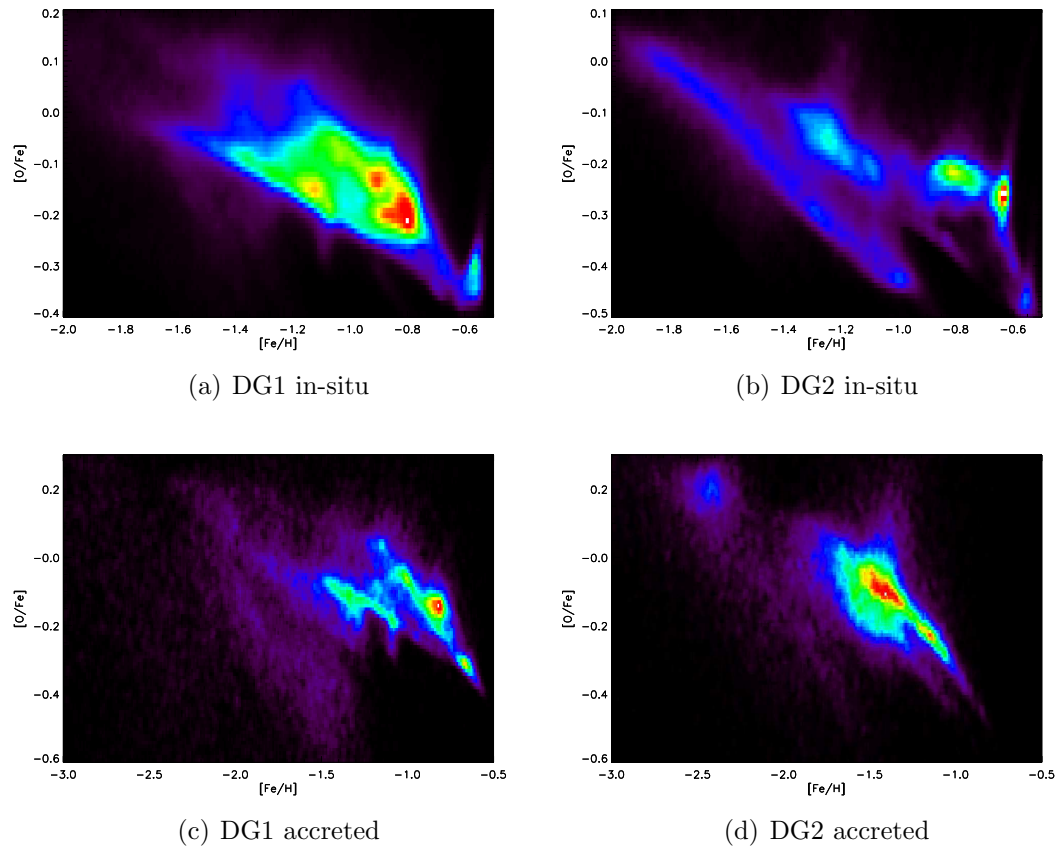


Figure 7.23: $[O/Fe]$ versus $[Fe/H]$ for *in-situ* stars (top panels) and *accreted* stars (bottom panels) stars (top panels) for the two simulated dwarf galaxies, DG1 and DG2.

accreted to the main halo. In DG2, on the other hand there is just one merger, which is reflected in the continuous $[\alpha/\text{Fe}]$ vs $[\text{Fe}/\text{H}]$ for *accreted* stars (bottom right panel of Figure 7.23), where there is no clear separation in metallicity to represent a second satellite. Again, this can be seen in Figure 7.18 where there is only one merger in DG2.

The $[\alpha/\text{Fe}]$ vs $[\text{Fe}/\text{H}]$ for *in-situ* stars in DG2 seem to show several different populations at distinct metallicities. This could be due to the bursty nature of the star formation in these simulations, and may be related to the tendency for dwarf galaxies to “breathe” (Stinson et al., 2007). In these dwarf galaxy simulations, as the gas cools and collapses into the main halo and stars start to form, the supernovae feedback is able to disrupt enough gas in these low mass galaxies to temporarily stop star formation. The gas is expelled into the hot halo where it cools, collapses and star formation occurs again. This is what (Stinson et al., 2007) describe as “breathing”. Observations of isolated dwarf galaxies have shown this episodic bursty nature in their star formation histories (Young et al., 2007).

Chemistry Summary

Overall, the *accreted* and *in-situ* stars in both the simulations show similar metallicity trends, with the *accreted* stars being more metal-poor than their *in-situ* counterparts, as one might expect from stars accreted early on in the galaxy’s evolution from lower mass progenitors. Both the populations in DG1 and DG2 show radial and vertical metallicity gradients.

We have seen that when satellites are accreted, they have an effect on the chemistry of the *in-situ* stars in galaxies. At the time of the merger, the $[\text{Fe}/\text{H}]$ of the *in-situ* stars decrease, due to the accretion of low metallicity gas, and the $[\alpha/\text{Fe}]$ ratios increase, due to the subsequent star burst triggered by the merger

event, which results in SNeII enriching the galaxy with α -elements.

7.4 Conclusions

We have analysed in this Chapter the detailed morphologies, kinematics, and chemistries of two populations in our dwarf galaxy simulations based on their origin, i.e. *accreted* or *in-situ*. We have related each population to galactic components and here we provide a summary of our results and conclusions.

We determined the *in-situ* stellar population in both DG1 and DG2 and found that in both cases they are overwhelmingly disc stars. They show a flattened spatial distribution, have small scaleheights, and are rotationally supported. The nature of the *accreted* stars, on the other hand, is quite different in the two dwarf galaxies. Nonetheless, both galaxies have separate components, which are the result of merger events, and show clear evidence of their hierarchical formation.

DG1's *in-situ* stellar population forms a thin and a thick disc component. We have determined that the thick disc in this galaxy is born hot. The merger events at early times heat the thick disc stars. Thin disc forms in the subsequent quiescent period of the galaxy's evolution.

DG1 has an *accreted* population of stars from the LMM which forms an extended spheroidal component, resembling that of a halo in nature. It has close to no net rotation and a spherical spatial distribution that extends further out than its *in-situ* disc counterpart. We found that it was not well fit by a $sech^2$ function and has an axial ratio of 0.9. Both of these findings reflect the spherical nature of this population. The *accreted* stars are more metal-poor and have higher $[\alpha/Fe]$ ratios as one would expect from stars accreted early on in the formation process.

DG2's *accreted* stellar population resembles a thick disc. It is rotating, shows a flattened distribution and is well fit by a $sech^2$ function with small measured scaleheights. However, we propose that it may be analogous to early-type, fast

rotating, flattened low-mass ellipticals. It is composed of *accreted* stars from the last major gas-rich merger at a high redshift, $z = 2$, with a mass ratio of $\sim 1:1$. The angular momentum of the accreted component today stems from this last major interaction of these two proto-galaxies of similar mass from which both the *accreted* and *in-situ* populations have adopted similar velocities, as seen in Figures 7.11, 7.12 and 7.13. An *in-situ* disc forms thereafter.

Chapter 8

Conclusions

Our understanding of galaxy formation and evolution remains far from complete. So far, we are working to a general framework in which dark energy and cold dark matter are the dominant components of the Universe. Yet if such a framework is to survive, several inconsistencies with observed properties of galaxies will need to be explained. One option is that the cold dark matter framework needs revision. The other option, the one that we pursue in this thesis, is that we require better understanding of the baryonic physics involved in gas cooling, star formation, and energy feedback from supernovae, gamma ray bursts and active galactic nuclei. These processes are highly non-linear and motivate us to attain a description of galaxy evolution by simulating it using highly intensive computational simulations. These simulations are a valuable tool to extend a bridge between reality and the incomplete information given by observations. We explore signatures in our models in the kinematics and chemistry of the stars, in particular of different components, such as the thin disc, thick disc, bulge and stellar halo as well as in different stellar populations.

All the studies in the thesis have an underlying theme, of exploring the consequences that the hierarchical formation process in Λ CDM cosmologies have on galaxy formation, and whether these signatures can explain features of observed

galaxies, and indeed whether some observed properties of galaxies are inconsistent with such a framework of galaxy formation.

In our first study we address the issue of the Milky Way’s old thin disc, as this seems at odds with the heating that one expects from the merging and accretion events within the Λ CDM formation scenario. By analysing an ensemble of disc galaxy simulations and comparing them to observations of the Galactic stellar disc, we can loosely separate our simulations into two groups, those which have interactions at low redshift after the thin disc has formed and those that show no major or minor interactions since $t = 6$ Gyr. We conclude that in order to obtain a thin disc consistent with observations of the Milky Way, the simulated galaxy must experience no interactions at late times (at least, since $t = 6$ Gyr). Yet even in our best case scenario, no simulated disc has a thin disc which is as old as the Milky Way’s thin disc. We highlight that this remains a serious and outstanding issue for the cold dark matter paradigm.

When analysing the suite of simulations, a general offset was found between the disc galaxy simulations and the Milky Way, where the simulations were all systematically hotter than the observed stellar disc. We found that, on top of the effects of mergers, a “floor” in the dispersion is related to the underlying treatment of the heating and cooling of the interstellar medium, and the low density threshold for star formation, which has been routinely implemented in Milky Way-scale galaxies. This finding has important implications for all studies of disc heating that use hydrodynamical codes.

As one of the persisting issues in disc galaxy simulations is the ability to form realistic disc, we studied the effects that feedback has on the properties of disc simulations of Milky Way mass. Increasing the stellar feedback in the cosmological simulations decreases the *accreted to in-situ* ratio due to the fact that star formation is quenched more efficiently in the low-mass building blocks.

This has a direct effect on the metallicity of the *accreted* satellites and hence on the overall metallicity of the galaxy.

Mass assembly within the context of hierarchical formation is essentially scale free. Keeping within the same theme of hierarchical clustering, we resize cosmological simulations to three different mass scales, allowing us to isolate the effects of baryonic physics in shaping the properties of the final galaxies. The overall properties were found to be very different in the different mass galaxies, which is consistent with galactic properties depending strongly on mass. However, vertical metallicity gradients of *in-situ* and *accreted* stars follow the same trends at all mass scales, whereby *in-situ* have strong vertical gradients whilst *accreted* stars have no vertical metallicity gradients. We also show that the *accreted* stars in the more massive galaxies have different chemistry than the stars found in the less massive galaxies. This highlights that the building blocks in the hierarchical formation of massive galaxies are not analogues of low mass galaxies at $z = 0$.

In our final study, we find that multiple components in dwarf galaxies may indeed be related to their hierarchical formation. Yet we also highlight that dis-entangling the processes of gas accretion, merging and star formation and interpreting observation is far from simple. The two analysed dwarf simulations both show signatures of having two disc components, a thick and thin disc, yet the thick discs seem to form in two different ways. One gains angular momentum from the last major merger, creating an analogue of fast rotating elliptical galaxies, with a thin disc subsequently growing from newly accreted gas. The other forms a thick disc *in-situ* from gas that is settling during a period of gas rich mergers.

The field of galaxy formation and evolution will remain an exciting field for theorist and observers over the next decade. New surveys will provide an abundance of data and information on the Milky Way and external galaxies. Surveys such as RAVE, GAIA and HERMES are fundamental to ascertain parameters

such as ages, abundances, velocities and distances for stars in the Milky Way. Coupled with improved simulations, this will help us gain a better and more enriched understanding of how galaxies such as our own Milky Way form, and provide further constraints on our cosmological paradigm.

Bibliography

- Abadi M. G., Navarro J. F., Steinmetz M., Eke V. R., 2003a, *ApJ*, 591, 499
- Abadi M. G., Navarro J. F., Steinmetz M., Eke V. R., 2003b, *ApJ*, 597, 21
- Agertz O., Teyssier R., Moore B., 2010, *ArXiv e-prints*
- Allen P. D., Driver S. P., Graham A. W., Cameron E., Liske J., de Propris R., 2006, *MNRAS*, 371, 2
- Anguiano B., Freeman K., Steinmetz M., Wylle de Boer E., Siebert A., The Rave Collaboration 2009, in J. Andersen, J. Bland-Hawthorn, & B. Nordström ed., *IAU Symposium Vol. 254 of IAU Symposium, RAVE: The Age-Metallicity-Velocity relation in the nearby disk*. pp 3P–+
- Aumer M., Binney J. J., 2009, *MNRAS*, 397, 1286
- Bailin J., Kawata D., Gibson B. K., Steinmetz M., Navarro J. F., Brook C. B., Gill S. P. D., Ibata R. A., Knebe A., Lewis G. F., Okamoto T., 2005, *ApJL*, 627, L17
- Barnes J. E., Hernquist L., 1996, *ApJ*, 471, 115
- Barnes J. E., Hernquist L., 1998, *ApJ*, 495, 187
- Battaglia G., Helmi A., Morrison H., Harding P., Olszewski E. W., Mateo M., Freeman K. C., Norris J., Shectman S. A., 2005, *MNRAS*, 364, 433

-
- Bekki K., Chiba M., 2005, MNRAS, 356, 680
- Bell E. F., Zucker D. B., Belokurov V., Sharma S., Johnston K. V., Bullock J. S., Hogg D. W., Jahnke K., de Jong J. T. A., Beers T. C., Evans N. W., Grebel E. K., Ivezić Ž., Koposov S. E., Rix H.-W., Schneider D. P., Steinmetz M., Zolotov A., 2008, ApJ, 680, 295
- Bensby T., Alves-Brito A., Oey M. S., Yong D., Meléndez J., 2011, ArXiv e-prints
- Bensby T., Feltzing S., 2010, in K. Cunha, M. Spite, & B. Barbuy ed., IAU Symposium Vol. 265 of IAU Symposium, The Galactic thin and thick disks in the context of galaxy formation. pp 300–303
- Bensby T., Feltzing S., Lundström I., 2003, A&A, 410, 527
- Bensby T., Feltzing S., Lundström I., 2004, A&A, 415, 155
- Bensby T., Feltzing S., Lundström I., Ilyin I., 2005, A&A, 433, 185
- Bensby T., Zenn A. R., Oey M. S., Feltzing S., 2007, ApJL, 663, L13
- Benson A. J., Frenk C. S., Lacey C. G., Baugh C. M., Cole S., 2002, MNRAS, 333, 177
- Blumenthal G. R., Faber S. M., Primack J. R., Rees M. J., 1984, Nature, 311, 517
- Bournaud F., Elmegreen B. G., Martig M., 2009, ApJL, 707, L1
- Bournaud F., Jog C. J., Combes F., 2005, A&A, 437, 69
- Brook C. B., Gibson B. K., Martel H., Kawata D., 2005, ApJ, 630, 298
- Brook C. B., Governato F., Roškar R., Stinson G., Brooks A. M., Wadsley J., Quinn T., Gibson B. K., Snaith O., Pilkington K., House E., Pontzen A., 2011, MNRAS, pp 595–+

-
- Brook C. B., Kawata D., Gibson B. K., Flynn C., 2004, MNRAS, 349, 52
- Brook C. B., Kawata D., Gibson B. K., Freeman K. C., 2004, ApJ, 612, 894
- Brooks A. M., Governato F., Quinn T., Brook C. B., Wadsley J., 2009, ApJ, 694, 396
- Bullock J. S., Kravtsov A. V., Weinberg D. H., 2001, ApJ, 548, 33
- Burkert A., Genzel R., Bouché N., Cresci G., Khochfar S., Sommer-Larsen J., Sternberg A., Naab T., Förster Schreiber N., Tacconi L., Shapiro K., Hicks E., Lutz D., Davies R., Buschkamp P., Genel S., 2010, ApJ, 725, 2324
- Burkert A., Naab T., 2003, in G. Contopoulos & N. Voglis ed., *Galaxies and Chaos* Vol. 626 of *Lecture Notes in Physics*, Berlin Springer Verlag, Major Mergers and the Origin of Elliptical Galaxies. pp 327–339
- Burkert A., Naab T., Johansson P. H., Jesseit R., 2008, ApJ, 685, 897
- Burstein D., 1979, ApJ, 234, 829
- Cameron E., Driver S. P., Graham A. W., Liske J., 2009, ApJ, 699, 105
- Cappellari M., Emsellem E., Bacon R., Bureau M., Davies R. L., de Zeeuw P. T., Falcón-Barroso J., Krajnović D., Kuntschner H., McDermid R. M., Peletier R. F., Sarzi M., van den Bosch R. C. E., van de Ven G., 2007, MNRAS, 379, 418
- Carney B. W., Latham D. W., Laird J. B., Aguilar L. A., 1994, AJ, 107, 2240
- Carollo D., Beers T. C., Chiba M., Norris J. E., Freeman K. C., Lee Y. S., Ivezić Ž., Rockosi C. M., Yanny B., 2010, ApJ, 712, 692
- Carollo D., Beers T. C., Lee Y. S., Chiba M., Norris J. E., Wilhelm R. e. a., 2007, nat, 450, 1020

-
- Ceverino D., Dekel A., Bournaud F., 2010, MNRAS, 404, 2151
- Chapman S. C., Ibata R., Lewis G. F., Ferguson A. M. N., Irwin M., McConnachie A., Tanvir N., 2006, ApJ, 653, 255
- Chen B., Stoughton C., Smith J. A., Uomoto A., Pier J. R., Yanny B., Ivezić Ž., York D. G., Anderson J. E., Annis J., Brinkmann J., Csabai I., Fukugita M., Hindsley R., Lupton R., Munn J. A., the SDSS Collaboration 2001, ApJ, 553, 184
- Cheng J. Y., Faber S. M., Simard L., Graves G. J., Lopez E. D., Yan R., Cooper M. C., 2011, MNRAS, 412, 727
- Chiba M., Beers T. C., 2000, AJ, 119, 2843
- Cowie L. L., Songaila A., Hu E. M., Cohen J. G., 1996, AJ, 112, 839
- Dalcanton J. J., Bernstein R. A., 2002, AJ, 124, 1328
- Dalcanton J. J., Yoachim P., Bernstein R. A., 2004, ApJ, 608, 189
- Dehnen W., Binney J. J., 1998, MNRAS, 298, 387
- Edvardsson B., Andersen J., Gustafsson B., Lambert D. L., Nissen P. E., Tomkin J., 1993, aaps, 102, 603
- Eisenhauer F., Schödel R., Genzel R., Ott T., Tecza M., Abuter R., Eckart A., Alexander T., 2003, ApJL, 597, L121
- Emsellem E., Cappellari M., Krajnović D., Alatalo K., Blitz L., Bois M., Bournaud F., et al. 2011, ArXiv e-prints
- Erb D. K., Shapley A. E., Pettini M., Steidel C. C., Reddy N. A., Adelberger K. L., 2006, ApJ, 644, 813

-
- Faber S. M., Tremaine S., Ajhar E. A., Byun Y.-I., Dressler A., Gebhardt K., Grillmair C., Kormendy J., Lauer T. R., Richstone D., 1997, *AJ*, 114, 1771
- Fall S. M., Efstathiou G., 1980, *MNRAS*, 193, 189
- Feltzing S., Bensby T., Lundström I., 2003, *A&A*, 397, L1
- Förster Schreiber N. M., Shapley A. E., Erb D. K., Genzel R., Steidel C. C., Bouché N., Cresci G., Davies R., 2010, *ArXiv e-prints*
- Gebhardt K., Richstone D., Ajhar E. A., Lauer T. R., Byun Y.-I., Kormendy J., Dressler A., Faber S. M., Grillmair C., Tremaine S., 1996, *AJ*, 112, 105
- Geha M., Blanton M. R., Masjedi M., West A. A., 2006, *ApJ*, 653, 240
- Geisler D., Smith V. V., Wallerstein G., Gonzalez G., Charbonnel C., 2005, *AJ*, 129, 1428
- Genzel R., Burkert A., Bouché N., Cresci G., Förster Schreiber N. M., Shapley A., et al. 2008, *ApJ*, 687, 59
- Gibson B. K., Courty S., Sánchez-Blázquez P., Teyssier R., House E. L., Brook C. B., Kawata D., 2009, in J. Andersen, J. Bland-Hawthorn, & B. Nordström ed., *IAU Symposium Vol. 254 of IAU Symposium, Hydrodynamical Adaptive Mesh Refinement Simulations of Disk Galaxies*. pp 445–452
- Gilmore G., Reid N., 1983, *MNRAS*, 202, 1025
- Governato F., Brook C., 2009, *ArXiv e-prints*, 801
- Governato F., Brook C., Mayer L., Brooks A., Rhee G., Wadsley J., Jonsson P., Willman B., Stinson G., Quinn T., Madau P., 2010, *Nature*, 463, 203
- Governato F., Willman B., Mayer L., Brooks A., Stinson G., Valenzuela O., Wadsley J., Quinn T., 2007, *MNRAS*, 374, 1479

-
- Haywood M., 2008, MNRAS, 388, 1175
- Hernquist L., 1990, ApJ, 356, 359
- Hernquist L., 1993, apjs, 86, 389
- Holmberg J., Nordstroem B., Andersen J., 2008, VizieR Online Data Catalog, 5128, 0
- Holmberg J., Nordström B., Andersen J., 2007, A&A, 475, 519
- Ibata R. A., Gilmore G. F., 1995, MNRAS, 275, 591
- Ivezić Ž., Sesar B., Jurić M., Bond N., Dalcanton J., Rockosi C. M., Yanny B., Newberg H. J., et al. 2008, ApJ, 684, 287
- Jonsson P., 2006, MNRAS, 372, 2
- Jurić M., Ivezić Ž., Brooks A., Lupton R. H., Schlegel D., Finkbeiner D., Padmanabhan N., et al. 2008, ApJ, 673, 864
- Kalirai J. S., Gilbert K. M., Guhathakurta P., Majewski S. R., Ostheimer J. C., Rich R. M., Cooper M. C., Reitzel D. B., Patterson R. J., 2006, ApJ, 648, 389
- Katz N., Hernquist L., Weinberg D. H., 1992, ApJL, 399, L109
- Katz N., White S. D. M., 1993, ApJ, 412, 455
- Kawata D., Gibson B. K., 2003, MNRAS, 340, 908
- Kazantzidis S., Bullock J. S., Zentner A. R., Kravtsov A. V., Moustakas L. A., 2008, ApJ, 688, 254
- Kazantzidis S., Zentner A. R., Kravtsov A. V., Bullock J. S., Debattista V. P., 2009, ApJ, 700, 1896

-
- Kennicutt R. C., 1998, *ApJ*, 498, 541
- Kereš D., Katz N., Weinberg D. H., Davé R., 2005, *MNRAS*, 363, 2
- Khochfar S., Burkert A., 2003, *ApJL*, 597, L117
- Khochfar S., Burkert A., 2005, *MNRAS*, 359, 1379
- Kobayashi C., Umeda H., Nomoto K., Tominaga N., Ohkubo T., 2006, *ApJ*, 653, 1145
- Lauer T. R., Ajhar E. A., Byun Y.-I., Dressler A., Faber S. M., Grillmair C., Kormendy J., Richstone D., Tremaine S., 1995, *AJ*, 110, 2622
- Leaman R., Cole A., Venn K., Tolstoy E., Irwin M., Szeifert T., 2007, in American Astronomical Society Meeting Abstracts #210 Vol. 38 of Bulletin of the American Astronomical Society, First Metallicity Distribution From CaT Spectroscopy of RGB Stars in the Dwarf Irregular Galaxy WLM. pp 121.10–+
- Lee H., Skillman E. D., Cannon J. M., Jackson D. C., Gehrz R. D., Polomski E. F., Woodward C. E., 2006, *ApJ*, 647, 970
- Lee Y. S., Beers T. C., An D., Ivezić Z., Just A., Rockosi C. M., Morrison H. L., Johnson J. A., Schonrich R., Bird J., Yanny B., Harding P., Rocha-Pinto H. J., 2011, *ArXiv e-prints*
- Lemoine-Busserolle M., Lamareille F., 2010, *MNRAS*, 402, 2291
- Loebman S. R., Roskar R., Debattista V. P., Ivezić Z., Quinn T. R., Wadsley J., 2010, *ArXiv e-prints*
- Magorrian J., Tremaine S., Richstone D., Bender R., Bower G., Dressler A., Faber S. M., Gebhardt K., Green R., Grillmair C., Kormendy J., Lauer T., 1998, *AJ*, 115, 2285

-
- Mashchenko S., Wadsley J., Couchman H. M. P., 2008, *Science*, 319, 174
- Matteucci F., 2007, ArXiv e-prints
- Mayer L., 2004, ArXiv Astrophysics e-prints
- Mayer L., Governato F., Kaufmann T., 2008, ArXiv e-prints, 801
- Minniti D., Borissova J., Rejkuba M., Alves D. R., Cook K. H., Freeman K. C., 2003, *Science*, 301, 1508
- Minniti D., Zoccali M., 2008, in M. Bureau, E. Athanassoula, & B. Barbuy ed., *IAU Symposium Vol. 245 of IAU Symposium, The Galactic bulge: a review.* pp 323–332
- Mishenina T. V., Soubiran C., Kovtyukh V. V., Korotin S. A., 2004, *A&A*, 418, 551
- Mo H., van den Bosch F. C., White S., 2010, *Galaxy Formation and Evolution*
- Moore B., Katz N., Lake G., 1996, *ApJ*, 457, 455
- Morrison H. L., 1993, *AJ*, 106, 578
- Moster B. P., Macciò A. V., Somerville R. S., Johansson P. H., Naab T., 2010, *MNRAS*, 403, 1009
- Mould J., Kristian J., 1986, *ApJ*, 305, 591
- Naab T., Burkert A., Hernquist L., 1999, *ApJL*, 523, L133
- Navarro J. F., Abadi M. G., Venn K. A., Freeman K. C., Anguiano B., 2010, ArXiv e-prints
- Navarro J. F., Benz W., 1991, *ApJ*, 380, 320

-
- Navarro J. F., Frenk C. S., White S. D. M., 1996, *ApJ*, 462, 563
- Navarro J. F., Frenk C. S., White S. D. M., 1997, *ApJ*, 490, 493
- Navarro J. F., Steinmetz M., 1997, *ApJ*, 478, 13
- Navarro J. F., White S. D. M., 1994, *MNRAS*, 267, 401
- Nissen P. E., 1995, in P. C. van der Kruit & G. Gilmore ed., *Stellar Populations*
Vol. 164 of IAU Symposium, Age and Metallicity Distributions among Galactic
Disk Stars. pp 109–+
- Nomoto K., Kobayashi C., Umeda H., 2002, in K. Nomoto & J. W. Truran ed.,
Cosmic Chemical Evolution Vol. 187 of IAU Symposium, Type Ia supernovae
and chemical evolution of galaxies. pp 33–46
- Nomoto K., Tominaga N., Umeda H., Kobayashi C., Maeda K., 2006, *Nuclear
Physics A*, 777, 424
- Nomoto K., Umeda H., 2002, in R. Fusco-Femiano & F. Matteucci ed., *Chemical
Enrichment of Intracluster and Intergalactic Medium* Vol. 253 of *Astronomical
Society of the Pacific Conference Series*, Hypernova Nucleosynthesis and Early
Chemical Evolution. (I). pp 221–+
- Nordström B., Mayor M., Andersen J., Holmberg J., Pont F., Jørgensen B. R.,
Olsen E. H., Udry S., Mowlavi N., 2004, *AAP*, 418, 989
- Oh S.-H., Brook C., Governato F., Brinks E., Mayer L., de Blok W. J. G., Brooks
A., Walter F., 2010, *ArXiv e-prints*
- Okamoto T., Eke V. R., Frenk C. S., Jenkins A., 2005, *MNRAS*, 363, 1299
- Paczynski B., 1998, *ApJL*, 494, L45+
- Penzias A. A., Schraml J., Wilson R. W., 1969, *ApJL*, 157, L49+

-
- Podsiadlowski P., Mazzali P. A., Nomoto K., Lazzati D., Cappellaro E., 2004, *ApJL*, 607, L17
- Pohlen M., Balcells M., Lütticke R., Dettmar R.-J., 2004, *AAP*, 422, 465
- Pompéia L., Hill V., Spite M., Cole A., Primas F., Romaniello M., Pasquini L., Cioni M.-R., Smecker Hane T., 2008, *A&A*, 480, 379
- Purcell C. W., Bullock J. S., Kazantzidis S., 2010, *MNRAS*, 404, 1711
- Quillen A. C., Garnett D. R., 2001, in J. G. Funes & E. M. Corsini ed., *Galaxy Disks and Disk Galaxies Vol. 230 of Astronomical Society of the Pacific Conference Series, The Saturation of Disk Heating in the Solar Neighborhood and Evidence for a Merger 9 Gyr Ago.* pp 87–88
- Quinn P. J., Hernquist L., Fullagar D. P., 1993, *ApJ*, 403, 74
- Ramírez I., Allende Prieto C., Lambert D. L., 2007, *A&A*, 465, 271
- Read J. I., Lake G., Agertz O., Debattista V. P., 2008, *MNRAS*, 389, 1041
- Reddy B. E., Tomkin J., Lambert D. L., Allende Prieto C., 2003, *MNRAS*, 340, 304
- Reid N., Majewski S. R., 1993, *ApJ*, 409, 635
- Rest A., van den Bosch F. C., Jaffe W., Tran H., Tsvetanov Z., Ford H. C., Davies J., Schafer J., 2001, *AJ*, 121, 2431
- Robertson B., Bullock J. S., Font A. S., Johnston K. V., Hernquist L., 2005, *ApJ*, 632, 872
- Robertson B., Yoshida N., Springel V., Hernquist L., 2004, *ApJ*, 606, 32
- Robertson B. E., Kravtsov A. V., 2008, *ApJ*, 680, 1083

-
- Roškar R., Debattista V. P., Brooks A. M., Quinn T. R., Brook C. B., Governato F., Dalcanton J. J., Wadsley J., 2010, ArXiv e-prints
- Roškar R., Debattista V. P., Quinn T. R., Stinson G. S., Wadsley J., Kaufmann T., 2009, in J. Andersen, J. Bland-Hawthorn, & B. Nordström ed., IAU Symposium Vol. 254 of IAU Symposium, Clues to radial migration from the properties of outer disks. pp 64P–+
- Roškar R., Debattista V. P., Stinson G. S., Quinn T. R., Kaufmann T., Wadsley J., 2008, ApJL, 675, L65
- Rubin V. C., Ford Jr. W. K., 1970, ApJ, 159, 379
- Sánchez-Blázquez P., Courty S., Gibson B. K., Brook C. B., 2009, MNRAS, 398, 591
- Savaglio S., Glazebrook K., Le Borgne D., Juneau S., Abraham R. G., Chen H.-W., Crampton D., McCarthy P. J., Carlberg R. G., Marzke R. O., Roth K., Jørgensen I., Murowinski R., 2005, ApJ, 635, 260
- Scannapieco C., Tissera P. B., White S. D. M., Springel V., 2009, in J. Andersen, J. Bland-Hawthorn, & B. Nordström ed., IAU Symposium Vol. 254 of IAU Symposium, Effects of Supernova Feedback on the Formation of Galaxies. pp 369–374
- Schönrich R., Binney J., 2009, MNRAS, 396, 203
- Seabroke G. M., Gilmore G., 2007, MNRAS, 380, 1348
- Searle L., Zinn R., 1978, ApJ, 225, 357
- Seth A. C., Dalcanton J. J., de Jong R. S., 2005, AJ, 129, 1331
- Shetrone M. D., Côté P., Sargent W. L. W., 2001, ApJ, 548, 592

-
- Silk J., 2011, ArXiv e-prints
- Smecker-Hane T. A., Cole A. A., Gallagher III J. S., Stetson P. B., 2002, ApJ, 566, 239
- Sommer-Larsen J., Götz M., Portinari L., 2003, ApJ, 596, 47
- Soubiran C., Bienaymé O., Mishenina T. V., Kovtyukh V. V., 2008, A&A, 480, 91
- Soubiran C., Girard P., 2005, A&A, 438, 139
- Spergel D. N., Verde L., Peiris H. V., Komatsu E., Nolta M. R., Bennett C. L., Halpern M., Hinshaw G., Jarosik N., Kogut A., Limon M., Meyer S. S., Page L., Tucker G. S., Weiland J. L., Wollack E., Wright E. L., 2003, ApJs, 148, 175
- Springel V., Di Matteo T., Hernquist L., 2005, MNRAS, 361, 776
- Springel V., Hernquist L., 2005, ApJl, 622, L9
- Steinmetz M., 1996, MNRAS, 278, 1005
- Steinmetz M., Mueller E., 1994, A&A, 281, L97
- Steinmetz M., Navarro J. F., 2002, New Astronomy, 7, 155
- Steinmetz M., White S. D. M., 1997, MNRAS, 288, 545
- Stewart K. R., Bullock J. S., Wechsler R. H., Maller A. H., 2009, ApJ, 702, 307
- Stinson G., Seth A., Katz N., Wadsley J., Governato F., Quinn T., 2006, MNRAS, 373, 1074
- Stinson G. S., Bailin J., Couchman H., Wadsley J., Shen S., Nickerson S., Brook C., Quinn T., 2010, MNRAS, 408, 812

-
- Stinson G. S., Dalcanton J. J., Quinn T., Kaufmann T., Wadsley J., 2007, *ApJ*, 667, 170
- Summers F. J., Evrard A. E., Davis M., 1993, in J. M. Shull & H. A. Thronson ed., *Evolution of Galaxies and their Environment Galaxy tracers in N-body simulations*. pp 56–57
- Teyssier R., 2002, *A&A*, 385, 337
- Thacker R. J., Couchman H. M. P., 2000, *ApJ*, 545, 728
- Tolstoy E., Venn K. A., Shetrone M., Primas F., Hill V., Kaufer A., Szeifert T., 2003, *AJ*, 125, 707
- Toomre A., 1977, in B. M. Tinsley & R. B. Larson ed., *Evolution of Galaxies and Stellar Populations Mergers and Some Consequences*. pp 401–+
- Tremonti C. A., Heckman T. M., Kauffmann G., Brinchmann J., Charlot S., White S. D. M., Seibert M., Peng E. W., Schlegel D. J., Uomoto A., Fukugita M., Brinkmann J., 2004, *ApJ*, 613, 898
- Tsikoudi V., 1979, *ApJ*, 234, 842
- van den Bosch F. C., Burkert A., Swaters R. A., 2001, *MNRAS*, 326, 1205
- van Starckenburg L., van der Werf P. P., Franx M., Labbé I., Rudnick G., Wuyts S., 2008, *A&A*, 488, 99
- Veilleux S., Cecil G., Bland-Hawthorn J., 2005, *ARAA*, 43, 769
- Velazquez H., White S. D. M., 1999, *MNRAS*, 304, 254
- Venn K. A., Irwin M., Shetrone M. D., Tout C. A., Hill V., Tolstoy E., 2004, *AJ*, 128, 1177

-
- Verde L., Oh S. P., Jimenez R., 2002, MNRAS, 336, 541
- Villalobos Á., Helmi A., 2008, MNRAS, 391, 1806
- Wadsley J. W., Stadel J., Quinn T., 2004, New Astronomy, 9, 137
- West A. A., Garcia-Appadoo D. A., Dalcanton J. J., Disney M. J., 2005, in
AIP Conf. Proc. 761: The Spectral Energy Distributions of Gas-Rich Galaxies:
Confronting Models with Data HI Selected Galaxies in the SDSS. pp 409–+
- White S. D. M., Frenk C. S., 1991, ApJ, 379, 52
- White S. D. M., Rees M. J., 1978, MNRAS, 183, 341
- Widrow L. M., Dubinski J., 2005, ApJ, 631, 838
- Wilkinson M. I., Evans N. W., 1999, MNRAS, 310, 645
- Williams M. J., Zamojski M. A., Bureau M., Kuntschner H., Merrifield M. R.,
de Zeeuw P. T., Kuijken K., 2011, MNRAS, 414, 2163
- Woosley S. E., Weaver T. A., 1995, apjs, 101, 181
- Wyse R. F. G., 1999, Baltic Astronomy, 8, 593
- Yoachim P., Dalcanton J., 2002, in American Astronomical Society Meeting Ab-
stracts Vol. 34 of Bulletin of the American Astronomical Society, Thick and
thin disk structural parameters in edge-on spiral galaxies. pp 1117–+
- Yoachim P., Dalcanton J. J., 2005, ApJ, 624, 701
- Yoachim P., Dalcanton J. J., 2006, AJ, 131, 226
- Yoachim P., Dalcanton J. J., 2008, ApJ, 682, 1004
- Young L. M., Skillman E. D., Weisz D. R., Dolphin A. E., 2007, ApJ, 659, 331

Zaritsky D., Olszewski E. W., Schommer R. A., Peterson R. C., Aaronson M.,
1989, ApJ, 345, 759

Zibetti S., White S. D. M., Brinkmann J., 2004, MNRAS, 347, 556

Zoccali M., Hill V., Lecureur A., Barbuy B., Renzini A., Minniti D., Gómez A.,
Ortolani S., 2008, A&A, 486, 177

Zolotov A., Friends S. D. M., 2009, MNRAS, 347, 556

Zolotov A., Willman B., Brooks A. M., Governato F., Hogg D. W., Shen S.,
Wadsley J., 2010, ApJ, 721, 738